Dynamical effects in fluid complex plasmas

Mierk Schwabe

München 2009

Dynamical effects in fluid complex plasmas

Mierk Schwabe

Dissertation
an der Fakultät für Physik
der Ludwig–Maximilians–Universität
München

vorgelegt von
Mierk Schwabe
aus Preetz

München, den 28. 08. 2009

Erstgutachter: Prof. G. E. Morfill
Zweitgutachter: Prof. D. Habs
Tag der mündlichen Prüfung: 24. 11. 2009

Contents

Zusammenfassung

Komplexe Plasmen bestehen aus Neutralteilchen, Ionen, Elektronen und zusätzlichen Mikroteilchen. Flüsse der Plasmateilchen auf die Mikroteilchen laden sie auf, und die Teilchen wechselwirken miteinander. Wird das System z.B. mit einem Laser beleuchtet, ermöglichen Aufnahmen des gestreuten Lichts vollständig aufgelöste kinetische Untersuchungen auf allen relevanten Frequenzen, z.B. der Einstein-, Debye- und Plasmafrequenz.

In dieser Arbeit werden dynamische Effekte in fluiden komplexen Plasmen im PK-3 Plus Aufbau, der aus einer Radiofrequenz-Plasmakammer besteht, auf der Internationalen Raumstation (ISS), während eines Parabelflugs und auf dem Boden untersucht. Ziel ist die Erforschung von dynamischen Phänomenen auf dem Partikelniveau, z.B. um zu eruieren, ab wann "korpuskulare" Effekte wichtig werden und wann die klassische Fluiddynamik eine adäquate Beschreibung liefert. Dazu werden "Periodgramme" verwendet, die eine Untersuchung der globalen dynamischen Struktur ermöglichen. Geschwindigkeiten und Kräfte auf einzelne Teilchen werden durch Analyse der Teilchenbewegung studiert.

Hochaufgelöste selbstangeregte Wellen wurden mit Experimenten im Labor auf dem Boden analysiert, in denen die Stärke der Kraft, die die Teilchen in die Randschichtbereiche der Kammer drückt, durch Thermophorese kontrolliert wurde. Die Selbstanregung der Wellen ist auf die freie Energie der Ionen zurückzuführen, die besonders in der Randschicht schnell durch die Mikroteilchenwolke strömen. Dieser Mechanismus erklärt ebenfalls die beobachtete Druckabhängigkeit der Anregungsschwelle. Mithilfe eines einfachen Modells der Mikroteilchendynamik ist es möglich, die Ladung der Teilchen abzuschätzen, die gut mit der vorhergesagten Ladung übereinstimmt. Selbstangeregte Wellen wurden weder durch Drucksenkung während des Parabelflugs induziert, noch dann, wenn die Teilchen durch die Thermophorese in der Mitte der Kammer levitiert wurden.

Mikroteilchenwellen in einem schwerelosen komplexen Plasma auf der ISS wurden durch eine Modulationsspannung extern angeregt. Zusätzlich zur vertikalen Oszillation mit der Anregungsfrequenz f_{mod} pflanzten sich Wellen in der vertikalen und horizontalen Richtung fort. Die horizontalen Schwingungen hingen nicht von f_{mod} ab. Als f_{mod} mit der Frequenz der horizontalen Wellen in Resonanz war, begann die Region der vertikalen Wellen, sich schräg in Richtung des Wolkenrands auszubreiten. Die Dispersionsrelation war quasischallartig. Um $f_{\mathrm{mod}} = 9\,\mathrm{Hz}$ war die Wellenaktivität auf die ganze Länge der Wolke verteilt. Bei höheren Frequenzen verschwanden die schrägen Wellen wieder. Die Teilchendynamik war ähnlich der in selbstangeregten Wellen im Experiment unter Gravitationsbedingungen.

Unter ähnlichen Bedingungen wie bei den selbstangeregten Wellen trat ein neues Phänomen nahe der Oberfläche der Teilchenwolke auf—die Bildung von Teilchenblasen, -tröpfchen und -spitzen. Das Verhalten der Mikroteilchen, z.B. Zerfallsmechanismen und Vortexbewegungen in den Tropfen betreffend, ähnelte dem der Moleküle in Flüssigkeitstropfen sowie sedimentierenden Teilchen. Die Druckabhängigkeit der Teilchengeschwindigkeit ist mit einem möglichen Kriechfluss des Gases in der Kammer kompatibel. Diverse Effekte deuten auf das Vorhandensein von Oberflächenspannung hin, z.B. die Entstehung von Spitzen mit Winkeln wie in Taylor-Kegeln, die selbstorganisierte Bildung runder Tröpfchen und der Aufbruch von Teilchenblasen. Außerdem wird eine qualitative Übereinstimmung der beobachteten Instabilität mit der Rayleigh-Taylor-Instabilität gezeigt.

Abstract

Complex plasmas consist of neutrals, ions, electrons and additional micrometer-sized grains. Fluxes of plasma particles onto the grain surface charge it, and the microparticles interact with each other. When the particles are illuminated, e.g., with a laser, recording the scattered light allows to perform fully resolved kinetic studies at all relevant frequencies, e.g., the Einstein frequency, Debye frequency, and plasma frequency.

In this thesis, dynamical effects in fluid complex plasmas are investigated using the PK-3 Plus setup, consisting of a radio-frequency plasma chamber, on the International Space Station (ISS), during a parabolic flight, and on the ground. The objective is the study of dynamical phenomena on the particle level, e.g., to determine when "corpuscular" effects become important and when fluid dynamics provides an accurate description. "Periodograms" are used to examine the global dynamic structures. Velocities and forces acting on individual particles were analyzed by studying the particle motion.

In the ground laboratory, self-excited highly resolved wave structures were analyzed. Thermophoresis was used to vary the extent to which the particles were pushed into the sheath regions of the chamber. The self-excitation of the waves is due to the free energy in plasma ions, which stream fast relative to the microparticles, especially in the sheath region. This excitation mechanism also explains the observed pressure dependence of the excitation threshold. Using a simple model of the microparticle dynamics, the grain charge is estimated, which agrees well with that calculated using known theories. Self-excited waves were neither observed when the particles were completely suspended in the center of the chamber by the thermophoretic force nor during dedicated experiments during the microgravity phase of the parabolic flight.

Microparticle waves were externally excited in a complex plasma under microgravity conditions on board the ISS by a variable, low frequency modulation voltage. In addition to the vertical slashing at the externally imposed frequency f_{mod}, waves propagated both in the vertical and horizontal direction. The horizontal oscillation did not depend on f_{mod}. When f_{mod} was resonant with the frequency of the horizontal oscillation, the excitation region of the vertically propagating waves started spreading obliquely towards the left part of the cloud. The dispersion relation of the oblique waves was quasi-sound like. Around $f_{\mathrm{mod}} = 9\,\mathrm{Hz}$, the wave activity spread over the whole cloud. At higher frequencies, the oblique waves disappeared. The particle dynamics resembled those accompanying the self-excited waves observed in the ground setup.

Under similar conditions as for the self-excited waves, a new phenomenon occurring near the surface of the particle cloud was investigated—the formation of microparticle bubbles, blobs, and surface cusps. The behavior of microparticles was similar to that observed in fluid drops and with sedimenting particles, including the breakup mechanism and vortex motion of particles inside the blobs. The forces acting on the microparticles are analyzed and the velocity scaling with pressure is shown to be compatible with a possible flow induced by thermal creep inside the plasma chamber. Various effects indicate the presence of surface tension, such as the formation of cusps with angles like in Taylor cones, the self-confinement of blobs inside the void, and the break-up of bubble lids. Qualitative agreement with the Rayleigh-Taylor instability is demonstrated.

Glossary

Constants

Symbol	Name	Value
ϵ_0	vacuum permittivity	$8.85 \cdot 10^{-12}\,\mathrm{F/m}$
e	elementary charge	$1.60 \cdot 10^{-19}\,\mathrm{C}$
g	gravitational acceleration on Earth	$9.81\,\mathrm{m/s^2}$
k_B	Boltzmann's constant	$1.38 \cdot 10^{-23}\,\mathrm{m^2kg/(s^2K)}$

Variables

Symbol	Name	Unit
α	surface tension	$[\mathrm{kg/s^2}]$
Γ	coupling parameter	*dimensionless*
γ_Ep	damping rate coefficient	$[\mathrm{s^{-1}}]$
γ	growth rate	$[\mathrm{s^{-1}}]$
γ_p	polytropic index	*dimensionless*
Δ	interparticle distance	[m]
ΔT	temperature difference between ground plates	[K]
δ_Ep	Coefficient in Epstein gas drag	*dimensionless*
η	(dynamic) viscosity	$[\mathrm{Pa \cdot s}]$
κ	thermal conductivity	$[\mathrm{W/(m{\cdot}K)}]$
κ^tr	translational part of thermal conductivity	$[\mathrm{W/(m{\cdot}K)}]$
λ_D	total Debye length	[m]
λ_c	ion mean free path	[m]
λ_Ds	Debye length of species s	[m]
μ	mobility	$[\mathrm{m^2/(s \cdot V)}]$
ν	kinematic viscosity	$[\mathrm{m^2/s}]$
ρ	mass density	$[\mathrm{kg/m^3}]$
τ	time constant	[s]
ϕ_E	electric potential	[V]
ϕ_fl	floating potential	[V]
ϕ_p	plasma potential	[V]
ω	angular wave frequency	[rad/s]
ω_gs	gyrofrequency of particle species s	[rad/s]

Symbol	**Name**	**Unit**
ω_{ps}	angular plasma frequency of species s	[rad/s]
A	voltage amplitude	[V]
a	acceleration	[m/s^2]
$\mathbf{B}$	magnetic flux density	[T]
C	capacitance	[F]
$\mathcal{C}$	capillary number	*dimensionless*
c	wave velocity	m/s
c_{DAW}	dust acoustic speed	m/s
c_{p}	specific heat capacity	[J/(kg·K)]
c_{s}	speed of sound	[m/s]
C_{T}	temperature jump length	[m]
d	distance	[m]
$\mathbf{E}$	electric field	[V/m]
E_{kin}	kinetic energy	J
$\mathbf{F}_{\mathrm{g}}$	force of gravity	[N]
$\mathbf{F}_{\mathrm{L}}$	Lorentz force	[N]
f_{mod}	modulation frequency	[Hz]
F_{net}	net force	[N]
$\tilde{g}$	effective gravity	[m/s^2]
$\mathcal{K}$	Knudsen number	*dimensionless*
k	wave number	[1/m]
L	length scale	[m]
l	length scale	[m]
$\mathcal{M}$	Mach number	*dimensionless*
m_{s}	mass of particle species s	[kg]
n_{s}	number density of particle species s	[kg/m^3]
ν_{sn}	collision frequency of particle species s with the neutral particles	[Hz]
p	pressure	[Pa]
P_{H}	Havnes parameter	*dimensionless*
q_{d}	charge of the microparticles	[C]
$\mathcal{R}$	Reynolds number	*dimensionless*
s	particle species $s = i, e, n, d$ meaning ions, electrons, neutrals, microparticles resp.	
t	time	[s]
T_{w}	wall temperature	[K]
$\mathbf{u}_{\mathrm{B}}$	Bohm velocity	[m/s]
U_{E}	electric potential energy	[J]
v	velocity	[m/s]

Symbol	Name	Unit
$\mathcal{W}$	Weber number	*dimensionless*
x	horizontal coordinate	[m]
x_{iz}	ionization degree	*dimensionless*
y	vertical coordinate	[m]
Z_{d}	number of electrons collected by microparticle	*dimensionless*

Acronyms

Notation	Description
3D	three-dimensional
ABR	Allen, Boyd, Reynolds
AC	alternating current
CCD	charge coupled device
DAW	dust acoustic wave
DC	direct current
DDW	dust density wave
DLR	Deutsches Zentrum für Luft- und Raumfahrt
DLW	dust lattice wave
DML	Drift Motion Limited
e.g.	exempli gratia—for example
FFT	Fast Fourier Transform
FoV	field of view
fps	frames per second
FWHM	full width at half maximum
i.e.	id est—that is
IDL	Interactive Data Language
ISS	International Space Station
ITER	International Thermonuclear Experimental Reactor
JIHT	Joint Institute for High Temperatures
LIC	line integral convolution
MF	melamine-formaldehyde
MPE	Max-Planck-Institut für extraterrestrische Physik
OML	Orbital Motion Limited
OQSW	oblique quasi-sound wave
PK-3	Plasmakristall-3 / Плазменный кристалл-3
PKE	Plasmakristall-Experiment / Експеримент “Плазменный кристалл”
RF	radio-frequency
SPIT	Super Particle Identification and Tracking
UV	ultraviolet

Chapter 1

Introduction

1.1 Dusty plasmas

In the shielded environment of our daily experience, we deal mainly with three states of matter: *solid* (without external forces, the matter maintains a fixed volume and shape), *liquid* (the volume of the matter is constant, but it adapts to the shape of its container), and *gaseous* (the matter expands to occupy whatever volume is available). It's only in extreme conditions where we encounter the fourth state of matter—the *plasma*, which is produced when electrons are detached from the atoms in a gas, producing free ions and electrons. The dynamics of the system is then largely controlled by the charged particles, even if the percentage of ionized atoms is low.

In general, a plasma in total is electrically neutral, but due to the presence of charged particles it can conduct electricity and interact with electric and magnetic fields. The ions and electrons also interact with each other, but as the interparticle forces are long-range, many particles are involved in this interaction, leading to a collective behavior of the whole plasma [1].

On Earth, natural plasmas occur very rarely. Figure 1.1 depicts two examples: *Flames* have some properties of plasmas, e.g., a non-negligible degree of ionization [2]. Atmospheric lightning is produced when ice and graupel particles inside a cloud acquire charges. The physical mechanism of the charging is still under debate. It is commonly believed to be

(a) *Flame of a candle.*

(b) *Lightning* (NOAO/AURA/NSF).

Figure 1.1: *Two examples of plasmas found on Earth.*

due to mutual friction (collisions) between the ice and the graupel [3]. Small particles tend to be charged positively, while bigger particles are predominantly charged negatively. The particles are separated by updrafts inside the cloud, so that high potentials are build up both inside the cloud as well as between the cloud and the ground. Eventually an electrical discharge between oppositely charged regions is formed - *lightning* [4]. In the lightning process, the air is ionized, and a plasma is generated.

Another example of naturally occurring terrestrial plasmas is the *ionosphere*, which is the ionized component of the Earth's upper atmosphere between 75 and 800 km height [5]. Ionization occurs by two different processes: photoionization, which is mainly due to ultraviolet (UV) and x-ray radiation from the sun, and impact ionization caused by impinging charged particles [5]. The resulting free electrons in the ionosphere reflect radio waves, as has been long known and used for communication.

In contrast, in space, 99 % of the visible matter is in the state of plasma [6]. *Stars* consist of a very hot plasma, producing energy by fusion of the atomic nuclei. The sun also ejects a continuous flux of plasma into the solar system, called *solar wind* [7]. The interaction of the solar wind and photons with the bodies in the solar system produces more plasmas: For instance, *comets* are heated when they approach the sun, emit gas, which is in turn ionized, forming a bright tail.

The magnetic field of the Earth forms a magnetic mirror for the charged particles from the solar wind, trapping them in the radiation belts and deflecting them towards the polar regions. When these particles hit the Earth's atmosphere near the poles, a plasma is produced, which can be observed in the form of *polar lights* [8]. Even outside the circumstellar regions, *interstellar atomic* or *molecular clouds* can be partly ionized by interstellar radiation and cosmic rays [9].

The solid matter in the universe is often in the form of small solid grains—"dust". Mixing these two components produces a *dusty plasma* [2, 10, 11][1]. The grains in such dusty plasmas acquire charges, for example by absorbing the fluxes of charged particles from the plasma onto their surfaces, or by photoemission. The dust then interacts with external electromagnetic fields and can affect the appearance and behavior of the plasma, e.g., creating new low frequency wave modes [14].

Dusty plasmas are ubiquitous in space [14]. For instance, in diffuse interstellar clouds, the dust component contains about 1 % of the total mass [9]. Figure 1.2 shows some more examples: *comets* possess separate ion and dust tails, which can be seen clearly in Figure 1.2a. Dust in planetary rings leads to the formation of optical depth modulations in planetary rings, which are called *spokes*. Examples in the rings of Saturn were first found with the Voyager spacecraft [16, 17] and then confirmed with the Hubble Space Telescope [18] and the Cassini spacecraft [19], as shown in Figure 1.2b. They appear dark in backscattered light and bright in forward-scattering. These structures cannot be explained by gravitational forces alone, but are thought to be composed of electrostatically levitated dust particles inside a short-lived, dense plasma near the rings [19–21]. Charged dust is also presumed to be important for the planet formation process in protoplanetary

[1] If the diameter of the dust particles is smaller than 1 µm and the sedimentation rate is low, one also speaks of *smoky plasmas* [12, 13].

(a) *The comet Hale-Bopp, featuring the distinct white dust tail and blue ion tail (J. Lodriguss).*

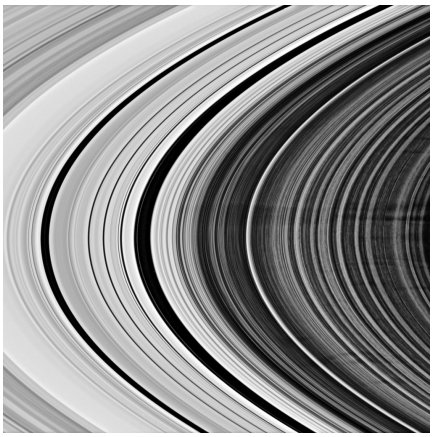

(b) *Spokes in the rings of Saturn recorded by the Cassini spacecraft (NASA/JPL/Space Science Institute).*

Figure 1.2: *Examples of dusty plasmas in space. From [15].*

disks: Opposite charges of the dust can significantly speed up the coagulation process [22].

"Dust" particles are also present in the lower parts of the Earth's ionosphere[2] and can be seen as illuminated clouds long after sunset in the summer months, the so-called *noctilucent clouds*. The presence of these clouds often coincides with strong radar backscatters, which have been shown to be associated with charged dust layers [23, 24], and consist of ice particles and possibly also smoke particles produced by meteorite impact in the atmosphere [25].

On Earth, the most common occurrence of plasmas are artificial ones, whether it be in lighting technology, fusion reactors or plasma processing techniques used for etching, thin film deposition, etc. In many of these systems, dust can seriously disturb the system or even destroy the product.

For instance, in fusion reactors, dust can either grow inside the plasma or be evaporated or sputtered from the walls [26–28]. This is not a problem for the current fusion experiments, but might prove a serious hinderance for the experimental reactor ITER, which is currently under construction in France. There, on the one hand, the dust is a safety concern due to radioactive activation of the grains, incorporation of tritium and beryllium, chemical reactivity and possible migration to and blockage of gaps or direct damage of the reactor blanket. On the other hand, dust could pose a threat to the operation of the fusion reactor: the incorporation of tritium into the grains uses up fuel which is not available for the fusion reaction, flaking of dust from the walls could disrupt the plasma, and the dust increases the plasma resistivity, leading to increased voltages needed for start-up [29, 30].

Another common application of plasmas is materials processing, e.g., new materials and surfaces can be manufactured, and structures can be etched into surfaces. Plasmas are especially important in the production of very large integrated circuits, where one third of the manufacturing steps are typically plasma-based [31]. In these reactive plasmas, dust

[2] In a region called *mesosphere*, at altitudes between 80 and 90 km.

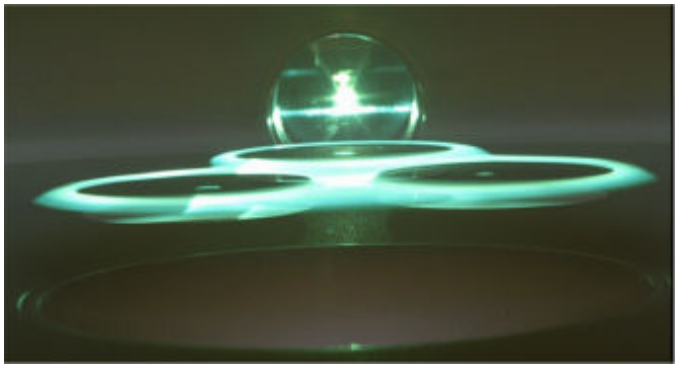

Figure 1.3: *Rings formed by dust suspended above three Si wafers, illuminated by a laser shining through the view port in the back of the picture. In the bottom, the graphite electrode is visible. From [35].*

growth by nucleation and agglomeration is a common process [32]. The central part of the plasmas, where electric fields are shielded by the free charged particles, (the *bulk* of the plasma) is surrounded by edge regions with strong electric fields, the *sheaths*. While the plasma is burning, dust particles acquire high charges and are suspended in these sheath regions of the discharge. When the plasma is turned off or the dust particles have grown to a size where levitation is no longer possible, they fall onto the wafer—the disc made of semiconductor material from which the integrated circuits are produced—and can cause voids or dislocations in the film and connect shorts, resulting in a decreased process yield and device reliability [33, 34]. Figure 1.3 shows dust levitated in a processing plasma.

However, nanoparticles in manufacturing plasmas can also have beneficial effects, for instance, the performance of solar cells can be improved, carbon-structures can be grown in plasmas, and the deposition rates in plasma enhanced chemical vapor deposition (PECVD) can be increased [32, 36]. There are also more indirect applications of dusty plasmas, for example sterilization of wounds with the help of atmosphere-pressure plasmas [37].

During studies in the laboratory, particles can be either grown inside the plasma as described above or inserted into the system with shakers. Under these controlled conditions, the systems are called *complex plasmas* to distinguish from the disordered systems with dust of various sizes occurring naturally [11]. When micrometer-sized particles (*microparticles*) are used, they can be illuminated by a laser and observed individually with a camera and magnifying lenses, so that the particle behavior can be studied on the atomistic (kinetic) level.

1.2 Strong coupling

In complex plasmas, the rate of momentum exchange through interactions between the microparticles can be much larger than that through other means, e.g., neutral drag [11]. Therefore, the microparticles can be treated as essentially single-species system regarding their dynamics.

The mobility of the electrons in discharges is so much higher than that of the ions that the electron flux to the grain surface strongly exceeds the ion flux. The microparticles therefore usually acquire high negative charges of the order of 10^3 or 10^4 electrons per particle. For this reason, the ratio of the Coulomb interaction between the particles to the

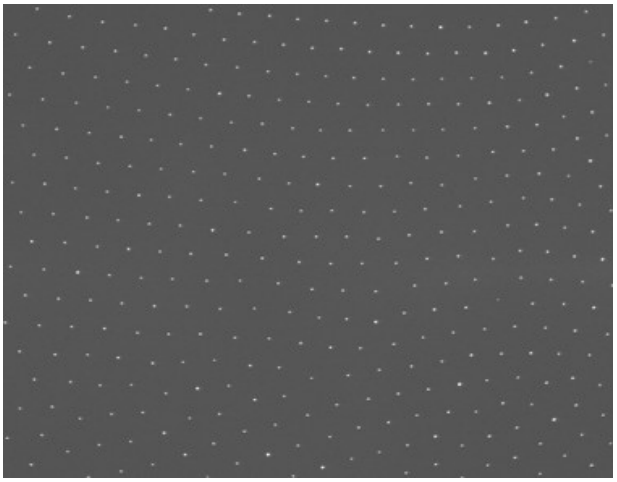

Figure 1.4: *Monolayer plasma crystal in an Air plasma at a pressure of 13.3 Pa consisting of 4.4 µm particles, seen from the top. The particles scatter the light of a laser beam, and are visible as white spots in the recorded image.*

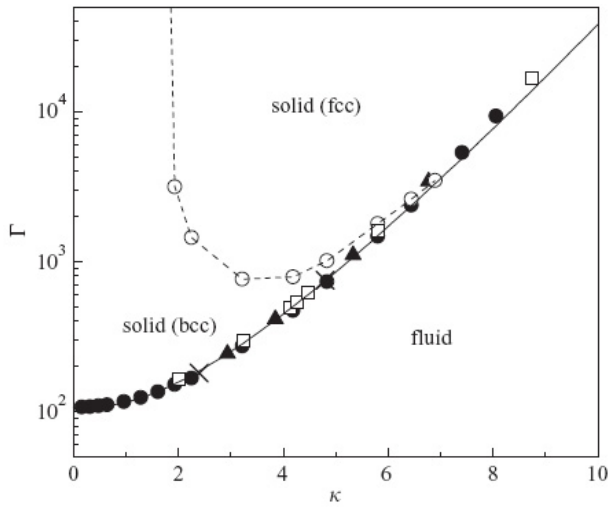

Figure 1.5: *Numerical simulation of the phase diagram of Debye-Hückel systems. From [11].*

kinetic energy (also called *coupling parameter*), can easily strongly exceed unity:

$$\Gamma = \frac{q_\mathrm{d}^2}{4\pi\epsilon_0 \Delta\, k_B T_\mathrm{d}} \gg 1. \tag{1.1}$$

Here, q_d is the microparticle charge, ϵ_0 denotes the vacuum permittivity, Δ is the mean distance between the particles, k_B represents Boltzmann's constant, and T_d designates the grain temperature. If Γ exceeds unity, one speaks of a *strongly coupled* system.

Wuerker, Shelton, and Langmuir [38] were the first to observe charged microparticles in an electrodynamic suspension system which arranged themselves in a quasicrystalline array that could also be melted. Ikezi [39] predicted the crystallization of grains in a plasma, which was later observed in radio-frequency (RF) discharges [40–43]—the *plasma crystal*. An example of a monolayer plasma crystal is depicted in Figure 1.4. These plasma crystals can be melted, making them simple and excellent model systems to study phase transitions and other such transformations.

Figure 1.5 shows the phase diagram in the Γ/κ-space. The so-called *structure* or *screen-*

ing parameter κ is defined as

$$\kappa = \Delta/\lambda_{\mathrm{D}}, \tag{1.2}$$

where λ_{D} is the plasma screening length, known as the *Debye length*. It can be seen from this diagram that complex plasmas can exist in solid and fluid states. At low Γ values, the system is always fluid, solidifying at higher values of the coupling parameter. Two possible solid states were found, body centered cubic (bcc) and face centered cubic (fcc). Experimentally, the solid phases of complex plasmas often coexist [11]. The liquid-solid phase transition, which can be induced by a change in gas pressure, has been investigated thoroughly [10, 44–46].

1.3 The influence of gravity on complex plasmas

In designing experiments with complex plasmas, the strong influence of gravity must be taken into account: Clouds of micrometer-sized particles levitating inside the presheath or sheath region are strongly compressed vertically by the gravitational influence of the Earth. This influence can be reduced by using smaller particles. Experimentally, it was shown that, e.g., nanometer-sized particles fill the whole chamber volume—but they are too small to be visualized individually [47]. Therefore, it is desirable to reduce the influence of the force of gravity in some other way as uniformly as possible.

Usually, gravity is compensated by levitating the particles in the sheath of the discharge, which is a region of positive space charge near the walls of the vacuum vessel [11]. In this region, an electric field is build up due to the potential difference between the bulk plasma and the walls. This field is strong enough to levitate micrometer-sized, strongly charged particles. For this reason, the particle cloud does not spread in the whole plasma chamber, but is restricted to the small region where the electric force balances gravity.

To perform measurements of large, three-dimensional isotropic systems, the experiments have to be performed under *microgravity conditions* [48]—environments in which the influence of gravity is strongly reduced or even negligible. A well-known method to achieve these conditions is by conducting experiments in space. However, there are ways to reduce the influence of gravity even on Earth.

1.3.1 Thermophoretic force

One possibility to increase the upwards force acting on the microparticles is to maintain a temperature gradient in the plasma chamber. Even without gas flux, there is a momentum transfer in the direction opposite to the temperature gradient: In a simplified picture, the temperature induced motion of the hotter gas particles is faster than that of the colder ones. Therefore, the hot atoms transfer more energy to the microparticle when they collide with the grain than the cold ones, resulting in a net force on the microparticle [49, 50]. Using this method, it is possible to lift the cloud of microparticles into the bulk of the plasma and observe many of the same phenomena as under microgravity conditions, e.g., the central particle free region (the *void*) [51]. Note that the strength of the thermophoretic

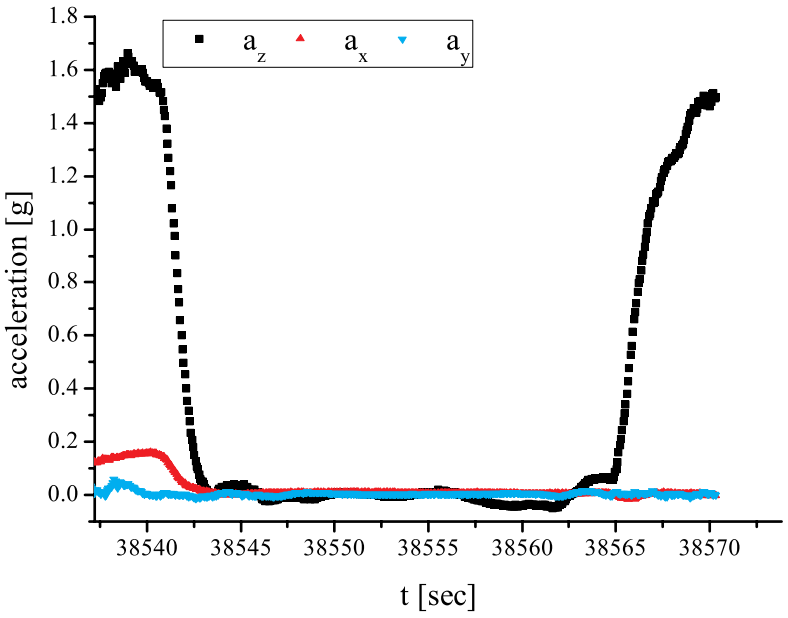

Figure 1.6: *Measured acceleration during a typical parabola flown with an Airbus A300 [52].*

force depends on the size of the microparticles, and thus leads to a separation of the particles of different sizes. The sheer magnitude of temperature differences needed to levitate microparticles also introduces new anisotropies into the system, and horizontal temperature gradients or gas convection induced by thermal creep may appear. Microgravity is therefore still preferable to produce large homogeneous systems of microparticles.

1.3.2 Parabolic flights

One way to eliminate the influence of gravity on Earth is letting the whole setup drop. *Drop towers* (like the one available at the university of Bremen) provide microgravity for about five seconds [53].

Much longer microgravity (about six minutes) than with drop towers is attainable with rockets on *ballistic flights*, e.g., in the TEXUS program [54]. There, it is possible to remotely control the experiments with tele-science. On *parabolic flights*, a plane performs a flight maneuver resulting in tens of seconds of weightlessness. In Europe, an Airbus A300 is used to achieve up to 22 s of low gravity (± 0.05 g) [55]. The experimenters can accompany the experiments themselves and react to the observations in real-time. Typical measured acceleration data is shown in Figure 1.6. The draw-backs are the relatively short duration and low quality of the weightlessness.

1.3.3 Experiments on board the space stations

The optimal way to perform experiments eliminating the influence of gravity is to use the International Space Station (ISS), where good microgravity conditions are realized [56]. There, comparatively vast three-dimensional (3D), homogeneous crystal and fluid complex plasmas can be studied [57–59].

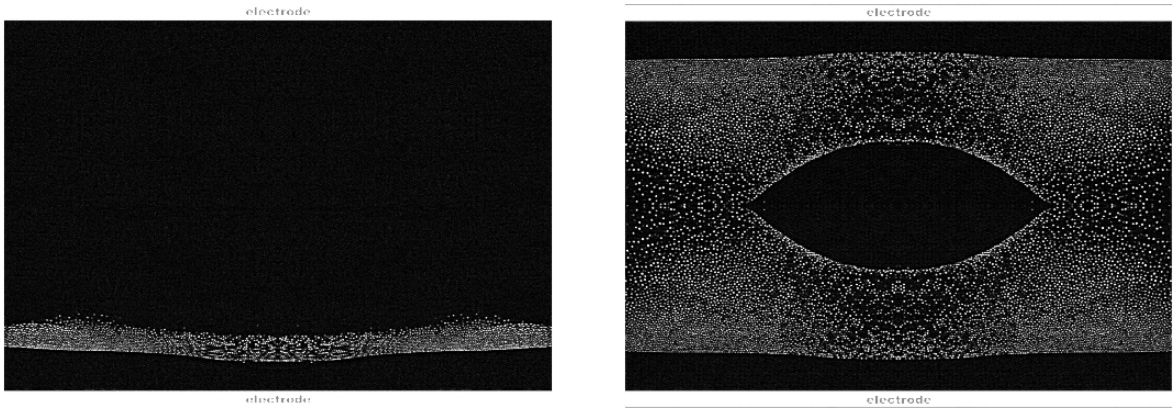

Figure 1.7: *A complex plasma consisting of 3.4 µm particles in the PKE-Nefedov setup under gravity conditions (left) and on board the ISS (right). From [59].*

The first two experiments on complex plasmas in space have been performed on board the Mir space station. In both experiments, the liquid behavior of charged microparticles was studied; the first, later dubbed "PK-1", consisted of a glass tube filled with microparticles of sizes between 1 and 100 µm in Neon gas at various pressures. The particles were exposed to solar radiation and charged by photoemission [60]. The second experiment, "PK-2", used a direct current (DC) discharge plasma with 100 µm bronze particles in Neon [61].

The next experiments on complex plasmas, PKE-Nefedov and PK-3 Plus[3], were performed on board the ISS in a collaboration between the Max-Planck-Institut für extraterrestrische Physik (MPE) and the Russian Joint Institute for High Temperatures (JIHT) [48, 58]. The experimental setups consist of parallel-plate plasma chambers. The plasma is ignited by applying an RF field to the electrodes. Microparticles of several sizes can be inserted into the system. (The experimental techniques are discussed in Chapter 3.) Figure 1.7 shows microparticle clouds in the PKE-Nefedov chamber under gravity (left) and microgravity (right) conditions. The strong compression of the particles by gravity in the left picture can easily be seen. Note the big central empty region, the *void*, under microgravity conditions. Typical are also convection rolls inside the microparticle cloud on the edges of the system.

1.4 Complex plasmas as model systems

Complex plasmas can also serve as excellent model systems for studying phase transitions, particle transport, waves, etc., with the great advantage that the processes can be observed at the kinetic (atomistic) level.

A good example are liquid complex plasmas, which have been the topic of several investigations, e.g., concerning shear flow and instabilities [62]. It is worth to note that the similarity parameters, the *Reynolds* and the *Mach numbers*, of these systems can match

[3]The setup that was also used in the experiments presented in this thesis.

those of water.

1.4.1 Similarity parameters

The *Reynolds number* $\mathcal{R}$ is a measure of the ratio of inertia forces to viscous forces

$$\mathcal{R} = \frac{vL}{\nu_\mathrm{d}}, \tag{1.3}$$

where v is the hydrodynamic velocity of the particles, L denotes a characteristic length, and ν_d is the kinematic viscosity. The magnitude of the Reynolds number determines whether a flow is laminar or turbulent; the higher $\mathcal{R}$, the stronger inertia forces and the more turbulent the flow.

Nosenko and Goree [63] investigated the viscosity of complex plasmas by pushing the grains with a laser beam. They measured $\nu_\mathrm{d} \sim 1\,\mathrm{mm}^2/\mathrm{s}$, which corresponds to $\mathcal{R} = 0.7$–17. Morfill et al. [64] find $\mathcal{R} = 5$–50 in the flow of microparticles around an obstacle in a complex plasma using $\nu_\mathrm{d} = (1\text{–}10)\,\mathrm{mm}^2/\mathrm{s}$ from numerical simulations. The value of the kinematic viscosity is similar to that of water, $\nu_\mathrm{W} \sim 1\,\mathrm{mm}^2/\mathrm{s}$ [65].

The *Mach number* $\mathcal{M}$ is defined as

$$\mathcal{M} = v/c_\mathrm{s}, \tag{1.4}$$

where c_s is the velocity of sound. For complex plasmas, the relevant velocity c_DAW is that of dust acoustic waves (DAWs) [64] or, if the system is strongly coupled, dust lattice waves (DLWs) [66–68]. Morfill et al. [64] estimate $c_\mathrm{DAW} \simeq 1.4\,\mathrm{cm/s}$, resulting in $\mathcal{M} \simeq 0.5$. Samsonov et al. [66] find Mach cones in a plasma crystal with $\mathcal{M} = 1.81 \pm 0.15$, and in [67] and [68], a wide range of Mach cones with $\mathcal{M} \leq 6$ is observed.

These parameters indicate that complex plasma fluids behave similarly to water, observed at the molecular level. This allows investigations of fluid flows on the equivalent of the "nanoscale" [62, 64].

1.4.2 Hydrodynamic instabilities

The most important hydrodynamic instabilities are the *Kelvin-Helmholtz instability*, which occurs when velocity is sheared between two layers, and the *Rayleigh-Taylor instability*, arising when a dense fluid is accelerated into a less dense one. Kelvin-Helmholtz instabilities can, for instance, be induced when wind is blowing over a water surface. A prominent example of the Rayleigh-Taylor instability is seen in planetary nebulae [69], which are the remnants of dying stars. There, successive layers of the star's atmosphere are ejected and interact with the interstellar medium, forming the instability. Typical are pronounced fingers at the interface between the two media.

An interesting question is whether these effects survive on the interparticle distance scale, and whether they have a kinetic trigger [62, 70]. An example of a hydrodynamic instability triggered inside the complex plasma cloud has been found by Morfill et al. [70] (Figure 1.8). In this experiment, microparticles flowing along the surface of a plasma crystal are investigated. If the surface is flat (Figure 1.8a), the flow is stable and laminar,

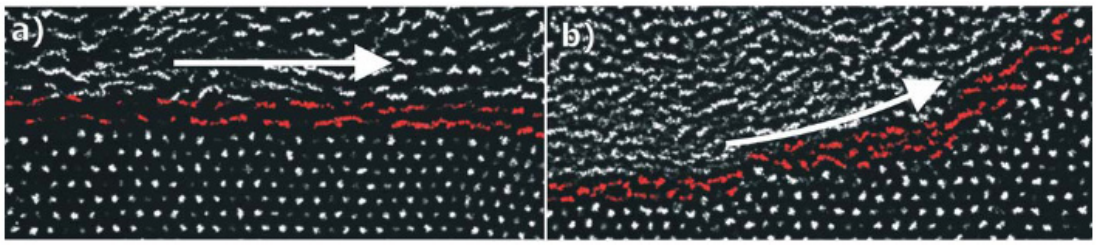

Figure 1.8: *Two examples of flowing complex plasmas. a) Shear flow over a flat plasma crystal. b) Flow over a curved plasma crystal. From [70].*

and the particle trajectories are almost parallel to the plasma crystal surface, showing almost no deformations.

If the surface of the plasma crystal is curved (Figure 1.8b), a mixing layer is formed between the flowing region and the crystal. This layer becomes unstable, and the particle trajectories are deformed. The cause of this is the centrifugally driven Rayleigh-Taylor instability, arising at the interface between the stable and the flowing microparticles.

Another such mixing layer has been observed at the interface of a flow of microparticles around an obstacle and the wake behind this obstacle [64], which has been interpreted as a new type of nonlinear collisional instability.

These examples demonstrate that effects of macroscopic liquids can also be present in complex plasmas. Complex plasmas can as well serve as a tool for investigating waves and wave-induced dynamical effects in fluid complex plasmas.

1.5 Complex plasma modes

Normal modes of complex plasmas are an important field of study as they provide a good way to test theories in experiments. *Vertical oscillations of single particles*, for instance, have been used to estimate the charge of the microparticles [43]. *Mesoscopic complex plasmas*, e.g., Coulomb clusters[4], exhibit normal modes that are dominated by finite-size effects [71–73].

Typical modes occurring are the *slashing mode*, which is a center of mass movement of the whole particle cloud, and the *breathing mode*, which is a radial compressional movement of the particles with the center of the particle cloud as node. These modes also exist for big microparticle clouds. A mode of vast complex plasma clouds with a central void similar to the breathing mode is the *heartbeat instability* [74], which is a quasi-periodical radial contraction and successive expansion of the void and corresponding microparticle motion, reminding of the beating of a heart.

In these systems, *microparticle waves* occur as well, which are governed by dispersion relations. The most ubiquitous waves are the dust acoustic waves (DAWs) [75, 76] and dust density waves (DDWs) [77, 78], which are *compressional (longitudinal) waves* in the microparticle component of the complex plasma. It is usually believed that DDWs

[4]Finite clusters with a small number of particles, usually confined by an additional glass box placed on the lower electrode of the discharge chamber.

resemble DAWs [79], but for more complicated conditions (and, hence, more adequate to the experiments), like highly collisional plasmas with drifting ions. Since the microparticles are heavier than the plasma ions, their presence can also modify the dispersion relations of normal plasma modes [80].

Dust waves in strongly coupled complex plasmas are called dust lattice waves (DLWs). In plasma crystals, waves exist in the compressional [81] and also in the *shear (transverse)* mode [82], and can be excited externally, for instance by pushing the crystal from one side with a focused laser beam. In the liquid phase of complex plasmas, both transverse and longitudinal waves exist [83–85]. In contrast, in the gaseous phase of complex plasmas, only the compressional waves occur.

DAWs were first predicted by Rao, Shukla, and Yu [75] and have since been studied theoretically in a number of publications [79, 80, 86–93].

The DAW is an attractive object from a theoretical point of view because of its supposedly simple physics: The plasma ions and electrons can be treated as inertialess; their role is to maintain the fields driving the microparticles. Idealized nonlinear theoretical models have been considered for collisionless soliton-like DAWs [94] and for nondispersive DAW shocks [95]. Nonlinear theoretical models, adequately describing DDWs, are still under debate.

From the observational point of view, wave experiments in a complex plasma have the advantage that the particles can be traced individually on the kinetic level. Dust acoustic waves have been investigated experimentally, among others, in RF discharges on ground [96, 97] as well as under microgravity conditions on the ISS [91, 98] and in parabolic flight experiments [79], in DC discharges [89, 90, 99–104], in Q-machines [80, 87], and in magnetized systems [105, 106]. DAWs with an infinitesimally small amplitude are called *linear*. Usually, the observed waves are treated as linear, which is substantiated by adjusting unknown parameters to suit theoretical predictions [75]. The wave parameters measured this way can be successfully used to estimate the charge of the particles [91, 98, 103].

1.5.1 Self-excited dust density waves

Self-excited waves (*autowaves*) are an important element of self-organization in nature [108]. For instance, they are observed in plastic deformation flows [109], in hydrothermal flows [110], or formed by striations in discharges [111]. Rhythmic patterns of mobile marine sandy beds, sand ripples and dune patterns are usual in deserts and along coasts [112–114]. Examples of autopatterns are shown in Figure 1.9. The common feature of these phenomena is that the pattern-forming medium is in an active state due to external tension or has an active agent (wind, water, plasma ions, etc.).

As mentioned above, waves in fluid complex plasmas, such as those shown in Figure 1.9d, appear when a control parameter is properly adjusted, e.g., when the pressure is reduced [105], or the discharge current is increased [80]. They normally flow in the direction of the ion drift in the discharge, and are thought to be caused by this ion drift through the microparticle cloud [80, 116]. Fortov et al. [117] showed that microparticle charge variations can also contribute.

gas	pressure [Pa]	particle size [µm]	particle type	f_{mod} [Hz]	v_{ph} [mm/s]	reference
$SiH_4/O_2/Ar$	$\leq 13\,\mathrm{Pa}$	~ 1	SiO_2	—	~ 60	[105]
N	9	1–15	Kaolin	—	90	[87]
N	9–13	0.5–1	Kaolin	5–40	120	[89]
N	13	~ 1	Kaolin	0, 6–30	120	[80]
Ne	40	1.87	MF	—	20	[90]
Ar	12–20	2.9, 40	SiO_2	—	5–100	[100]
Ar	24	3.4, 6.8	MF	0–16	8	[91]
Ne	10–50	1.87	MF	—	23–83	[97]
Ne	40	1.03	MF	gas flow of 0.1 s	18	[101]
Ar	15	6.8	MF	—	16–17	[79]
Ar	12–18	15	SiO_2	—	5	[102]
Ar	2	0.93	MF	—, 16–37	100–200	[106]
Ar	12	3.4	MF	0–35	17–25	[98]
Ar	25	1.28	MF	—	56	[107]
Ar	13–26	~ 1	Kaolin	0, 15–150	~ 100	[103]

Table 1.1: *Phase velocities v_{ph} of dust waves observed under various experimental conditions. The frequency of the external modulation used to excite the waves is designated by f_{mod}.*

Whether DAWs can be self-excited under microgravity conditions is still under debate. Waves are very common during experiments on parabolic flights, but the microgravity conditions in these experiments are unstable; often the microparticle cloud is pushed into the upper or lower sheath by fluctuating vertical accelerations. Piel et al. [79] have repeatedly observed stable waves at low pressures and no waves at higher pressures, while in other experiments, even at low pressures, waves do not occur in a repeatable manner [118]. So far, no self-excited waves have been observed on board the ISS even at the lowest attainable pressures. This discrepancy might be due to differences in discharge power or gas pressure. Experiments with parameters under which waves are observed during parabolic flights are planned in future missions on board the ISS [118].

1.5.2 Externally excited dust density waves

A common method to study the dispersion relation of the DAWs is to excite the waves externally with a known frequency, for example by applying a modulating voltage to the discharge electrodes. In these studies, until recently, it was normal practice to assume that the frequency of the excited waves was equal to that of the applied modulation [80, 89, 91, 96, 98]. For instance, in [91] and [98] waves are excited externally under microgravity conditions in the PKE-Nefedov setup [58], and the dispersion relations are studied by varying the modulation frequency (and the amplitude) in the range (0–35) Hz. In both cases, by adjusting the microparticle charge, it is possible to fit the experimental dispersion

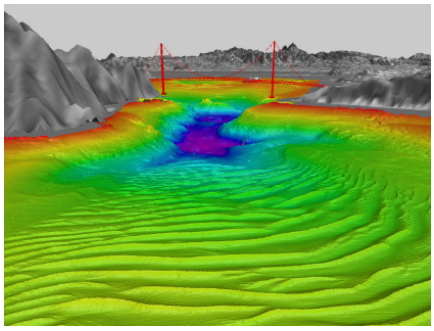

(a) *Marine sand waves in the bay near San Francisco. From [115].*

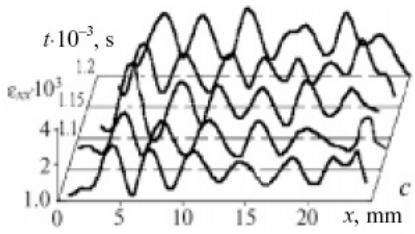

(b) *Steady-state strain localization pattern of Zr + 2.5 % Nb. From [109].*

(c) *Sand ripples in dunes. Picture courtesy of M. Kretschmer.*

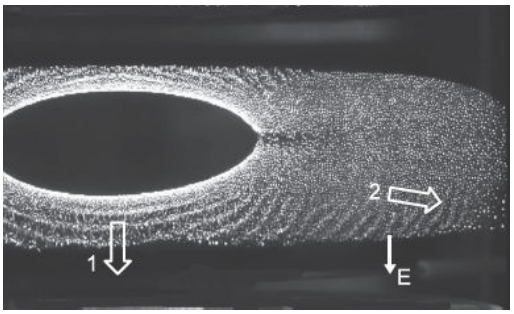

(d) *Dust density waves in a complex plasma. From [79].*

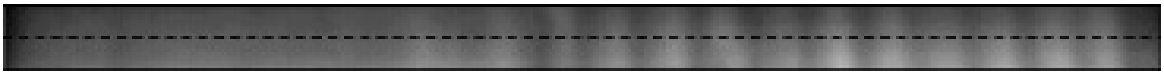

(e) *Hydrothermal flow pattern. From [110].*

Figure 1.9: *Examples of autowaves found in nature.*

relation to the theoretical one. In [91], the DLW dispersion relation also matches the experimental one.

The situation can be more complicated than in the simple picture explained above: The induced waves can co-exist with self-excited ones. Thomas, Fisher, and Merlino [103] study this phenomenon in a DC discharge at modulation frequencies higher than 100 Hz. They find a linear superposition of self-excited and driven wave modes. Additionally, they demonstrate a deviation from the linear model which they ascribe to finite dust temperatures.

1.6 Fluid effects

1.6.1 Drops

Another interesting effect of conventional liquids is the formation and break-up of drops. The break-up of liquid drops in an air stream or that of a blob of sedimenting particles

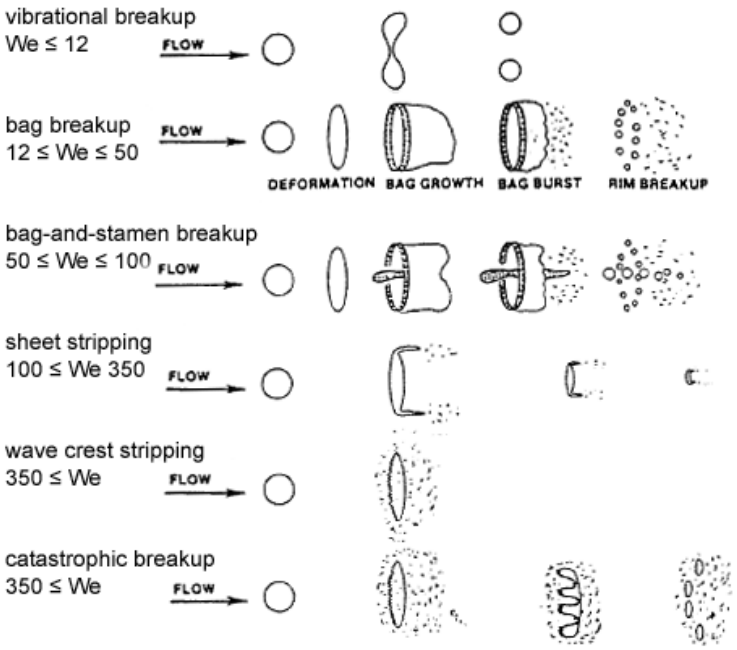

Figure 1.10: *Break-up mechanisms of water drops in a gas stream realized at various Weber numbers. From [123].*

in a liquid has been of long interest, starting with the fall of rain drops [119]. It has been investigated in free fall experiments, wind tunnels, shock tubes, and others [120, 121]. Different breakup mechanisms are possible [122] depending on the Weber number $\mathcal{W}$ of the system, which is a measure of the ratio of inertia to surface tension forces

$$\mathcal{W} = \frac{\rho v^2 l}{\alpha}. \tag{1.5}$$

Here, ρ is the mass density of the drop, v represents the drop velocity, l denotes the length scale, and α is the surface tension.

Which break-up mechanism is realized depends on the Weber number (Figure 1.10). For low $\mathcal{W}$, for example, bag breakup is likely: the drop first deforms into a bag shape, then bursts in the center. For intermediate $\mathcal{W}$, a probable breakup mechanism is sheet stripping, where particles are emitted from the sides of the drop, forming pointed edges. At high $\mathcal{W}$, catastrophic breakup and wave crest stripping can occur, whereby the drop disintegrates on the sides [122].

The fluid movement inside a falling water drop is investigated in detail by Han, Stapf, and Blümich [124], revealing large convection rolls inside the drop in the case of pure distilled water. In the case of a surfactant drop, much less movement is found.

Remarkably, the behavior of a blob of sedimenting (mesoscopic) particles in a liquid can be very similar to that of a pure water drop. Depending on whether the particles are so small that a continuum description is applicable or not, these systems are called either *suspension drops* or *blobs*. The analogy between suspension drops and liquid drops is fundamental without interfacial tension needed. For instance, the drops form membranes when breaking up, show similar vortices as found inside water drops [121, 124], and sometimes emit single particles, forming a tail [125]. With the help of these sedimentation

studies it is possible to investigate the movement of individual particles in an ensemble or blob.

1.6.2 Bubbles

The complementary problem to blobs, bubbles in a fluidized bed, is also of interest. An ensemble of particles is *fluidized* if its weight is completely supported by an upward flow of fluid [126]. The behavior of these systems depends on the size of the supported particles and the streaming speed of the fluid. When a gas is used as fluidization agent, bubbles are formed frequently. The gas inside one of these bubbles moves in a vortex, pushing the particles out and forming an "empty" void [127]. The supporting gas can also be ionized, producing a plasma-fluidized particle bed. There have been investigations of strong coupling effects between the particles in a plasma-fluidized bed [128].

Many other bubble-forming systems exist, e.g., electron bubbles at the solid-superfluid interface of helium under the influence of an electric field [129].

1.6.3 Bubbles and drops in complex plasmas

The systematic study of bubbles, blobs, and droplets in complex plasmas started relatively recently even in the young field of complex plasmas.

Clusters consisting of a small amount of microparticles can be formed by applying additional confinement to the particles, for example by placing an additional glass box on the lower electrode (to form Coulomb clusters) [130], or by applying an additional potential to a small part of the lower electrode via an "adaptive" electrode [131, 132]. Antonova et al. [132] demonstrated the existence of attractive forces between the microparticles in small clusters.

Recently, a cluster formed of a big central particle and several smaller ones was observed in a DC plasma by Usachev et al. [133]. The confinement of the cluster of like-charged particles is provided by plasma flux onto the central particle.

Mikikian et al. [47] found an ensemble of smaller microparticles inside the void under microgravity conditions in the PKE-Nefedov setup. The microparticles were pushed quasi-periodically through the center of the void, where the ensemble disintegrated. When it reached the opposite void boundary, the ensemble reformed. The particles were not confined for extended periods, but visually resembled blobs for short moments of time.

The sizes of "microvoids" or bubbles in complex plasmas typically range from hundreds of microns to a few millimeters. They can occur under the influence of forces, for instance in complex plasmas in strong magnetic fields [134]. They also have been artificially produced by Chu et al. [135] by ablating some microparticles with a strong, sharply focused laser pulse. The resulting plume of ablated material pushed the surrounding microparticles outwards, creating a particle-free region. Depending on the plasma parameters, the resulting bubbles did not immediately collapse, but moved downwards at speeds of (5–6) cm/s and exited the microparticle cloud. They interacted with the surrounding microparticles, exciting their oscillations and waves.

To the best of the author's knowledge, self-formed dynamical structures resembling drops and bubbles have not been observed in complex plasmas before.

1.7 Contributions of this thesis

In this thesis, many phenomena of fluid systems in complex plasmas under the influence of various external forces are studied using the PK-3 Plus setup. The experiments were performed partly at the MPE (under gravity conditions), partly by cosmonauts/astronauts on the ISS and partly during a parabolic flight (13th campaign by the Deutsches Zentrum für Luft- und Raumfahrt (DLR)).

In order to shed light on the atomistic processes occurring within self-excited dust density waves, the ground setup was used with a high-resolution, high speed data acquisition system. It was possible to trace the motion of the microparticles at a time scale of one ms/frame and subpixel resolution while they were captured by the wave ridges, moved within them and then were released again, falling back towards their original positions. This made it possible to investigate the force and velocity fields and to estimate the charge of the microparticles on the basis of a simple model incorporating the particle flux balance.

The mechanism exciting the DDWs was studied by investigating the instability threshold of the waves under the influence of a variable thermophoretic force (in the range of (1–4) g) and comparing with a model explaining the waves in terms of the ion flux. The method of *periodgrams* (Section 3.3.1) was adapted to find the wave parameters.

In order to narrow down the origin of self-excitation under microgravity conditions, self-excited waves on a parabolic flight were also briefly examined.

The microgravity conditions of the ISS are best suited for experiments on externally excited dust density waves. In this system, intense oscillations and nonlinear waves were excited by a function generator. A previously unknown complex dependence of the response of the microparticles on the exciting frequency was demonstrated. Even without external modulation, a horizontal oscillation at the frequency of 5 Hz was observed. Increasing the modulation frequency widened the spectrum: The modulation first excited a global vertical slashing mode (at the modulation frequency). At a frequency of 3 Hz intense shaking induced periodic nonlinear wave-ridges in the bottom and top parts of the cloud. The ridges traveled at an approximately constant speed of (4–5) mm/s. The modulation also intensified the horizontal waves localized at the horizontal cloud edges, though the regions of intensive waves were visibly disconnected. At higher frequencies, the intense wave activity involved all the cloud, and "oblique" quasi-sound wave-ridges started to propagate through the cloud. The distribution of velocity and force fields was also studied.

Furthermore, a novel phenomenon of fluid complex plasmas was investigated in the laboratory on ground under similar conditions as the self-excited waves: the formation of bubbles, blobs, and surface cusps in the microparticle cloud at low discharge powers and under the influence of thermophoresis. It was possible to turn the activity on and off by changing control parameters like the applied temperature gradient or the pressure. A detailed analysis of these structures, the movement of the microparticles within them and

the dependence on the various control parameters was performed, and they were compared with similar phenomena in conventional liquids and sedimenting particles. Several effects indicating the presence of surface tension were observed, even at the small "nano-scales" of a few hundreds of particles. A possible mechanism, analogous to the Rayleigh-Taylor instability, that could drive the instability is proposed. Experiments dedicated to the formation of the same instability under microgravity conditions are also briefly discussed [136].

Before presenting the experiments in detail, an introduction to the basics of the theories needed to describe complex plasmas is given in the following.

Chapter 2

Theory

2.1 Weakly ionized plasmas

Laboratory experiments on complex plasmas are often performed in weakly ionized plasmas that are driven electrically at frequencies that the massive ions cannot follow. This way, free electrons are accelerated by the electric fields to velocities high enough to ionize additional atoms, until a balance between ionization and recombination (e.g., at the chamber walls) is reached. The velocity of the electrons is limited by collisions with atoms.

The ionization degree x_{iz} is defined as the ratio of the ion number density n_{i} to the total particle density

$$x_{\mathrm{iz}} = \frac{n_{\mathrm{i}}}{n_{\mathrm{i}} + n_{\mathrm{n}}}, \tag{2.1}$$

where n_{n} is the number density of the neutral particles. In discharges of this type, x_{iz} is very small ($x_{\mathrm{iz}} \ll 1$), which explains the term *weakly ionized plasmas* [31]. Under these conditions, the collisions of ions with neutrals are dominant compared with ion-ion and ion-electron collisions. Therefore, the ion temperature is of the order of the temperature of the neutral gas, which is usually around room temperature. For this reason, these plasmas are also called *low temperature plasmas*. In contrast, the lighter electrons are efficiently heated by the applied field, and have a much higher energy of the order of a few eV; the system (atoms-ions-electrons) is hence not in thermal equilibrium.

If a test charge q is introduced into a plasma, its Coulomb potential is screened by the free ions and electrons surrounding it. The electric potential ϕ_{E} is related to the charge densities by Poisson's equation

$$-\nabla^2 \phi_{\mathrm{E}}(r) = \nabla \cdot \mathbf{E} = \frac{e}{\epsilon_0} \left(n_{\mathrm{i}} - n_{\mathrm{e}} \right). \tag{2.2}$$

Here, $\mathbf{E}$ represents the electric field, e denotes the (positive) elementary charge, ϵ_0 is the vacuum permittivity, and n_{i} and n_{e} are the number densities of the ions and electrons, respectively. If the test charge introduces only small disturbances (far-field approximation), and Boltzmann distributions of the electron and ion densities and single-charged ions are assumed:

$$n_{\mathrm{i}} = n_{\mathrm{i0}} \exp\left(-\frac{e\phi_{\mathrm{E}}}{k_{\mathrm{B}} T_{\mathrm{i}}} \right) \approx n_{\mathrm{i0}} \left(1 - \frac{e\phi_{\mathrm{E}}}{k_{\mathrm{B}} T_{\mathrm{i}}} \right), \tag{2.3}$$

$$n_{\mathrm{e}} = n_{\mathrm{e0}} \exp\left(+\frac{e\phi_{\mathrm{E}}}{k_{\mathrm{B}} T_{\mathrm{e}}} \right) \approx n_{\mathrm{e0}} \left(1 + \frac{e\phi_{\mathrm{E}}}{k_{\mathrm{B}} T_{\mathrm{e}}} \right), \tag{2.4}$$

the Poisson equation (2.2) is solved by the well-known *Debye-Hückel potential*

$$\phi_{\mathrm{E}}(r) = \frac{q}{4\pi\epsilon_0 r} \exp\left(-\frac{r}{\lambda_{\mathrm{D}}}\right). \tag{2.5}$$

The screening length λ_{D} is the *total Debye length*

$$\lambda_{\mathrm{D}} = \left(\lambda_{\mathrm{De}}^{-2} + \lambda_{\mathrm{Di}}^{-2}\right)^{-1/2}, \tag{2.6}$$

where $\lambda_{\mathrm{Ds}} = \sqrt{\epsilon_0 k_{\mathrm{B}} T_{\mathrm{s}}/n_{\mathrm{s}} e^2}$ is the Debye length of particle species s (electrons or ions). The total Debye length is thus the distance from the test particle where its potential is attenuated to 1/e (only here, e denotes Euler's number, the base of the natural logarithm) of the original strength due to screening by the other plasma particles. The reason is that particles with charges of opposite sign are attracted by the test particle and same-charge particles are repelled, leading to the build-up of a spherical space charge of opposite sign shielding the field of the test charge.

In a plasma, significant non-compensated charge densities can spontaneously exist only on the length scale defined by the Debye length. Far away from the ensemble of test charge and screening charges (at distances much greater than the Debye length), the potential of the field drops very fast, and the plasma is *quasi-neutral*

$$n_{\mathrm{i0}} = n_{\mathrm{e0}}. \tag{2.7}$$

The plasma particles interact with each other via electromagnetic fields. In an ideal plasma, the number of particles which are close enough to each other to feel the spontaneous plasma fields (closer than the Debye length) has to be high, for instance for the total number of electrons in a Debye sphere

$$N_{\mathrm{e}} = \frac{4\pi}{3}\lambda_{\mathrm{D}}^3 n_{\mathrm{e}} \gg 1 \tag{2.8}$$

holds. This condition is also called the *plasma condition*. It leads to the emergence of collective effects. Additionally, the total dimension of the system L has to be large compared to the Debye length, so that effects taking place on the border of the system are not dominant:

$$L \gg \lambda_{\mathrm{D}}. \tag{2.9}$$

By considering a small disturbance in the position of the charge carriers, it can be shown that the perturbed charge densities in a plasma oscillate at a characteristic frequency, the plasma frequency ω_{ps} of particle species s:

$$\omega_{\mathrm{ps}} = \sqrt{\frac{e^2 n_{\mathrm{s}}}{\epsilon_0 m_{\mathrm{s}}}}. \tag{2.10}$$

Electromagnetic waves with frequencies lower than the plasma frequency are screened by the charged particles and cannot penetrate deep into the plasma.

2.1.1 Sheaths

Just after the initial ignition of a discharge, the more mobile electrons are lost to the chamber walls surrounding the plasma faster than the heavier ions. This results in the build-up of a positive space charge in the region near the walls and the subsequent generation of a potential barrier confining the electrons in the plasma: the *confinement potential*. The resulting field decelerates the electrons approaching the walls and accelerates the ions towards the walls. The region where this happens is called the *sheath* [31].

Inside the sheath, the quasi-neutrality condition (2.7) is violated because of the net positive space charge. Bohm [137] showed that the ions have to enter the sheath with a velocity greater than or equal to the *Bohm velocity*

$$v_{\mathrm{is}} \geq u_{\mathrm{B}} = \sqrt{\frac{k_{\mathrm{B}} T_{\mathrm{e}}}{m_{\mathrm{i}}}} \tag{2.11}$$

in order to fulfill the ion continuity and energy conservation conditions.

In contrast, inside the *bulk* of the plasma (the region of the plasma enclosed by the sheaths), the ion velocity must be less than the Bohm velocity in order to preserve quasi-neutrality. Even outside the sheath, an electric field has to penetrate into the plasma so as to accelerate the ions to the Bohm velocity. This region of the plasma is called the *presheath*, and is typically much wider than the sheath region [31].

2.1.2 Screening

In the bulk of the plasma (far from the sheaths), the Debye length (2.6) can be approximated by the ion Debye length

$$\lambda_{\mathrm{D}} \approx \sqrt{\frac{\epsilon_0 k_{\mathrm{B}} T_{\mathrm{i}}}{e^2 n_i}} \equiv \lambda_{\mathrm{Di}}\,, \tag{2.12}$$

since the electron temperature is much higher than the ion temperature, and the contribution of the electrons to screening can be neglected. In the sheath, on the other hand, the ions stream so fast that their contribution to screening is small, and the Debye length is close to that of the electrons [138]

$$\lambda_{\mathrm{D}} \approx \sqrt{\frac{\epsilon_0 k_{\mathrm{B}} T_{\mathrm{e}}}{e^2 n_e}} \equiv \lambda_{\mathrm{De}}\,. \tag{2.13}$$

Typical parameters of experiments with complex plasmas are $T_{\mathrm{e}} = 3\,\mathrm{eV}$, $T_{\mathrm{i}} = 300\,\mathrm{K}$ and $n_{\mathrm{i}} = n_{\mathrm{e}} = 10^{14}\,\mathrm{m}^{-3}$, yielding $\lambda_{\mathrm{Di}} = 120\,\mu\mathrm{m}$ and $\lambda_{\mathrm{De}} = 1.3\,\mathrm{mm}$.

2.1.3 Radio-frequency plasmas

One method to ignite weakly ionized plasmas is to apply an alternating current (AC) high-frequency field via two parallel electrodes. Figure 2.1 depicts such a setup, where the electrodes are driven symmetrically, and a blocking capacitor is used to prevent any

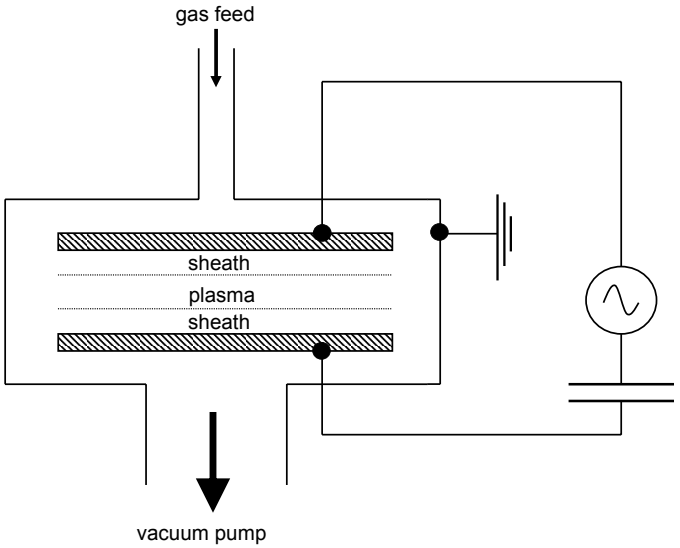

Figure 2.1: *Schematics of a symmetrically driven capacitively coupled radio-frequency plasma chamber, after [31]. A blocking capacitor is used to prevent any DC currents from flowing.*

DC currents from flowing [139]. Not shown in the figure is the matching network, which is used to match the impedance of the circuit to that of the plasma and sheath inside the reactor, maximizing the power transfer to the plasma.

Usually, the industrial frequency of 13.56 MHz is used as driving frequency, explaining the name *RF plasma*. The electrons are light enough to be able to follow the applied alternating field, while the ions are so massive that they only react to time-averaged fields. In radio-frequency plasmas, the plasma densities are typically relatively low, $(10^{15}$–$10^{17})\,\mathrm{m}^{-3}$ (and can be even lower), and electron temperatures are of the order of (3–4) eV (in Argon) [31, 48, 140].

2.2 Complex plasmas

When micrometer-sized grains (*microparticles*) are introduced into a plasma, ions and electrons strike their surface. As the electrons are more mobile than the ions, the grains acquire high negative charges, whereby the magnitude of the charge depends on the properties of the grain itself and on the properties of the plasma [141].

The microparticles therefore introduce a new charged species into the plasma. The basic properties of plasmas discussed above still hold, such as quasi-neutrality on length scales $l \geq \lambda_\mathrm{D}$ [2],

$$n_\mathrm{i} = n_\mathrm{e} + Z_\mathrm{d} n_\mathrm{d}. \tag{2.14}$$

Here, Z_d is the mean number of elementary charges accumulated on each microparticle, which is considered to be charged negatively, $q_\mathrm{d} = -Z_\mathrm{d} e$. However, the plasma can also be influenced by the microparticles on scales greater than the local Debye length of the microparticles. For instance, if the dust density is high enough, the collection of electrons can lead to a noticeable depletion in electron density. The strength of depletion is described by the *Havnes parameter* P_H [142], which denotes the ratio of the charges collected by the

microparticles to the number of the free electrons per unit volume

$$P_{\mathrm{H}} = \frac{Z_{\mathrm{d}} n_{\mathrm{d}}}{n_{\mathrm{e}}}. \tag{2.15}$$

If P_{H} is high ($P_{\mathrm{H}} > 1$), the depletion of the electrons leads in turn to a significant reduction of the charge on the microparticles as compared to the charge of single grains [141]. For small P_{H} ($P_{\mathrm{H}} \ll 1$), the charge of the microparticles approaches that of an isolated grain embedded in the plasma, and no significant depletion of electrons takes place.

It has also been shown that the depletion of electrons leads to noticeable changes in the electron and ion distribution functions [143, 144]: If $P_{\mathrm{H}} > 0.1$, the faster electrons are depleted, even though the total electron density is unchanged [141].

In order to simplify the description, in the following the changes exerted by the microparticles on the plasma are ignored, and the forces experienced by the microparticles themselves are discussed.

2.2.1 Charging

A microparticle introduced into a plasma collects ions and electrons flowing to the grain surface and consequently charges up. Usually, the net charge of the microparticle becomes strongly negative under laboratory conditions, as the electron mobility by far exceeds that of the ions. The charge continues to build up, accelerating the ion influx towards the particle surface and retarding the electron fluxes until an equilibrium between the two fluxes (and therefore the final value of the microparticle charge) is reached. This process takes place in the time span of (10–100) µs [145]. The microparticle charge can fluctuate around the final value due to the random nature of the charging process. For typical conditions of complex plasmas in gas discharges, the magnitude of the charge fluctuations Z_1 is given by [138]

$$\langle Z_1 \rangle \sim 0.5\sqrt{Z_{\mathrm{d}}}, \tag{2.16}$$

where Z_{d} is the equilibrium charge. For small particles ($r_{\mathrm{d}} \leq 1\,\mu\mathrm{m}$) in the crystal phase at low pressures (of the order of 1 Pa), these fluctuations can cause spatial oscillations of the microparticles [146, 147]. For complex plasmas in the gaseous phase, the parameters are averaged in space, and charge fluctuations can be neglected [146].

Other processes of charging can also occur, but are usually less important in laboratory complex plasmas than the charging by ion and electron fluxes [2]. See Appendix A for details on other charging mechanisms.

The final potential that is reached is called the *floating potential* ϕ_{fl} (which is defined as the potential of any isolated body in a plasma (to which no net currents are flowing) relative to the plasma potential).

The charge q_{d} of the microparticles can then be determined by

$$q_{\mathrm{d}} = C\phi_{\mathrm{fl}}, \tag{2.17}$$

where C is the capacitance of the grain. For an isolated, conducting spherical grain, it is given by $C = 4\pi\epsilon_0 r_{\mathrm{d}}(1 + r_{\mathrm{d}}/\lambda_{\mathrm{D}}) \approx 4\pi\epsilon_0 r_{\mathrm{d}}$ ($r_{\mathrm{d}} \ll \lambda_{\mathrm{D}}$ is the radius of the microparticle).

The floating potential is determined by

$$\phi_{\mathrm{fl}} = -\zeta \frac{k_{\mathrm{B}} T_{\mathrm{e}}}{e}, \tag{2.18}$$

where ζ is a coefficient depending on the plasma parameters.

Orbital Motion Limited Theory

In the Orbital Motion Limited (OML) theory [148–152], it is assumed that the electrons and ions do not collide during their approach towards the grain, and that there are no barriers in the effective potential [11]. The cross sections for ion and electron collection are then determined from the laws of conservation of energy and angular momentum, e.g., for the ions

$$L = m_{\mathrm{i}} v_{\mathrm{i}0} b_{\mathrm{c}} = m_{\mathrm{i}} v_{\mathrm{i}} r_{\mathrm{d}}, \tag{2.19}$$

$$\frac{1}{2} m_{\mathrm{i}} v_{\mathrm{i}0}^2 = \frac{1}{2} m_{\mathrm{i}} v_{\mathrm{i}}^2 + e\phi_{\mathrm{fl}} \tag{2.20}$$

Here, $v_{\mathrm{i}0}$ is the ion velocity very far from the grain, b_{c} denotes the critical impact parameter where the ion just grazes the grain surface (ions with impact parameters $b < b_{\mathrm{c}}$ all hit the grain), and v_{i} represents the ion velocity when the ion is arriving at the grain.

From these equations, the cross section for ion collection is found to be

$$\sigma_{\mathrm{ci}} = \pi b_{\mathrm{c}}^2 = \pi r_{\mathrm{d}}^2 \left(1 - \frac{2e\phi_{\mathrm{fl}}}{m_{\mathrm{i}} v_{\mathrm{i}0}^2} \right). \tag{2.21}$$

The electron collection cross section is determined equivalently as

$$\sigma_{\mathrm{ce}} = \pi b_{\mathrm{c}}^2 = \pi r_{\mathrm{d}}^2 \left(1 + \frac{2e\phi_{\mathrm{fl}}}{m_{\mathrm{e}} v_{\mathrm{e}0}^2} \right). \tag{2.22}$$

The charging currents $I_{\mathrm{e(i)}}$ are then found by integrating over the Maxwell-Boltzmann distribution function $f_{\mathrm{e(i)}}(v)$

$$I_{\mathrm{e(i)}} = n_{\mathrm{e(i)}} \int v \sigma_{\mathrm{c\,e(i)}} f_{\mathrm{e(i)}}(v)\, d^3 v. \tag{2.23}$$

The integration yields

$$I_{\mathrm{i}} = \pi r_{\mathrm{d}}^2 n_{\mathrm{i}} e \sqrt{\frac{8 k_{\mathrm{B}} T_{\mathrm{i}}}{\pi m_{\mathrm{i}}}} \left(1 - \frac{e\phi_{\mathrm{fl}}}{k_{\mathrm{B}} T_{\mathrm{i}}} \right), \tag{2.24}$$

$$I_{\mathrm{e}} = -\pi r_{\mathrm{d}}^2 n_{\mathrm{e}} e \sqrt{\frac{8 k_{\mathrm{B}} T_{\mathrm{e}}}{\pi m_{\mathrm{e}}}} \exp\left(\frac{e\phi_{\mathrm{fl}}}{k_{\mathrm{B}} T_{\mathrm{e}}} \right). \tag{2.25}$$

Matsoukas and Russel [153] have considered the case for which the velocity of the ions is small compared with the ion thermal velocity (e.g., in the bulk of the discharge). The grain charge then is approximately

$$q_{\mathrm{d}} \approx C_0 4\pi\epsilon_0 \frac{k_{\mathrm{B}} T_{\mathrm{e}}}{e}\, r_{\mathrm{d}} \ln \left[\frac{n_{\mathrm{i}}}{n_{\mathrm{e}}} \left(\frac{m_{\mathrm{e}} T_{\mathrm{e}}}{m_{\mathrm{i}} T_{\mathrm{i}}} \right)^{1/2} \right], \tag{2.26}$$

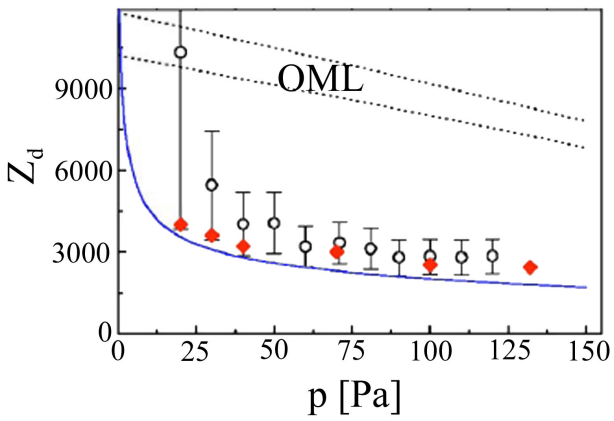

Figure 2.2: *Particle charge as a function of neutral gas pressure, for grains of radius $r_d = 1.3\,\mu m$. The charge was obtained from experiments (open circles) and from MD simulations for individual particles (solid diamonds). The area between the two dotted lines denotes the charge given by the OML model (which was modified to take into account the experimentally determined Havnes parameters in the range $0.4 < P_H < 1$. The solid lines show calculations including the increased ion flux to the particle in a weakly collisional regime. From [154].*

where C_0 depends weakly on T_e/T_i and m_e/m_i. Matsoukas and Russel found $C_0 = 0.73$ for a wide range of temperatures in an Argon plasma.

Even though the OML theory is one of the most widely applied theories to determine the particle charge, its region of validity is still under discussion. The "classical" criterion for validity of the approximations used is

$$r_d \ll \lambda_D \ll \lambda_c, \tag{2.27}$$

where λ_c is the mean free path of the ions. This condition is tightened to

$$\lambda_c > r_d \left(-\frac{e\phi_{fl}}{k_B T_i} \right)^{1/2} \tag{2.28}$$

by Annaratone, Allen, and Allen [155]. Khrapak et al. [154] determine

$$\lambda_c > 0.1 \left(-\frac{e\phi_{fl}}{k_B T_i} \right) \lambda_D \tag{2.29}$$

as criterion for the validity of the OML approximation. Figure 2.2 shows the number of charges they find experimentally and with molecular dynamics (MD) simulations as a function of neutral gas pressure in comparison with the prediction by OML theory. The discrepancy between the theory and the experiments rises with rising pressure (and therefore rising ion collisionality).

Typical experiments in complex plasmas are performed at pressures between 10 and 100 Pa. Therefore, OML is often useful only to determine an upper estimate of the grain charge, and a theory taking into account ion-neutral collisions is required for refinements.

Ion collisionality

Ions that collide with neutrals while in the vicinity of a grain can lose so much energy that they cannot escape from the potential well created by the microparticle. If the ions

fall onto the grain, the amount of microparticle charge is reduced. Ions that orbit the grain can also occur, not able to escape but also not falling onto the grain surface. These *trapped ions* remain in orbit around the microparticle until another collision takes place. They modify the potential created by the microparticle, and the combined effect of ion collisionality and trapped ions can reduce the strength of the negative floating potential ϕ_{fl} of the microparticles by as much as 50 %, depending on the plasma parameters [156].

Another theory taking into account ion collisions is the Drift Motion Limited (DML) theory [157]. Here, the increase of the ion flux to the grain surface is described by introducing on additional parameter ξ in the description of the flux:

$$I_{\mathrm{i}} = \pi r_{\mathrm{d}}^2 n_{\mathrm{i}} e \sqrt{\frac{8 k_{\mathrm{B}} T_{\mathrm{i}}}{\pi m_{\mathrm{i}}}} \left(1 - \xi \frac{e\phi_{\mathrm{fl}}}{k_{\mathrm{B}} T_{\mathrm{i}}}\right). \tag{2.30}$$

It is a function of the ion mean free path λ_{c} and the particle radius r_{d}. If $\lambda_{\mathrm{c}} < \lambda_{\mathrm{D}}/3$, ξ is given by

$$\xi = \sqrt{2\pi/3}\, \lambda_{\mathrm{c}}/r_{\mathrm{d}}. \tag{2.31}$$

Morfill et al. [157] show that for $\lambda_{\mathrm{c}} > 0.1\lambda_{\mathrm{D}}$, a fit works well in which the particle radius in Equation (2.31) is replaced by

$$r_{\mathrm{d}} \rightarrow r_{\mathrm{d}} + \sqrt{2\pi/3} \frac{\lambda_{\mathrm{c}}^2}{3\lambda_{\mathrm{D}} + \lambda_{\mathrm{c}}}. \tag{2.32}$$

The OML estimate of the particle charge can be as high as twice that obtained using DML theory [157].

At higher ion collisionalities, the ion motion towards the grain is impeded by the collisions, not enhanced as in the case of weak ion collisionality. Then, the grain charge increases with increasing pressure, until a saturation at high pressures (when the electron collisionality becomes significant) is reached [158]. Khrapak and Morfill [158] show that the minimum in the strength of microparticle charging is reached when the ion mean free path is of the order of the screening length. In some cases, under these conditions, the value predicted by radial motion theory can be attained.

Radial Motion Theory

The lowest charge estimate is predicted by the Radial Motion Theory (also called Allen, Boyd, Reynolds (ABR) theory) [159, 160]. In this theory, it is assumed that the ions move radially towards the grain. Collisions with neutrals are again neglected. The ion energy is determined by the potential difference between the initial ion position and the grain surface.

For the electron densities, a Boltzmann relation is assumed

$$n_{\mathrm{e}}(r) = n_{\mathrm{e0}} \exp\left(\frac{e\phi_{\mathrm{E}}(r)}{k_{\mathrm{B}} T_{\mathrm{e}}}\right), \tag{2.33}$$

where as above $e\phi_{\mathrm{E}} < 0$. The electron flux is obtained by integrating the radial velocity of the electrons over the velocity space, considering only inbound electrons, and the obtained value is then set equal to the ion flux [161]. The grain charge is determined by solving Poisson's equation (2.2).

2.2.2 Forces on isolated grains

The charged grains in the plasma are subjected to various forces, which are briefly introduced in the following.

Gravity

In ground based experiments, one of the strongest forces acting on the microparticles is the force of gravity $\mathbf{F}_\mathrm{g}$

$$\mathbf{F}_\mathrm{g} = m_\mathrm{d}\,\mathbf{g}, \tag{2.34}$$

where $\mathbf{g}$ is the gravitational acceleration. The force of gravity scales with the volume of the microparticle, and thus $F_\mathrm{g} \propto r_\mathrm{d}^3$. For a microparticle made of melamine-formaldehyde often used in complex plasma experiments (density $\rho = 1510\,\mathrm{kg/m^3}$, radius $r_\mathrm{d} = 3.4\,\mu\mathrm{m}$), the strength of the force of gravity is $F_\mathrm{g} = 2.49 \cdot 10^{-13}\,\mathrm{N}$.

Electric force

The electric force acting on the grains is [162]

$$\boldsymbol{F}_\mathrm{E} = q_\mathrm{d}\boldsymbol{E}\left(1 + \frac{k_\mathrm{D}^2 r_\mathrm{d}^2}{3(1 + k_\mathrm{D} r_\mathrm{d})}\right), \tag{2.35}$$

with $\mathbf{E}$ denoting the electric field and $k_\mathrm{D} = 1/\lambda_\mathrm{D}$. This implies that the plasma does not shield the microparticle from bulk electric fields, in fact, the bulk polarization even slightly increases the effective electric field acting on the grain [162]. In most complex plasmas, $r_\mathrm{d} \ll \lambda_\mathrm{D}$, and the charges on the microparticles are not polarized, reducing Equation (2.35) to

$$\boldsymbol{F}_\mathrm{E} = q_\mathrm{d}\boldsymbol{E}. \tag{2.36}$$

The charge of the microparticles is proportional to their radius, and therefore $F_\mathrm{E} \propto r_\mathrm{d}$.

Electric fields are often used to levitate particles against gravity. For instance, they are self-maintained in the sheaths of RF discharges [10], in striations of DC discharges [138, 163], or within a firerod of a Q-machine [87]. Usually these electric fields are strongly inhomogeneous, which results in highly compressed complex plasma clouds.

In the case of RF discharges like those used in the experimental part of this work, the strength E of the electric field at the edge of the sheath region is of the order of a few hundred V/m. Inside the bulk of the discharge, the electric fields are much weaker, as they are screened by the plasma.

Konopka [164] measured the horizontal confinement potential, which was enhanced by a copper ring placed on the lower electrode. The distribution of this potential is fitted well by

$$\phi_E(x) - \phi_p = -b(x - x_0)^2, \tag{2.37}$$

where ϕ_E is the electric potential acting on a test particle, ϕ_p denotes the plasma potential, x is the horizontal position of the test particle and x_0 designates the horizontal position of the maximum of the potential. The parabola constant b was determined to be of the order of $10^{-11}\,\mathrm{kg/s^2}$ by studying horizontal oscillations of a test particle in the confinement potential [164].

Magnetic force

The magnetic force (Lorentz force) $\mathbf{F}_\mathrm{L}$ acting on a point charge q_d with velocity $\mathbf{v}_\mathrm{d}$ is given by

$$\mathbf{F}_\mathrm{L} = q_\mathrm{d}\mathbf{v}_\mathrm{d} \times \mathbf{B}. \tag{2.38}$$

Here, $\mathbf{B}$ represents the magnetic flux density. The influence of the magnetic field is only important if one of the particle species in the plasma is *magnetized*: its collision frequency ν_sn with the neutral background gas is much smaller than its gyrofrequency ω_gs, and it can thus complete many gyrorotations before being disturbed by a collision with a neutral particle: $\nu_\mathrm{sn} \ll \omega_\mathrm{gs}$. Due to their small mass, the plasma electrons are easier to magnetize than ions or microparticles. The force induced by the magnetic field of the Earth can be neglected if the gas pressure is not unusually small ($p > 5\,\mathrm{Pa}$) [165].

Neutral drag

The neutral drag force (*Epstein drag force*) arises when the microparticles are moving relative to the neutral background gas, so that the momentum transferred to the grains by atoms from the forward side exceeds that transferred by atoms from the backward side. The neutral drag force is directed oppositely to the direction of motion of the microparticles. Epstein [166] determined the drag force for particles which are small in size compared with the mean free path of atom-atom collisions ($r_\mathrm{d} \ll \lambda_\mathrm{mfp}$) and which move slowly compared with the mean thermal velocity of the gas atoms ($v_\mathrm{d} \ll u_\mathrm{n}$) as

$$\boldsymbol{F}_\mathrm{dn} = -\gamma_\mathrm{Ep} m_\mathrm{d} \boldsymbol{v}_\mathrm{d}, \tag{2.39}$$

where γ_Ep is the damping rate coefficient

$$\gamma_\mathrm{Ep} = \delta_\mathrm{Ep} \frac{4\pi}{3} \frac{n_\mathrm{n} m_\mathrm{n} u_\mathrm{n}}{m_\mathrm{d}} r_\mathrm{d}^2 \tag{2.40}$$

with $u_\mathrm{n} = \sqrt{8 k_\mathrm{B} T_\mathrm{n} / \pi m_\mathrm{n}}$, n_n representing the number density of the gas atoms, and r_d designating the radius of the microparticles. The mass of the gas atoms and microparticles are denoted by m_n and m_d, respectively. The coefficient δ_Ep depends on the collision mechanism, with values between 1.0 for specular reflection and 1.442 for diffuse reflection [166]. Liu, Goree, and Nosenko [167] measured $\delta_{Ep} = 1.26 \pm 0.13$ with a laser acceleration method and $\delta_\mathrm{Ep} = 1.44 \pm 0.19$ using the vertical resonance method. Konopka [164] determined $\delta_\mathrm{Ep} = 1.48 \pm 0.05$ for melamine-formaldehyde (MF) particles in a room-temperature Argon plasma, which will be used in the calculations in the following. All measured values are in fairly good agreement with Epstein's formula. The drag force therefore scales as the surface of the particles: $F_\mathrm{dn} \propto r_\mathrm{d}^2$.

Ion drag

The ion drag force exerted on the microparticles stems from three sources [2]: the *collection drag force* $\mathbf{F}_\mathrm{di}^\mathrm{coll}$, which is due to direct impacts of ions on the grain surface, the *orbit* or *Coulomb drag force* $\mathbf{F}_\mathrm{di}^\mathrm{o}$, induced by Coulomb interactions between ions and microparticles, and the *ion flow drag force* $\mathbf{F}_\mathrm{di}^\mathrm{flow}$, caused by a distortion of the shape of the Debye sphere around the microparticle:

$$\mathbf{F}_\mathrm{di} = \mathbf{F}_\mathrm{di}^\mathrm{coll} + \mathbf{F}_\mathrm{di}^\mathrm{o} + \mathbf{F}_\mathrm{di}^\mathrm{flow}. \tag{2.41}$$

The contribution of the ion flow is usually small [168] and can be neglected.

The collection force is caused by the nonelastic momentum transfer by the ions accumulating on the grain. The force is given by [169]

$$\boldsymbol{F}_{\mathrm{di}}^{\mathrm{coll}} = n_{\mathrm{i}} \bar{v}_{\mathrm{i}} m_{\mathrm{i}} \pi b_{\mathrm{c}}^2 \boldsymbol{v}_{\mathrm{i}} \tag{2.42}$$

with the collection impact parameter

$$b_{\mathrm{c}} = r_{\mathrm{d}} \left(1 - \frac{2e\phi_{\mathrm{fl}}}{m_{\mathrm{i}} \bar{v}_{\mathrm{i}}^2} \right)^{1/2}. \tag{2.43}$$

The mean velocity of the ions $\bar{v}_{\mathrm{i}}$ is given by $\bar{v}_{\mathrm{i}} = \sqrt{v_{\mathrm{i}}^2 + u_{\mathrm{i}}^2}$. The mass of the ions is designated by m_{i}. The expression of the collection impact parameter is based on the OML theory.

The orbit force is caused by momentum transfer due to elastic Coulomb interactions between the ions and the microparticles. It can be expressed as [169]

$$\boldsymbol{F}_{\mathrm{di}}^{\mathrm{o}} = n_i \overline{v_i} m_i 4\pi b_{\pi/2}^2 \Gamma_C \boldsymbol{v_i}, \tag{2.44}$$

where

$$b_{\pi/2} = r_{\mathrm{d}} \frac{e|\phi_{\mathrm{fl}}|}{m_{\mathrm{i}} \overline{v_i}^2} \tag{2.45}$$

represents the impact parameter which results in a deflection of the particle by $\pi/2$, and

$$\Gamma_C = \frac{1}{2} \ln \left(\frac{\lambda_D^2 + b_{\pi/2}^2}{b_c^2 + b_{\pi/2}^2} \right) \tag{2.46}$$

denotes the Coulomb logarithm. It contains contributions from the region between b_c and λ_D [2].

The total ion drag force can then be expressed as

$$\boldsymbol{F_{di}} = m_i n_i \overline{v_i} \pi \left(b_c^2 + 4 b_{\pi/2}^2 \Gamma_C \right) \boldsymbol{v_i}. \tag{2.47}$$

This equation is known as *Barnes' formula* [169].

Khrapak et al. [170] show that Equation (2.47) underestimates the strength of the ion drag force: In complex plasmas, the range of the interaction between ions and microparticles is often larger than the Debye length, as the grains are highly charged, and a non-negligible amount of ions is deflected strongly even outside the Debye sphere. This means that the magnitude of the Coulomb logarithm is often too small. For instance, using only Barnes' formula (2.47), the formation of the central particle free region (void) of complex plasmas under microgravity conditions cannot be explained by ion drag force alone, but with the modified force this is possible [57].

Khrapak et al. [170, 171] modify the standard theory by including small angle ion-grain collisions with a cut-off larger than the Debye length. They replace the standard Coulomb logarithm Γ_C in (2.47) with

$$\Gamma_C^* = 2 \int_0^\infty e^{-x} \ln \left(\frac{2\lambda_D x + b_{\pi/2}}{2 r_{\mathrm{d}} x + b_{\pi/2}} \right) dx. \tag{2.48}$$

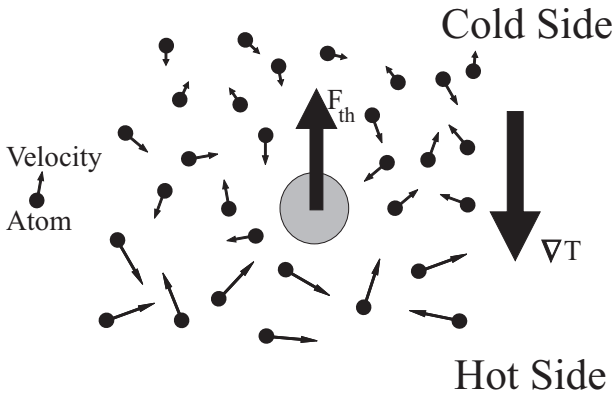

Figure 2.3: *Simplified picture of a grain in a gas with a temperature gradient, after [178]. The atoms on the hot side carry more momentum than those on the cold side, which yields a difference in momentum transferred by collisions from the atoms to the grain. Therefore, a force is acting on the grain, pointed towards the cold side.*

The result is a strong increase of the orbit force by a factor of up to 40, especially in the case of subthermal ions. Neglecting ion collisions with the neutral background, the ion drag force is then given by *Khrapak's formula* [170]

$$\boldsymbol{F}_{\mathrm{id}} = \frac{2\sqrt{2\pi}}{3} n_{\mathrm{i}} m_{\mathrm{i}} u_{\mathrm{i}} b_{\pi/2}^2 \Gamma_c^* \, \boldsymbol{v}_{\mathrm{i}}. \tag{2.49}$$

Here, only the orbital contribution to the force is considered, as it is shown in [170] that the elastic scattering strongly dominates over inelastic scattering for grains of radii (0.01–10) µm. Equation 2.49 has been proven to agree better with experimental data, especially under low pressure conditions [172], and has later been extended to the strong interaction limit, also giving good experimental results [173, 174].

Recently, a kinetic approach has been used to calculate the ion drag force [175].

Electron drag

The electron drag force acting on microparticles can usually be neglected because of the low electron mass. Exceptions are discharges with strong electron drifts (e.g., DC discharges) and low electron temperatures ($T_{\mathrm{e}} \lesssim 1\,\mathrm{eV}$) [176].

Thermophoretic force

If a temperature gradient is maintained in the gas, the atoms on the hot side of an inserted grain carry more momentum than those on the cold side. This yields a difference in momentum transferred by collisions from the atoms to the grain, and therefore a net force is acting on the microparticle in the direction opposite to that of the temperature gradient [177]. Figure 2.3 demonstrates this simplified process.

The description of the thermophoretic force depends strongly on the Knudsen number $\mathcal{K}$ [178], which is the ratio of the atom mean free path to a characteristic length scale, in the case discussed here the particle radius

$$\mathcal{K} = \lambda_{\mathrm{mfp}} / r_{\mathrm{d}}. \tag{2.50}$$

Under typical conditions for experiments with complex plasmas under the action of thermophoresis in Argon, the Knudsen number is of the order of 110 (see Table 2.1 for the conditions used). For smaller particles or Neon gas, it is even larger. This puts the experiments in the *free molecular regime* ($\mathcal{K} \to \infty$), where the particle can be treated as

gas	σ [$10^{-20}\,\mathrm{m}^2$]	λ_{mfp} [µm]	$\mathcal{K}$	F_{th} [$10^{-12}\,\mathrm{N}$]
Ar	42	380	110	2.5
Ne	21	770	230	5.1

Table 2.1: *Cross section σ [179] and mean free path $\lambda_{\mathrm{mfp}} = (1/\sqrt{2}\sigma n_{\mathrm{n}})$ for atom-atom collisions under conditions $T_{\mathrm{n}} = 330\,K$ and $p = 20\,Pa$, and Knudsen number $\mathcal{K}$ and strength F_{th} of the thermophoretic force (2.52) acting on particles with $r_{\mathrm{d}} = 3.4\,\mu m$ at $dT/dx = 2000\,K/m$.*

a very large molecule, and the velocity distribution of the gas particles is not disturbed by the presence of the microparticle [178]. Waldmann [180] derives the thermophoretic force in the free molecular regime for monatomic gases, the *Waldmann formula*, which for parallel-plate geometry and complete thermal accomodation at the particle surface reads as [181]

$$\mathbf{F}_{\mathrm{th}} = -\left(\frac{32}{15}\right)\left(\frac{\pi m_{\mathrm{n}}}{8k_{\mathrm{B}}T_{\mathrm{n}}}\right)^{1/2} r_{\mathrm{d}}^2\left(\kappa^{\mathrm{tr}}\frac{dT}{dx}\right), \tag{2.51}$$

where κ^{tr} is the translational part of the thermal conductivity of the gas[1], dT/dx denotes the temperature gradient maintained in the gas, T_{n} is the gas temperature, m_{n} represents the mass of the gas atoms, and r_{d} is the radius of the microparticle. The grain surface that is exposed to the impinging gas atoms determines the scaling of the force: $F_{\mathrm{th}} \propto r_{\mathrm{d}}^2$.

The thermophoretic force acting in complex plasmas has also been investigated experimentally. Rothermel et al. [51] find that

$$F_{\mathrm{th}} = -3.33\frac{k_{\mathrm{B}}r_{\mathrm{d}}^2}{\sigma}\frac{dT}{dx} \tag{2.52}$$

agrees well with the experimental data. Equation (2.52) results in a 25 % stronger force than predicted by (2.51). As the authors investigated complex plasmas under conditions very similar to those in this work, the estimations in this thesis are based on Equation (2.52).

Thermophoresis has been employed by numerous experimenters to counteract gravity in complex plasmas [51, 130, 157, 182–186]. Adjusting the temperature gradient allows the form and position of the microparticle cloud to be controlled, but commonly the cloud has a complicated "sandwich-like" structure under the action of thermophoresis [51, 183]. The difference between the scalings with particle radius of the thermophoretic force ($F_{\mathrm{th}} \propto r_{\mathrm{d}}^2$) and the force of gravity ($F_{\mathrm{g}} \propto r_{\mathrm{d}}^3$) causes a sorting of the grains by size. The microparticle clouds created by this method therefore cannot replace the homogeneous structures achieved under microgravity conditions [48].

If the gas is enclosed in a small container, another Knudsen number becomes important [178]

$$\mathcal{K}_{\mathrm{L}} = \lambda_{\mathrm{mfp}}/L, \tag{2.53}$$

[1] For monatomic gases, the translational thermal conductivity is equal to the total thermal conductivity $\kappa^{\mathrm{tr}} = \kappa$.

where L is the distance from the microparticle to the nearest plate[2]. In typical experiments relevant to this work, $\mathcal{K}_\mathrm{L}$ is of the order of 0.03.

In rarefied gases with temperature gradients perpendicular to a wall a jump of the temperature between the inserted plates and the gas occurs [187]. The temperature difference between the wall and the gas is described by the relationship [188]

$$T_\mathrm{w} - T_\mathrm{n} = C_\mathrm{T} \frac{dT}{dx}, \tag{2.54}$$

where T_w and T_n denote the temperatures of the wall and the gas, respectively, and C_T is the temperature jump length [189]:

$$C_\mathrm{T} = C \frac{2 - \sigma_\mathrm{T}}{\sigma_\mathrm{T}} \lambda_\mathrm{mfp}. \tag{2.55}$$

Here, σ_T is the accommodation coefficient. The magnitude of the constant C depends on the type of gas. For monatomic gases, Pan et al. [189] find $C = 1.7964$ when the heat flows from the gas to the wall and $C = 1.5954$ in the opposite case. The magnitude of the temperature jump therefore is inversely proportional to gas pressure.

In gases that are in the near-continuum slip flow regime with $\mathcal{K}_\mathrm{L}$ not too large, the thermophoretic force can be approximated by the continuum-gas limit if the temperature gradient is adjusted to take into account the temperature jumps that occur at each plate [190].

Thermal creep

A strong temperature gradient along a surface in a rarefied gas creates *thermal creep* or *thermal gas slip*. This effect induces a neutral gas flow tangential to the surface *in the direction of the temperature gradient* and proportional to the magnitude of the temperature gradient [191]. The underlying physical mechanism is the following [192]: If a plane is immersed in a gas with a temperature gradient along its surface, atoms that collide with the plane transfer momentum to the wall depending on their direction (compare Figure 2.4a): The velocity of the atoms arriving from the warmer side is greater than that of the particles from the cold side. In case of diffuse reflection, there is no contribution of the atoms leaving the wall to the tangential momentum transfer (Figure 2.4b). This leads to a net transfer of momentum from the gas to the wall towards the cold side, which, in turn, induces a gas flux along the wall towards the hotter side. This effect was predicted by Maxwell [49] and first verified experimentally by Reynolds [193]. The slip velocity of the gas along the wall is given by

$$v_\mathrm{TC} = K_\mathrm{TC}\, \nu \ln\left(\nabla_{||} T_\mathrm{w}\right), \tag{2.56}$$

where K_TC is the coefficient of thermal creep [49], which is in the range of 0.75–1.2 [194]. The kinematic viscosity is denoted by ν, and $\nabla_{||} T_\mathrm{w}$ is the component of the temperature gradient parallel to the surface. Mitic et al. [185] observed movement of microparticles in a complex plasma under the influence of neutral gas convection induced by thermal creep in a DC discharge tube heated non-uniformly by an external heating wire.

[2] Often, for simplicity, the distance between the plates is used [182].

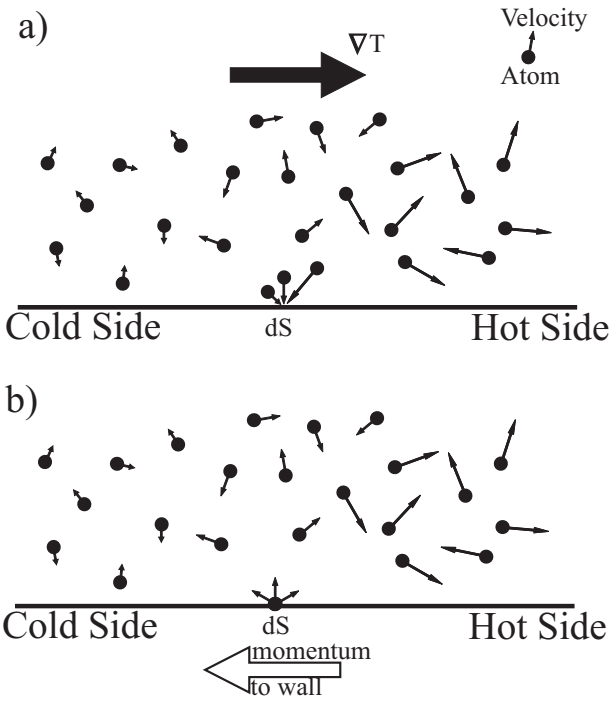

Figure 2.4: *Physical mechanism behind the thermal creep process in a gas with a thermal gradient along a wall: (a) The particles impact the wall at a small area dS with different velocities, but (b) are reflected isotropically. This leads to a momentum transfer to the wall towards the cold side and a corresponding flux of the gas towards the hot side.*

2.2.3 Interparticle forces

When several grains are inserted into the plasma, they interact with each other. They are charged strongly and equally in sign and thus repel each other. The situation, however, can be more complicated: it has been shown theoretically that at larger distances, there can be an attractive force between the particles [11]. Additionally, the presence of other microparticles reduces the charge on each particle as was shown above (Section 2.2, p. 23).

Below, the most important interparticle forces are briefly discussed.

Electrostatic Repulsion

The potential surrounding a spherical microparticle with charge q_d in a plasma is the *Debye-Hückel potential*, which is also called *Yukawa potential*

$$U(r) = \frac{q_\mathrm{d}^*}{4\pi\epsilon_0 r} e^{-r/\lambda_\mathrm{d}}, \tag{2.57}$$

with the effective charge on the microparticle q_d^* given by

$$q_\mathrm{d}^* = \frac{q_\mathrm{d}}{1 + r_\mathrm{d}/\lambda_\mathrm{D}} e^{r_\mathrm{d}/\lambda_\mathrm{D}}. \tag{2.58}$$

For small particles ($r_\mathrm{d} \ll \lambda_\mathrm{D}$), Expression (2.58) reduces to the real charge q_d. In all systems studied in this thesis, this condition is fulfilled.

The interaction force between two microparticles at distance Δ is consequently given by

$$\boldsymbol{F}_\mathrm{dd} = -q_\mathrm{d} \frac{\partial U}{\partial r} \frac{\boldsymbol{r}}{r}\bigg|_{r=\Delta}. \tag{2.59}$$

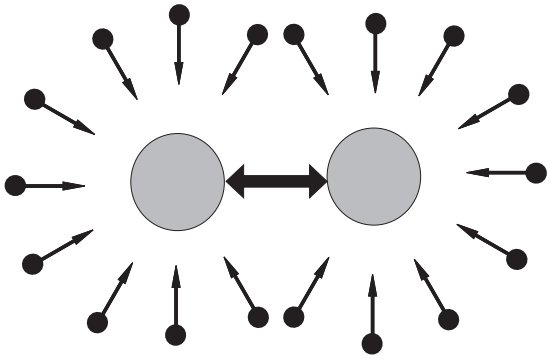

Figure 2.5: *The mechanism behind the shadow force. Two adjacent grains shield each other from the particle influx, leading to an attracting net force between the grains.*

Shadow forces

Each grain in the plasma is constantly bombarded by plasma ions and atoms from all sides. If two grains are close to each other, the plasma flux onto one grain is shadowed by the other one, leading to a difference in pressure exerted by the plasma particles between the outer and the inner sides, and, consequently, to a net force between the two grains [138, 195]. Figure 2.5 shows this mechanism.

Due to their negative charge, the microparticles attract the ions surrounding them, leading to a constant influx of ions to the surface, and, in case of neighboring microparticles, a resulting *ion shadow force*. If the temperature of the grain surface is different from the gas temperature, net fluxes of energy and momentum between the microparticles and the gas exist [138], leading to the *neutral shadow force*. This force is repulsive if the grain surface temperature is higher than the neutral gas temperature and attractive in the opposite case [196]. The potentials of both ion and neutral shadow forces scale as [138]

$$U_{ns}(r) \sim U_{is}(r) \propto 1/r. \tag{2.60}$$

At large distances, the attraction caused by the shadow effect thus can theoretically overcome the electrostatic repulsion.

Ion wake potential

When several layers of particles are present above each other in or near the sheath, the particles often arrange themselves in vertical chains. This effect is caused by the ions that are streaming towards the electrodes. They are deflected by the charged microparticles and create a wake—a region of positive space charge—downstream of the particle. The positive space charge then in turn attracts the microparticles in lower layers [197]. Upstream and to the side, the Debye sphere is almost not deformed [198]. Melzer, Schweigert, and Piel [199] demonstrated experimentally that this force acts only on the "lower" particle and not on the "upper" one by selectively pushing either one with a laser beam. When the upper particle is moved, the lower particle follows as predicted, whereas, when the lower particle is moved, the upper one remains stationary. This demonstrates the nonreciprocal nature of the wake field attraction in the sheath [200]. It is possible to produce a reciprocal ion wake

force	scaling	strength $[10^{-13}\,\mathrm{N}]$	
		small particles	big particles
gravity (2.34)	r_d^3	0.16	24
electric force (2.36)	r_d	0.50	2.7
neutral drag (2.39)	r_d^2	0.032	0.92
thermophoresis (2.52)	r_d^2	0.75	21
ion drag (Barnes) (2.47)		0.049	0.037
ion drag (Khrapak) (2.49)		0.14	1.9

Table 2.2: *Overview of the most important forces acting on "small" and "big" microparticles (radii $r_\mathrm{d} = 0.64\,\mu m$ and $r_\mathrm{d} = 3.4\,\mu m$, respectively) with mass density $\rho = 1510\,kg/m^3$. The charge is calculated with the OML approximation (2.26), thus giving an upper limit for the strength of the electric force. Further assumptions are: Argon plasma with $\sigma = 42 \cdot 10^{-20}\,m^2$ [179] and $m_\mathrm{n} = 40 \cdot 1.67 \cdot 10^{-27}\,kg$, $T_\mathrm{e} = 3\,eV$, $T_\mathrm{i} = T_\mathrm{n} = 300\,K$, $n_\mathrm{i} = n_\mathrm{e} = 10^{-7} \cdot n_\mathrm{n}$, $E = 100\,V/m$, $\nabla T = 1670\,K/m$, $p = 20\,Pa$, $\delta_\mathrm{Ep} = 1.48$ [164], $v_\mathrm{i} = 0.01 u_\mathrm{B} = 0.01\sqrt{k_\mathrm{B} T_\mathrm{e}/m_\mathrm{i}}$.*

potential by applying alternating electric fields at frequencies that the ions can follow, but the microparticles cannot [201]—this creates so-called *electrorheological plasmas*.

Force scalings and magnitudes

Table 2.2 lists the scaling of the forces with the grain radius (if a simple scaling is possible; for the ion drag the dependence is complex), and the typical strengths for the cases $r_\mathrm{d} = 0.64\,\mu\mathrm{m}$ and $r_\mathrm{d} = 3.4\,\mu\mathrm{m}$. It can be seen that the magnitude of the electric force is of the order of that of gravity. Also, for the chosen set of parameters, the thermophoretic force can be strong enough to compensate for gravity, likewise making possible a levitation of the microparticles.

2.2.4 Dust-acoustic waves

Vast clouds of microparticles embedded in the plasma environment reveal a new remarkable behavior—the ability to support new low frequency wave modes. The simplest waves are the *dust acoustic waves* (compare Section 1.6). Following [2], the dispersion relation of these waves can be derived assuming Boltzmann distributions of the electron and ion number densities perturbations:

$$n_\mathrm{e1} \approx n_\mathrm{e0} \frac{e\phi_\mathrm{E}}{k_\mathrm{B} T_\mathrm{e}},\; n_\mathrm{i1} \approx -n_\mathrm{i0} \frac{e\phi_\mathrm{E}}{k_\mathrm{B} T_\mathrm{i}}, \tag{2.61}$$

where $n_\mathrm{i,e}$ are the ion, electron number densities, ϕ_E is the electric potential, and $T_\mathrm{i,e}$ depict the ion, electron temperatures. Assuming furthermore that the quasi-neutrality condition including the negatively charged grains, $e n_\mathrm{i0} = e n_\mathrm{e0} - q_\mathrm{d} n_\mathrm{d0}$, holds in the unperturbed state, and that there are no fluctuations of the microparticle charge, the Poisson equation can be combined with the microparticle fluid continuity and momentum equations to yield

$$\left(\frac{\partial^2}{\partial t^2} - \frac{\gamma_\mathrm{p} k_\mathrm{B} T_\mathrm{d}}{m_\mathrm{d}} \nabla^2\right) n_\mathrm{d1} = \frac{n_\mathrm{d0} q_\mathrm{d}}{m_\mathrm{d}} \nabla^2 \phi_\mathrm{E}. \tag{2.62}$$

Here, γ_p is the polytropic index ($\gamma_\mathrm{p} = 1$ for isothermal and $\gamma_\mathrm{p} = 3$ for adiabatic particle motion). Linearizing the equations while assuming small perturbations of the plasma parameters and potential $\propto \exp(-i\omega t + i\,\mathbf{k}\cdot\mathbf{x})$ (ω is the wave frequency and $\mathbf{k}$ the wave vector) results in the dispersion relation for the dust-acoustic waves

$$\omega^2 = \gamma_\mathrm{p} u_\mathrm{Td}^2 k^2 + \frac{c_\mathrm{DAW}^2 k^2}{1 + k^2 \lambda_\mathrm{D}^2}. \tag{2.63}$$

The thermal velocity of the microparticles is given by $u_\mathrm{Td} = \sqrt{k_\mathrm{B} T_\mathrm{d}/m_\mathrm{d}}$, and

$$c_\mathrm{DAW} = \omega_\mathrm{pd} \lambda_\mathrm{D} = \left(\frac{k_\mathrm{B} T_\mathrm{i} Z_\mathrm{d}^2 n_\mathrm{d}}{m_\mathrm{d} n_\mathrm{i}}\right)^{1/2} \tag{2.64}$$

is the dust acoustic speed. Above, interparticle collisions were neglected. In the simplest frictional case, taking into account the Epstein drag force, it is sufficient to substitute ω^2 in (2.63) by $\omega(\omega + i\gamma_\mathrm{Ep})$ [98].

If $\omega \gg k u_\mathrm{Td}$, Equation (2.64) can be simplified [75]:

$$\omega = \frac{c_\mathrm{DAW} k}{\sqrt{1 + k^2 \lambda_\mathrm{D}^2}}. \tag{2.65}$$

For long wavelengths ($\lambda_\mathrm{D}^2 k^2 \ll 1$), this equation reduces to $\omega \approx c_\mathrm{DAW} k$. For the opposite limit, ($\lambda_\mathrm{D}^2 k^2 \gg 1$), it corresponds to oscillations at the dust plasma frequency: $\omega \approx \omega_\mathrm{pd}$.

There are many other collective modes of vast microparticle clouds, noticeably the breathing mode and the slashing mode, which have been introduced in Section 1.6. In the following, some of these modes excited in fluid complex plasmas are studied using the PK-3 Plus setup.

Chapter 3

Experimental setup and analysis

The experiments analyzed in this thesis were performed in the PK-3 Plus laboratory, which was designed by the PK-3 Plus team [48]. They were partly carried out at the Max-Planck-Institut für extraterrestrische Physik (MPE) in Garching, Germany, and partly by the European astronaut Thomas Reiter as well as the Russian cosmonauts Sergey Volkov and Yury Lonchakov in the equivalent setup on board the International Space Station (ISS) within the framework of a cooperation between the MPE and the Joint Institute for High Temperatures (JIHT) in Moscow, Russia. The microgravity conditions on board the ISS are very favorable for experiments with complex plasmas, but the data acquisition system is limited by the weight and power consumption as well as the fact that the hardware is not up-to-date any more[1]; therefore some experiments were performed on the 13th parabolic flight campaign sponsored by the Deutsches Zentrum für Luft- und Raumfahrt (DLR) using the ground setup with a state-of-the-art data-acquisition system.

3.1 PK-3 Plus laboratory

The plasma chamber of the PK-3 Plus laboratory consists of a quadratic glass cuvette covered on the top and bottom by two aluminum ground plates (Figure 3.1). It can

[1]The laboratory was launched to the ISS in 2005.

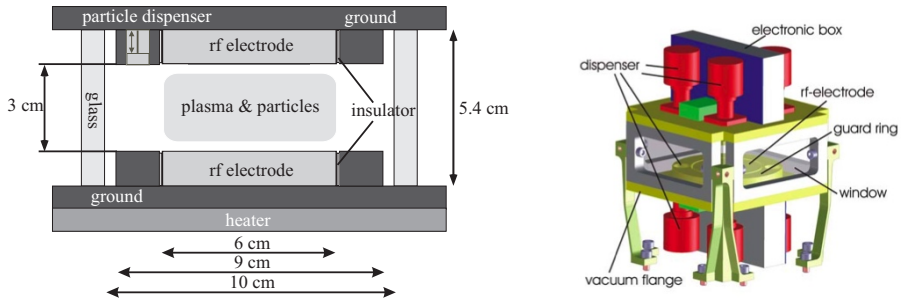

(a) *Schema of a vertical cross section through the experiment chamber.*

(b) *Spatial view of the experiment chamber.*

Figure 3.1: *Schematics of the PK-3 Plus chamber. The heater and dispenser configuration of a) corresponds to the ground setup, the distribution of the dispensers in b) to the space setup. From [48].*

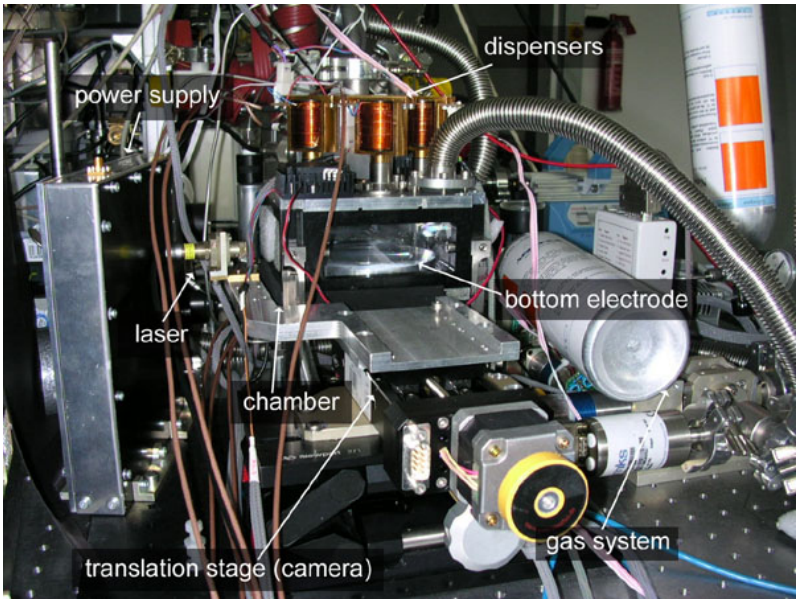

Figure 3.2: *Photograph of the ground experimental setup. The camera, which is normally placed on the translation stage, is missing.*

be evacuated to a minimal base pressure of 10^{-6} mbar and can be filled with gas from an attached gas bottle. The plasma is produced by an RF field applied to two parallel electrodes on the top and bottom of the chamber. Microparticles are then inserted into the plasma with dispensers and are illuminated with a laser beam, the scattered light of which is recorded with a camera. A photograph of the ground setup is shown in Figure 3.2.

Vacuum system

A schematic of the vacuum system of the PK-3 Plus laboratory is shown in Figure 3.3. A difference between the ground and the space setups is the way pre-vacuum is achieved: The roughing pump which is used on ground is replaced by a connection to the vacuum of space on board the ISS. In both laboratories, a turbo-molecular pump is employed to attain high vacuum conditions. The assist gas (shown in the right of the figure as Argon bottle, even though in space, an additional Neon bottle is present) is then released by a three-way cock via a rotating dead volume. Thereafter, the gas from this region fills an auxiliary volume and is allowed to expand through a capillary into the plasma chamber. By rotating the 3-way-valve the gas in the plasma chamber can be regularly refreshed.

The chamber is connected to the pumps via another three-way-cock that allows either a direct connection to the pump, completely disconnecting the chamber from the pump, or connecting the pressure control unit. This instrument controls a solenoid valve between the chamber and the pumps which can be opened to various extents to allow the pressure measured by the control unit to approach a software-controlled value. This way, pressures of (5–255) Pa can be adjusted to the desired level[2].

The pressure is measured independently by a pirani vacuum-meter, a baratron and a second baratron in the pressure control unit. The most accurate pressure measurement is

[2]The pressure in the chamber can be slightly different (some Pa) from that measured by the control unit because of the physical distance between the two.

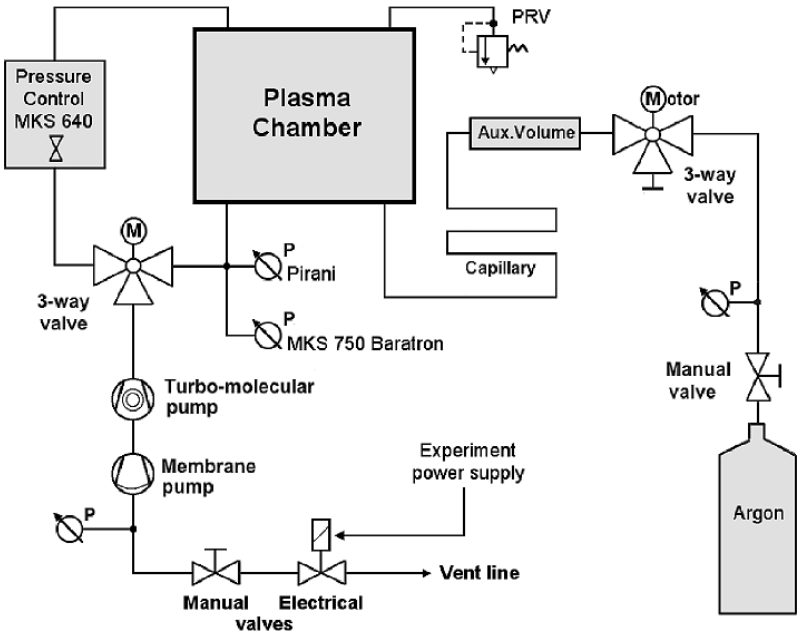

Figure 3.3: *A schematic of the vacuum system. The dead volume in the 3-way-valve between the gas bottle and the chamber rotates to fill the chamber with gas, which is in turn evacuated with the pumps. It is indicated in the figure as a closed connection in the 3-way-valve. In the setup on board the ISS, the membrane pump is replaced by a connection to the vacuum of space. The pressure relief valve (PRV) is also only present in the ground setup. The pressure maintained in the plasma chamber is controlled with the pressure control unit visible in the left. From [202].*

that by the first baratron, as this instrument is located closest to the chamber.

Electrical setup

The electrodes of the discharge chamber have a diameter of 6 cm and a distance of 3 cm. They are made of aluminum, and are surrounded by a ceramic insulator and a grounded guard ring with an outer diameter of 9 cm. The electrodes are mushroom-shaped with a connection to the electrical system in the center. They are usually driven in push-pull mode by an RF field with a frequency of 13.56 MHz. The power from the RF generator is coupled to the electrodes via a matching box that is adjusted to minimize the reflected power.

Microparticles

Microparticles can be inserted into the plasma chamber with the help of dispensers, which are mounted in the ground plates (Figure 3.1b). The particles are stored inside the head of the dispenser, which is shaken electromagnetically, pushing the particles through a fine grid into the plasma. In the experiments described in this work, monodisperse melamine-formaldehyde (MF) particles with a mass density of 1510 kg/m^3 and a diameter of (1–7) µm are used unless otherwise noted[3]. *Monodisperse* in this context means a typical variation

[3]The particles can be obtained from Microparticle GmbH [203].

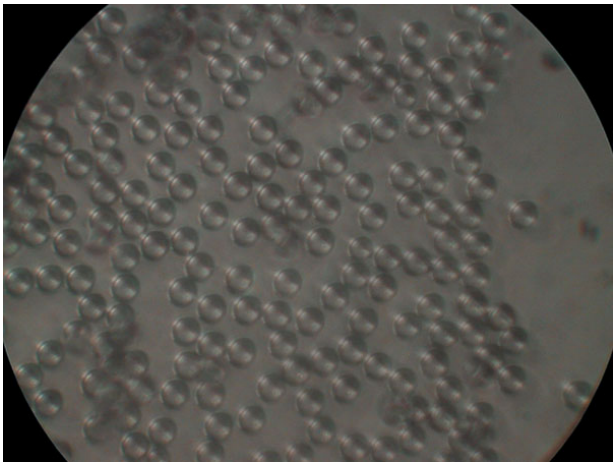

Figure 3.4: *Optical microscopic photograph of MF microparticles. Picture courtesy of M. Kretschmer.*

of the radius of the microparticles of up to a few percent. Figure 3.4 shows a picture of such particles obtained with an optical microscope.

Optics and diagnostics

After ignition of the plasma, microparticles are inserted into the chamber forming a cloud suspended above the lower electrode. Optical access is provided via the four side windows shown in Figure 3.1 and visible in Figure 3.2. The particles are illuminated with laser light from the side. Three different laser diodes were used in the course of this work with wavelength λ and power P: On the ISS, $\lambda = 686\,\mathrm{nm}$, $P = 40\,\mathrm{mW}$ [48], in the ground experiments $\lambda = 686\,\mathrm{nm}$, $P = 45\,\mathrm{mW}$ except for the measurement of the plasma glow in Section 4.3 and during the parabolic flight experiments where $\lambda = 532\,\mathrm{nm}$, $P = 200\,\mathrm{mW}$. The laser beam is spread into a vertical plane with a width of the order of the interparticle distance ($\sim 100\,\mu\mathrm{m}$). The light that is scattered by the particles inside this plane is then recorded with a camera at an angle of 90° to the plane of the laser beam. In Figure 3.2, the laser is visible. The camera usually is mounted on the translation stage, in front of the chamber. Normally, a filter is placed before the lens of the camera to block the plasma glow and ambient light, so that only the laser light is recorded.

On the ISS, charge coupled device (CCD) cameras with frame rates of up to 50 frames per second (fps) are used. The four cameras provide a high resolution view, a view of the plasma glow, an overview, and the quadrant view, which shows approximately one half of the total horizontal length of the area typically occupied by the microparticle cloud, and most of the vertical height. For the analysis of the experiment presented in this thesis, the quadrant view ($35.7\,\mathrm{mm} \times 26.0\,\mathrm{mm}$ at a resolution of $720\,\mathrm{pixels} \times 577\,\mathrm{pixels}$) was used.

In the experiments on ground and during the parabolic flight, a CMOS Photron Fastcam-1024 PCI camera with a resolution of $1024\,\mathrm{pixels} \times 1024\,\mathrm{pixels}$ and a recording speed of up to 1000 fps at the full resolution was used together with a data acquisition system which can record this high data rate for more than 30 minutes. The pixel size is $17\,\mu\mathrm{m} \times 17\,\mu\mathrm{m}$, and various lenses providing for different fields of view were used.

An automatic logging system records housekeeping data such as effective voltages and currents, the power of the RF generator, the temperature of the ground plates and the various pressure measurements.

Scanning

The laser and the camera are mounted on a translation stage, which makes it possible to scan horizontally through the system in the direction perpendicular to the laser plane with a velocity of up to 8 mm/s. The maximal scanning velocity is also limited by requirements of particle tracing: An individual particle should be visible in several consecutive frames for an accurate determination of the horizontal particle position.

3.2 Temperature gradients

In the setup used in ground based experiments, it is possible to heat the lower ground plate of the chamber with eight evenly distributed resistors (shown schematically in Figure 3.1). The upper ground plate is then cooled with two fans. This way, a vertical temperature gradient of up to 2300 K/m can be maintained between the two ground plates.

In the PK-3 Plus laboratory on the ISS, the "top"[4] plate can also be heated, but only to a very small degree. Usually, this option is used to compensate for a heating of the bottom plate caused by close-by electronics. Heating the upper plate at the maximal strength strongly shifts the position of the microparticle cloud due to thermophoresis.

Note that, due to construction reasons, the temperatures are always measured at the ground plates, not directly at the electrodes. The expected differences are of the order of 1 K or less. In addition, in rarefied gases with a temperature gradient perpendicular to a wall, there is a temperature difference between the wall and the gas, which reduces the gas temperature gradient set in the chamber (see Section 2.2.2, page 32).

Therefore, the true temperature difference between the electrodes is a few degrees less than that between the ground plates, ΔT, depending on the gas pressure and the temperature. This leads to a slight overestimation of the strength of the thermophoretic force calculated with the measured value ΔT.

3.2.1 Vertical temperature gradient

In order to study how uniformly the applied heating is distributed in the gas, a numerical simulation was performed with the convection and conduction model of FEMLAB 3.0 without heat sources and in steady-state mode. Details on the simulation are given in Appendix B. Figure 3.5 depicts the obtained distribution of the temperature (Figure 3.5a) and the temperature gradient (Figure 3.5b) inside the plasma chamber assuming that the chamber top cover and bottom base (each comprised of the electrode, guard ring and ground plate) are kept at fixed temperatures of 30 °C and 95 °C, respectively.

As can be seen in Figure 3.5b, the greatest differences in temperature gradient naturally occur near the edges of the guard ring (the gap between the electrode and the guard ring was neglected in this simulation); in the region between the electrodes the temperature gradient is uniform.

[4] *Top* and *bottom* in the context of experiments under microgravity conditions refer to the orientation of the camera view.

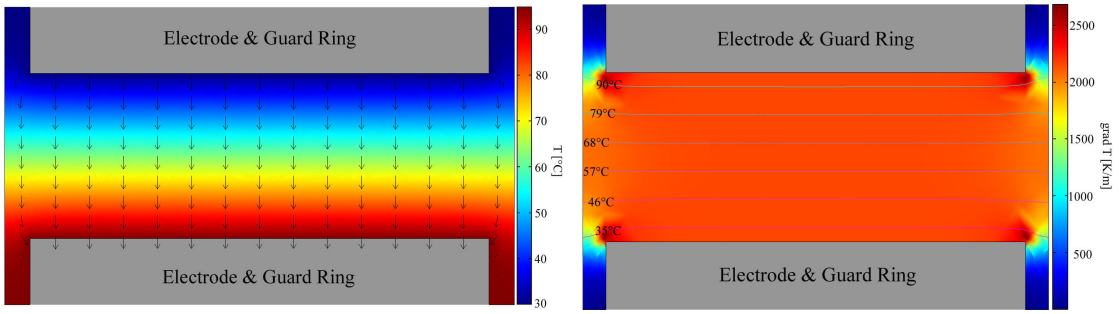

(a) *Color coded temperature distribution with superimposed temperature gradient (arrows).*

(b) *Color coded distribution of the temperature gradient with superimposed temperature contours.*

Figure 3.5: *Simulation of the temperature and temperature gradient distributions in the plasma chamber with a fixed temperature of 30 °C at the upper and 95 °C at the lower plate.*

3.2.2 Horizontal temperature gradient

In real experiments the chamber is not heated uniformly: Only the ground plate is directly heated by the resistors. Since the electrode is mushroom-shaped, it is heated in its center, whereto the mounting transfers the heat from the ground plate. To determine whether a substantial horizontal temperature gradient was produced by this setup, the temperature in the center of the heated electrode (T_c), the temperature on the electrode border (T_b), and that on the guard ring (T_g) were measured in Argon gas at a pressure of 35 Pa with Pt-100 temperature sensors. Figure 3.6 shows the case when the lower electrode was heated to the maximal temperature used in the experiments of this thesis, so that a temperature difference ΔT of 65 K between the two ground plates was obtained. The figure shows the temperature differences $T_c - T_g$ and $T_b - T_g$ as a function of time.

At the beginning of the measurement, when the set ΔT was first attained, the temperature differences between the system elements were the largest. The electrode temperatures were measured to be always lower than those of the guard ring, which is to be expected as the guard ring is positioned directly on the heated ground plate. The temperature of the borders of the electrode was 1.6 K less than that at the guard ring, and the temperature in the center of the electrode was 1.0 K less than at the ring.

Approximately three minutes after $\Delta T = 65$ K was reached, stable horizontal temperature differences were established: $T_g - T_b = 1.0$ K and $T_c - T_b = 0.3$ K. This corresponds to a horizontal temperature gradient of about 10 K/m pointing from the border of the electrode towards the center, and of about 100 K/m pointing to the guard ring from the border of the electrode. These gradients are two to three orders of magnitude smaller than the vertical temperature gradient of 2170 K/m, which is also visible in the simulations shown in Figure 3.5b.

Temperature gradients along a wall immersed in a rarefied gas induce a flow of the gas towards the hotter side (see Section 2.2.2, Page 32). The measured horizontal temperature gradients could cause a flow of the gas along the lower electrode and consequently a

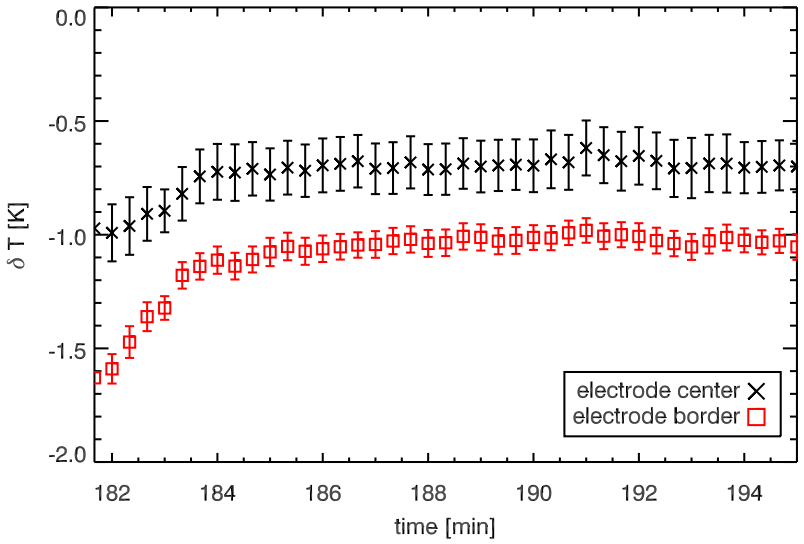

Figure 3.6: *Temperatures δT measured at the electrode center and border relative to those measured at the guard ring, while a temperature difference ΔT of 65 K was applied. The x-axis begins at the time when $\Delta T = 65\,K$ was reached. A stable difference of approximately $\delta T = 0.3\,K$ between the electrode center and its border is clearly seen. The temperature differences between the guard ring and the two positions on the electrode were even stronger ($\delta T = 1.0\,K$ and $\delta T = 0.7\,K$).*

gas convection. However, the vertical temperature gradients are much stronger than the horizontal ones. The thermal creep along the vertical walls thus might induce the gas to flow downwards along the chamber walls, then inwards and back up in the center of the chamber, creating big cylindrically symmetric gas convection rolls. The analysis of the dynamics of the microparticles in the complex plasma might help in detecting such gas convection.

3.3 Analysis techniques

3.3.1 Periodgrams

A common analysis technique applied to the pictures recorded during the experiments in this thesis is the method of *periodgrams*[5]. The pictures used below for illustration show the self-excited waved analyzed in Section 4.1, but the applied method is the same for all cases. First, a horizontal region is selected for analysis, like the region that is marked by two vertical lines in Figure 3.7. The pixel intensities in this region are added up for every position along the propagation direction of the waves, which results in a histogram, such as the one superimposed in Figure 3.7. This procedure is performed for each frame of the analyzed picture sequence. Next, a new image is calculated in which all histograms are plotted next to each other. It is color-coded according to the magnitude of the histograms.

[5]Produced with Interactive Data Language (IDL) routines, which are based on code by U. Konopka [204] that was refined and developed further by the author.

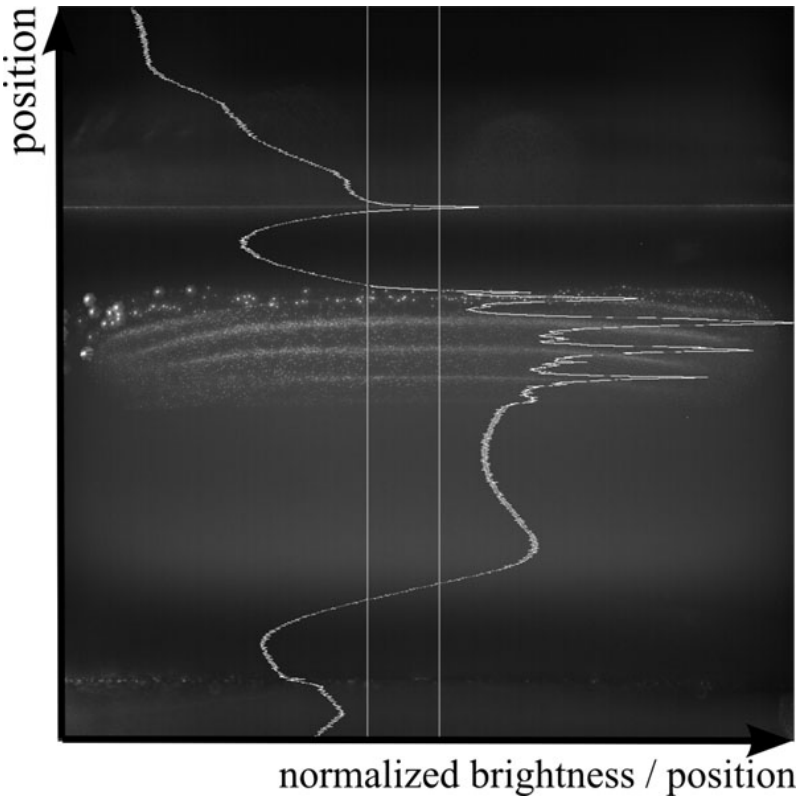

Figure 3.7: *Calculation of a periodgram: A horizontal region of interest is selected, marked by two vertical lines in the figure. For each height, the brightness of all pixels in this region is summarized, producing the points of a histogram such as the one superimposed in the image (white curve).*

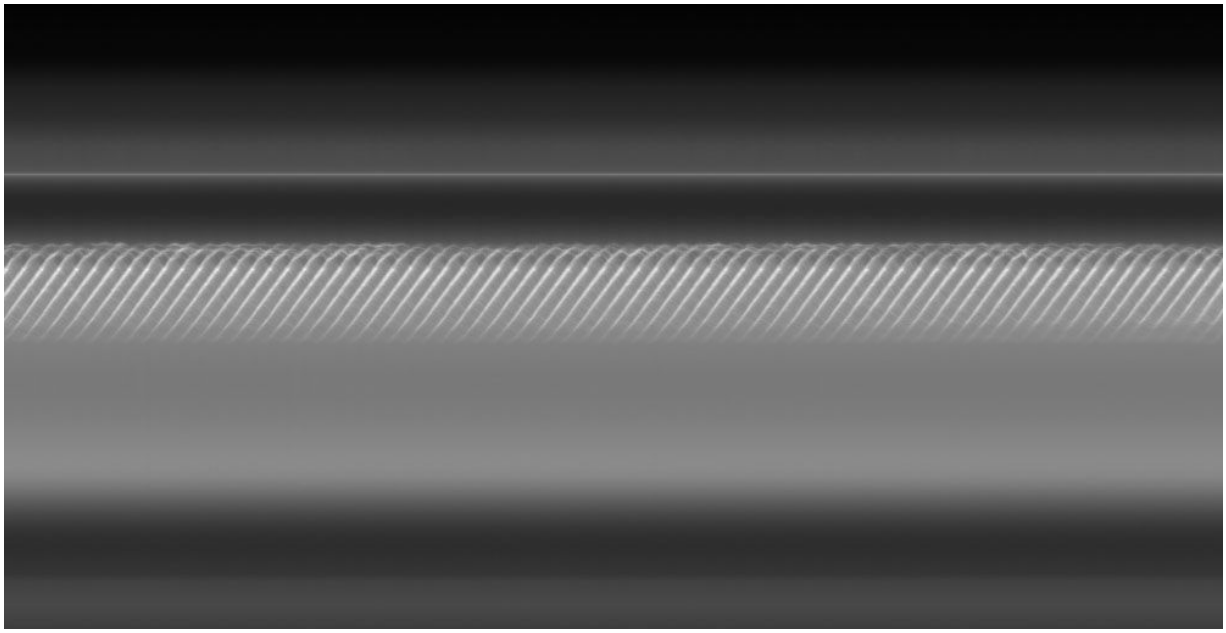

Figure 3.8: *All histograms plotted next to each other result in the periodgram. Here, the horizontal axis corresponds to time, the vertical axis to height. The wave ridges are visible as bright white stripes near the center of the image. The plasma glow can be seen as diffusely glowing region. The upper electrode was illuminated by the laser and is recognizable as horizontal white line in the top of the image.*

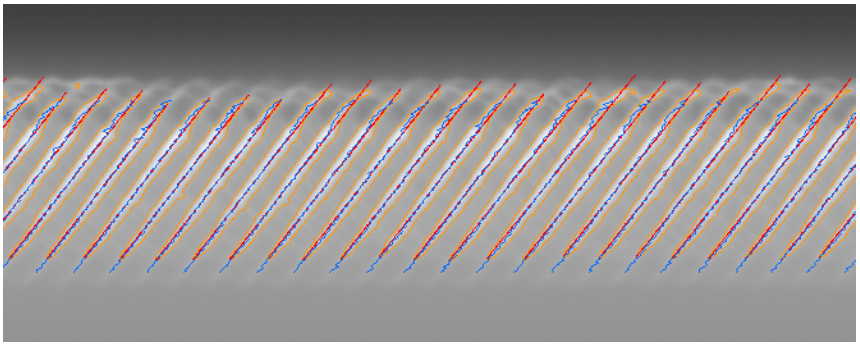

Figure 3.9: *The identified positions of the wavefronts determined from the periodgram 3.8 by plotting brightness contours.*

The resulting image is called *periodgram*. Here, the x-axis corresponds to time and the y-axis to the original height. In the region of the periodgram where particles are present, brightness indicates the density of the microparticle cloud. An example of a periodgram is shown in Figure 3.8.

Finally, the periodgram is analyzed by superimposing and analyzing contours of the brightness, as shown in Figure 3.9, or by correlation analysis methods: The image is shifted either vertically or horizontally until a maximum in correlation with the original image is reached. The corresponding shift is then defined as the distance (vertical shift) or time interval (horizontal shift) between the wave ridges. The wave period can be obtained from the time interval, and the wavelength from the distance between the wave ridges. The obtained data points are then analyzed with standard statistical methods. The wave speed can be determined from the slope of the lines.

Note that for waves traveling in an arbitrary direction the direction of the summation is tilted in such a way to be along the wave front. Periodgrams are also useful for the analysis of many other dynamical effects in complex plasmas, as is shown in Section 4.3.

3.3.2 Particle tracking

The SPIT routines[6] were used to track the particle positions. The operational steps of the particle identification and tracing routines are as follows: First, particle positions are identified in each frame by plotting brightness contours at an adjustable threshold and determining the centers of intensity of each local region found this way. This process can be fine-tuned by changing the intensity threshold above which the particles are identified and by subtracting a fraction of the image background intensity before the particle identification starts. This way, the influence of pixel-locking, which is a common error produced by particle identification routines [205, 206], can be minimized (see Section 3.4). Using this method, it is possible to achieve a sub-pixel accuracy in the determination of the particle positions.

The particles are then traced from the given frame to the next one by predicting the

[6] A collection of routines in IDL developed by members of the complex plasma group at the MPE, notably Uwe Konopa, Robert Sütterlin, and many others.

expected positions in the next frame, e.g., by using the velocities of the particles. The positions in the next frame are then matched with the predicted positions using an adjustable maximal allowed distance between each prediction and the allocated position. If for a given prediction, no new particle position is assigned, the particle is considered lost. More sophisticated searching patterns can also be used, for instance, the particle positions can be extrapolated to the frame after the next one, allowing a certain number of frames in between where the particle is not found. The velocities, forces, etc. are then calculated from the particle positions. This makes possible a treatment of the complex plasmas on the individual particle level and the direct analysis of forces acting on the microparticles.

3.4 Measurement uncertainties

There are several sources for errors in the identified particle positions. *Pixel noise* is the random noise in the brightness of each pixel which arises because of fluctuations in the sensor of the camera and the electronics. Another source of errors is the finite size of the camera pixels, which results in loss of information about the particle's intensity profile and consequently in the *pixel locking effect*: the determined particle positions tend to accumulate around full and half pixel values [205, 206].

Once data is calculated from the particle positions, other sources or uncertainties are added, including those that stem from *poor statistics*. For derived values, the error propagates from the particle positions, e.g., to the velocities.

3.4.1 Pixel noise

The strength of the error induced by pixel noise is estimated by inspecting a particle-free region in the image. A histogram of the recorded intensity values can be used to determine the *noise peak*—the pixel intensities due to pixel noise (and also due to the plasma glow if no filter was used to block the glow in the recording). In the particle identification routine, a threshold for the determination of the particle positions is chosen which is above this noise peak. Comparing with the particle free stripe shows that there the number of pixels with intensities above this threshold is usually small. Also, single pixels above the threshold ("particles" with diameter 1) are discarded in the particle identification routine.

For instance, in Section 4.2, a particle-free stripe of size $35.1 \times 0.45\,\mathrm{mm}^2$ was examined. The number of pixels above the noise peak was less than 1 %.

3.4.2 Pixel locking

In order to minimize the pixel locking effect, a baseline value is subtracted from the original images before the particle identification routine is run. The threshold for particle identification is then chosen as low as possible while still resulting in reasonable particle identification[7].

[7] A simple sanity check is that no particles are identified at positions where no particles are visible by eye and vice versa, particles which are well visible by eye should be identified by the routine.

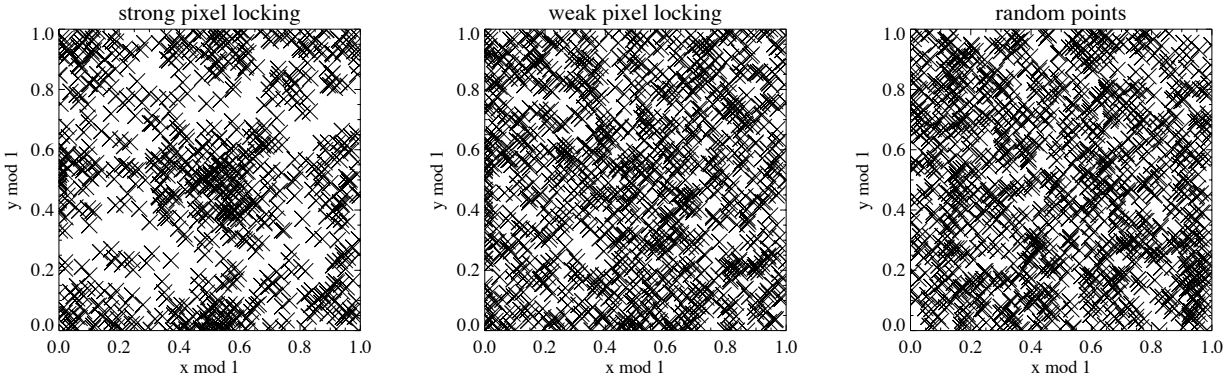

Figure 3.10: *Sub-pixel map of identified particle positions obtained with an unadjusted routine (left), a better adjusted routine (center), and random particle positions for comparison (right).*

To visualize the strength of pixel locking, sub-pixel maps of the found particle positions are plotted as shown in Figure 3.10. In this figure, an image from an experiment presented in Section 4.3 is analyzed and the identified sub-pixel particle positions (the positions modulo 1 pixel) are plotted. On the left, the result of an unoptimized routine applied to the image is shown. The pixel-locking effect is clearly visible, the particle positions are clustered in the center and on the sides of the map.

In the middle of Figure 3.10, a baseline and low threshold are used with the same particle identification routine and the same original image. The pixel locking effect is much less pronounced than before. Most noticeable is the slight accumulation of particle positions near $x \bmod 1 = 0$ which is still present in the figure.

For comparison, completely random particle positions are shown on the right in Figure 3.10 for the same number of particles as in the image in the middle.

To optimize the particle identification results, therefore, the parameters such as the baseline must be carefully selected to minimize the pixel locking effects while identifying as many particles as possible, in a similar way as described in [205].

3.4.3 Errors of the particle identification routine

In the experiment presented in Section 4.2, an agglomerated particle was lying immobile on the lower electrode. In order to estimate the error stemming from pixel noise and at the same time that induced by the particle identification routine, this particle was traced. The maximal resulting error in the position was measured to be of the order of 0.1 pixels. The error in velocities propagated from this uncertainty is estimated as 0.35 mm/s.

For smaller particles, the images of which occupy a smaller number of pixels, the identified positions are less precise. A slight defocussing of the camera lens when recording the image may improve the quality of the identified positions [205].

3.4.4 Errors from poor statistics

The largest uncertainty stems from statistical variations of the measured data used for analysis. To determine a mean value of a measured parameter, either the empirical mean and corresponding standard deviation is calculated, or, if the number of measurements is high enough, all determined values of this parameter are plotted and a Gaussian is fitted to the result. The resulting standard error is shown in the corresponding plots.

Chapter 4

Experiments

A phenomenon found very often in complex plasmas are dust acoustic waves. In the ground setup, these waves appear when the gas pressure is decreased: First, the particles closest to the cloud edge start to oscillate vertically. If the pressure is decreased further, the oscillations spread inside the microparticle cloud until all particles are participating, and waves are traveling inside the cloud towards the closest chamber wall. At this stage, the waves usually have a regular appearance, with wavefronts that are dominantly aligned parallelly to the discharge electrodes, and only few bifurcations of the wave ridges are seen. With decreasing pressure the waves become increasingly strong and non-linear, the wavelength grows, and the wave pattern turns more and more irregular, with many bifurcations.

Figure 4.1a shows a complex plasma that was composed of 6.8 µm MF particles at

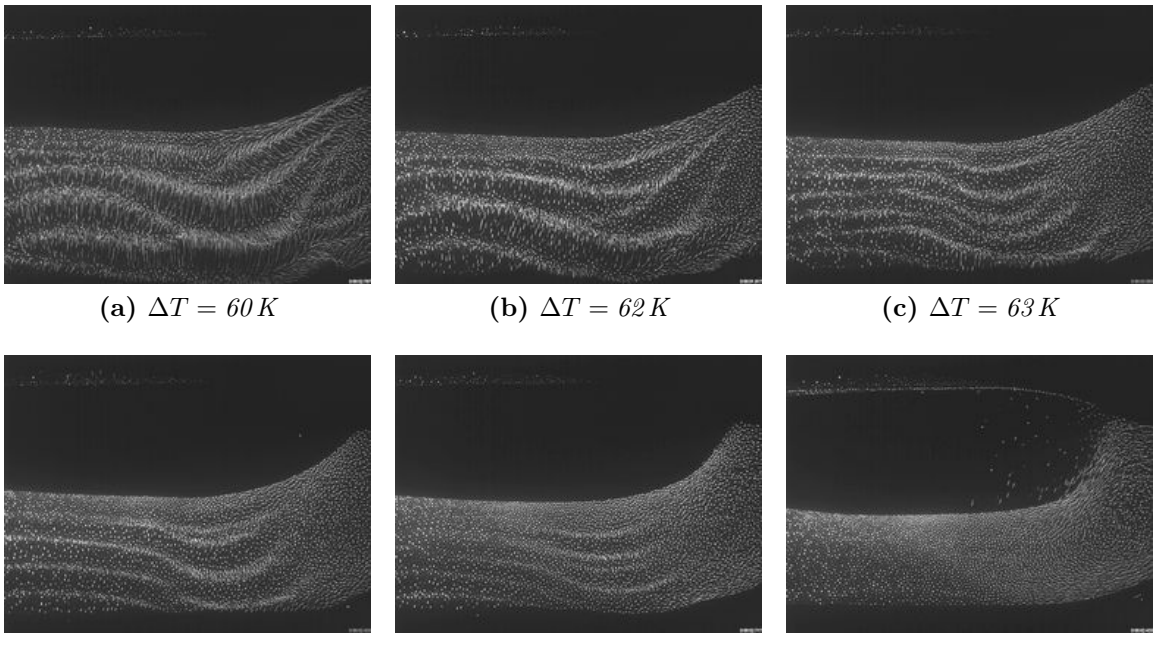

(a) $\Delta T = 60\,K$ **(b)** $\Delta T = 62\,K$ **(c)** $\Delta T = 63\,K$

(d) $\Delta T = 64\,K$ **(e)** $\Delta T = 65\,K$ **(f)** $\Delta T = 66\,K$

Figure 4.1: *Experiment in Argon with 6.8 µm particles at a pressure of 18.5 Pa (FoV: 27×21 mm²). From a) to f), the temperature differences ΔT between the ground plates were increased. The waves disappeared at higher ΔT.*

a temperature difference between the upper and lower ground plate of $\Delta T = 60\,\mathrm{K}$ in the PK-3 Plus setup. The behavior of the particles in this stage corresponds to the low pressure stage without the influence of thermophoresis.

Experiments in which a temperature gradient is used to levitate the microparticles are well suited for studying waves, as the vertical position of the microparticle cloud can be controlled by thermophoresis. When the temperature gradient applied to this system was increased, lifting the microparticles away from the sheath region of the plasma, the wave patterns were affected. They became more regular and less strong (Figure 4.1b–e), just as an increase in pressure would cause. Finally, at $\Delta T = 66\,\mathrm{K}$, the waves completely disappeared, indicating a violation of the excitation condition, and a homogeneous, stable microparticle cloud could be observed (Figure 4.1f). The cloud structure changed and the beginning of the formation of the central void (particle free region) typical for complex plasmas under microgravity conditions was clearly seen (the upper part of the cloud in Figure 4.1f), indicating that gravity was almost compensated by the thermophoretic force.

The fact that the waves disappeared at this stage of gravity compensation demonstrates the important influence of the sheath on the excitation conditions, as does the fact that intense self-excited waves have never been observed under microgravity conditions on board the ISS, where the microparticles are confined in the bulk of the plasma.

An additional increase of the temperature gradient above the point of gravity compensation (towards the realization of "negative gravity" conditions) caused the microparticles to flow around the void and accumulate in the top region of the chamber. Then, if the temperature gradient was increased even further, waves were again formed, but at the top of the chamber, symmetrically to those observed before at the bottom.

In Section 4.1, these self-excited waves are examined under various applied temperature gradients and effective gravity conditions. The motion of the microparticles, depicting their path through and between the wave ridges, is traced and analyzed at the kinetic level. Waves obtained under microgravity conditions (on board the ISS) are studied in Section 4.2. In these experiments, the waves were excited externally by applying a modulation voltage to the electrodes. This allows to examine the response of the complex plasma to these external fields of various modulation frequencies.

Returning to Figure 4.1 and the setup on ground, sometimes an additional effect was induced in the complex plasma when the thermophoretic force just compensated gravity: At low powers and high microparticle number densities and pressures, first particles started to move through the void. This can be seen already in Figure 4.1f on the right side. Changing some control parameter (e.g., injecting more particles) at this stage often led to a completely new fluid effect in complex plasmas: the formation of bubbles, blobs, and cusps near the lower void boundary. This effect is analyzed in detail in Section 4.3.

4.1 Self-excited dust density waves

4.1.1 Observations during a parabolic flight

Waves are commonly observed in experiments with complex plasmas during parabolic flights with high particle densities and low pressures (e.g., [207–209]), and under some

Figure 4.2: *Uniform complex plasma cloud obtained during a parabolic flight. FoV: 33.6×16.7 mm², pressure 13.3 Pa, 6.8 µm MF particles. The interparticle separation was* $\Delta \simeq 320\,\mu m$.

particular conditions, they even appear reproducibly at low pressures and not at higher ones [210]. However, on parabolic flights, the system responds sensitively to the inevitable variations in effective gravity (a parabola is considered "good" if ± 0.05 g is achieved, see Section 1.3.2). This makes it difficult to distinguish waves excited by the fluctuations in gravity from real "self-excited" waves.

In order to verify that waves can be self-excited when the pressure is lowered below the excitation threshold, a series of experiments in an Argon complex plasma was performed on the 13th DLR parabolic flight campaign. Typical values of the control parameters were a power of 160 mW, a peak-to-peak voltage of 50 V and a peak-to-peak current of 15.6 mA. MF particles of diameter 3.4 or 6.8 µm were inserted into the system once the low gravity phase was reached, and the pressure was initially set to a value at which no self-excited waves were expected to appear (at first $p > 30$ Pa, during later parabolas the experiments were started at lower pressures). Then the pressure was lowered to (13–15) Pa during the ~ 20 s of low gravity with the goal to reproducibly reach the critical pressure for the excitation of waves.

After the low gravity phase ended and gravity increased to 1.8 g, the particles fell down towards the lower sheath, where they were suspended above the electrode by the strong sheath electric field. At this stage, intense waves were observed. However, during the low gravity phase, in none of the ten parabolas dedicated to these experiments self-excited waves appeared. On the contrary, the microparticle system was very stable. Figure 4.2 shows an image of a complex plasma during a parabola at a pressure of 13.3 Pa with 6.8 µm particles. The conditions were thus similar to those reported in [79], where dust density waves were observed. A notable exemption is the microparticle number density, which is given as $n_\mathrm{d} = 5 \cdot 10^{10}\,\mathrm{m}^{-3}$ in [79] for the same particle size, whereas in the experiment presented here, $n_\mathrm{d} \simeq 7 \cdot 10^{9}\,\mathrm{m}^{-3}$.

Thus, it cannot be excluded that at higher microparticle number densities, lower pressures, or higher discharge powers, self-excited waves would have appeared, but the results obtained so far again suggest that an external disturbance of the system is needed in order

to excite waves, such as gravity pushing the particles deeper into the sheath. Further investigations are required to solve this question.

The influence of external disturbances on self-excited waves can be analyzed by varying the force with which the grains are pushed into the sheath. One technique to achieve this is to apply a variable thermophoretic force.

4.1.2 Observations on ground

The self-excited waves were investigated[1] in ground-based experiments with the discharge chamber of the PK-3 Plus setup filled with Argon gas at pressures between 10 and 40 Pa at a very small symmetrical gas flow. Microparticles with diameters of (1–2) µm were injected into the system, and a typical peak-to-peak voltage was 30 V. Under these conditions, the amount of disruption of the observed waves, such as bifurcations and bending of the wave ridges, was minimal.

Figure 4.3 shows an example of a pattern shown by such self-excited waves, using MF particles with a diameter of (1.28 ± 0.06) µm and a mass density of $1510\,\mathrm{kg/m^3}$. Additionally, a relatively small number of bigger particles was present in the chamber, presumably agglomerates, visible in the figure near the top of the cloud. They did not influence the dynamics of the density waves.

The microparticles were suspended at a certain height against gravity by electric and thermophoretic forces, and were illuminated with the vertically expanded sheet of light from the diode laser. The light scattered by the microparticles was recorded with the high speed camera specified in Section 3.1 at a frame rate of 1000 fps and a spatial resolution of 1 Mpixel at 45.6 µm/pixel, allowing highly resolved measurements.

[1] The essence of the work described in this section was published in [107] with the co-authors M. Rubin-Zuzic, S. Zhdanov, H. M. Thomas, and G. E. Morfill.

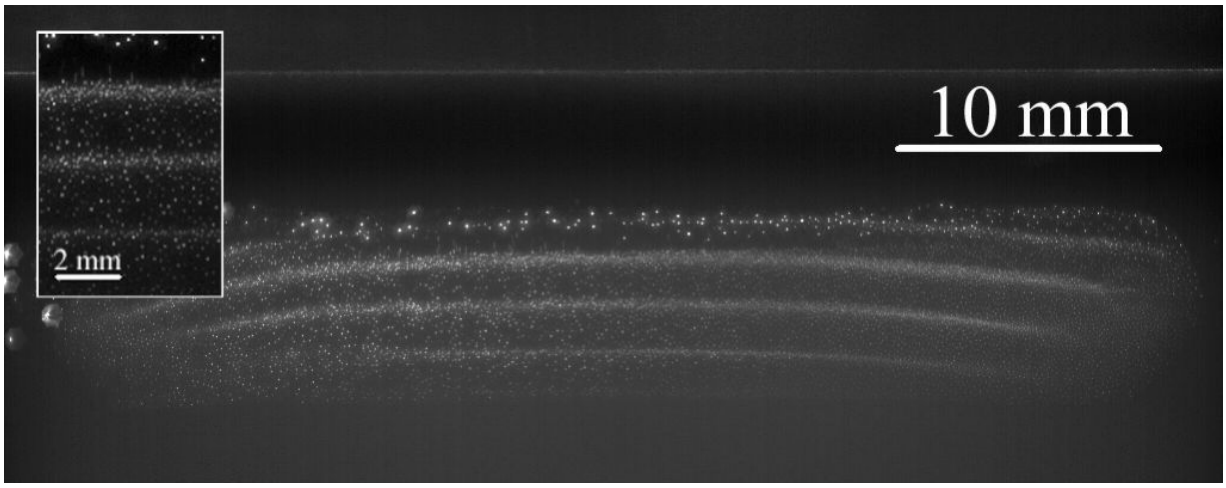

Figure 4.3: *Sideview of self-excited waves and zoom into the picture (inset). The horizontal line indicates the position of the upper electrode. Near the upper edge of the microparticle cloud bigger particles are visible as brighter spots.*

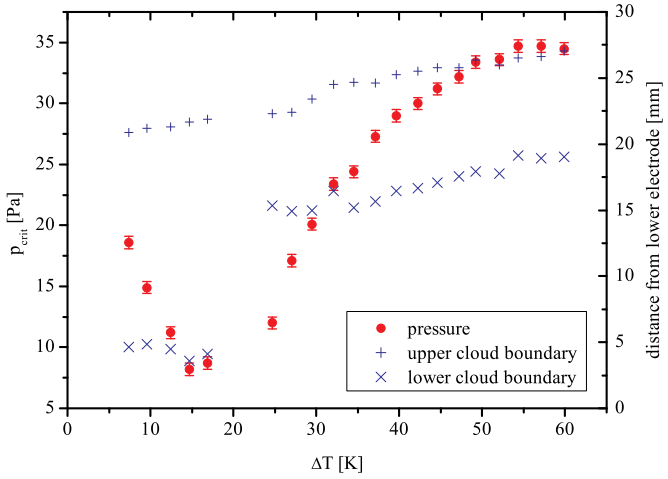

Figure 4.4: *Critical pressure for the onset of self-excited waves (red dots) in an Argon plasma with SiO_2 particles of diameter 1.55 µm, and positions of the edges of the particle cloud (+: upper, ×: lower edge) as a function of the temperature difference between the ground plates (bottom axis).*

4.1.3 Critical pressure

When the pressure was decreased below a certain threshold, waves were excited in the complex plasma. Figure 4.4 shows this threshold—the *critical pressure* below which waves were present—in an Argon plasma with (1.55±0.04) µm SiO_2 particles with a mass density of $\rho = (1.8\text{–}2.0) \cdot 10^3\,\mathrm{kg/m^3}$ as function of the applied temperature difference. The measured positions of the upper and lower boundaries of the particle cloud are also plotted. The increasing levitation height of the particles with higher temperature gradients is well visible.

Again, there were no self-excited waves in the parameter range where gravity was approximately compensated by the thermophoretic force ($F_{\mathrm{eff}} = F_{\mathrm{th}} - m_{\mathrm{d}} g = 0$)—visible in the figure as the range where the lower boundary of the particle cloud was moved above the center chamber. The waves were only present when the particles were pushed into the sheath region. The stronger this force was, the higher the pressures are at which the waves appeared. This held both for the range above and below the threshold $F_{\mathrm{eff}} = 0$.

4.1.4 Excitation mechanism

In the following, a complex plasma consisting of the more usual MF microparticles (1.28 µm diameter, as in Figure 4.3) and Argon gas is investigated. These small particles have the advantage that the excited waves were very fast, so that it was easier to achieve a wave pattern of great clarity. Figure 4.5 shows that in this system, the critical pressure again increased with the temperature gradient in a domain where the thermophoretic force acting on the particles exceeded gravity (see the top axis in Figure 4.5), so that the *effective gravity*

$$\mathbf{g_{eff}} = \mathbf{F_{eff}}/m_{\mathrm{d}} = \mathbf{g} + \mathbf{F_{th}}/m_{\mathrm{d}} \tag{4.1}$$

was directed oppositely to $\mathbf{g}$ ($\mathbf{g}$ is directed downwards, $\boldsymbol{F}_{\mathbf{th}}$ upwards). The particle cloud thus occupied the upper part of the chamber, as in Figure 4.3. The cloud was compressed by the thermophoretic force, in analogy to the compression of the objects in [109], which developed plastic flow zones.

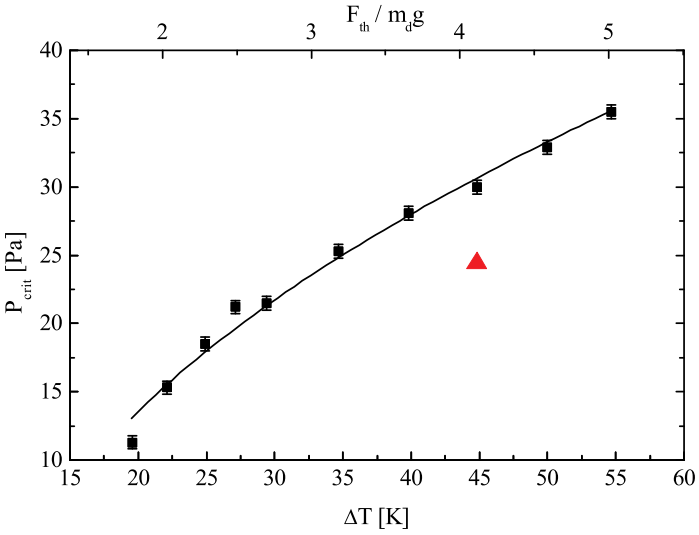

Figure 4.5: *Critical pressure for the onset of self-excitations in an Argon plasma with 1.28 µm MF particles versus the temperature difference between the ground plates. The top axis shows values of the normalized thermophoretic force calculated by using equation (2.52). The solid line is a fit. The position of the red triangle corresponds to the conditions investigated more closely below.*

In the regime where the waves were excited, the observed growth in p_{crit} is easy to explain supposing that the waves were triggered by the streaming ion instability (with a growth rate $\gamma \propto v_i - v_*$ [90, 117], where $v_i = \mu E$ denotes the ambipolar diffusion speed, $\mu \propto p^{-1}$ is the ion mobility, p designates the pressure, and v_* is the parameter from [90]), and furthermore assuming that the waves were stabilized by particle-gas friction, hence $v_i - v_* \propto p$ at the instability threshold. From the force balance

$$F_{\mathrm{th}} - m_{\mathrm{d}} g \approx Z_d e E_{\mathrm{crit}}, \tag{4.2}$$

the ratio $F_{th}/m_{\mathrm{d}}g$ is obtained as a polynomial function of p, assuming a constant Z_{d} and v_* in the relevant range of parameters:

$$\frac{F_{\mathrm{th}}}{m_{\mathrm{d}} g} - 1 \propto \frac{v_{\mathrm{i}}}{\mu} \propto p v_{\mathrm{i}} \tag{4.3}$$

$$\propto p(p + p_0). \tag{4.4}$$

The constant p_0 can be obtained from the experiment.

A least squares polynomial fit to the experimental data results in

$$p/p_0 = \sqrt{F_{\mathrm{th}}/m_{\mathrm{d}} g - 1 + \epsilon^2} - \epsilon, \tag{4.5}$$

$$p_0 = (21 \pm 1)\,\mathrm{Pa}, \tag{4.6}$$

$$\epsilon = 0.31 \pm 0.08, \tag{4.7}$$

which supports the assumption that the waves were triggered by the streaming ions. The density waves propagated in the direction of effective gravity, which was also the direction of the ion drift.

4.1.5 Wave parameters

Figure 4.6 shows the periodgram taken over all 2000 pictures recorded during the experiment. The conditions are marked by the triangle in Figure 4.5. Each vertical column

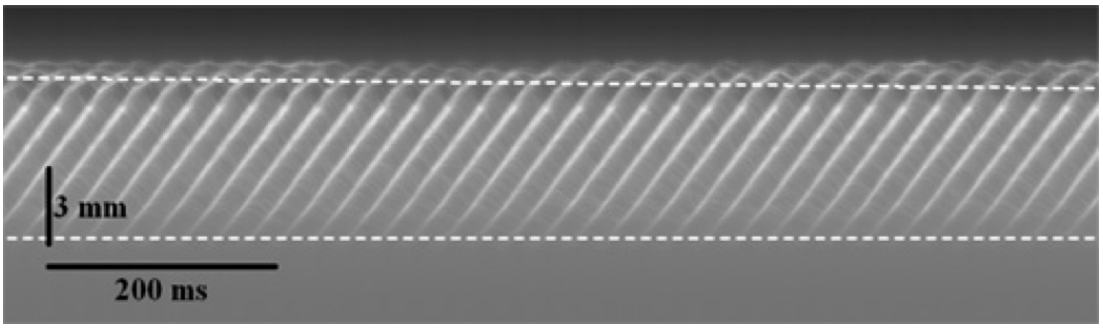

Figure 4.6: *Periodgram of the waves. The plot abscissa corresponds to time, the ordinate to height and the brightness to the re-normalized sum of all pixel intensities in a 4.56 mm wide central region (inset of Figure 4.3). The horizontal dashed lines mark the boundaries of the plot area used for analysis. Scales are shown as black stripes.*

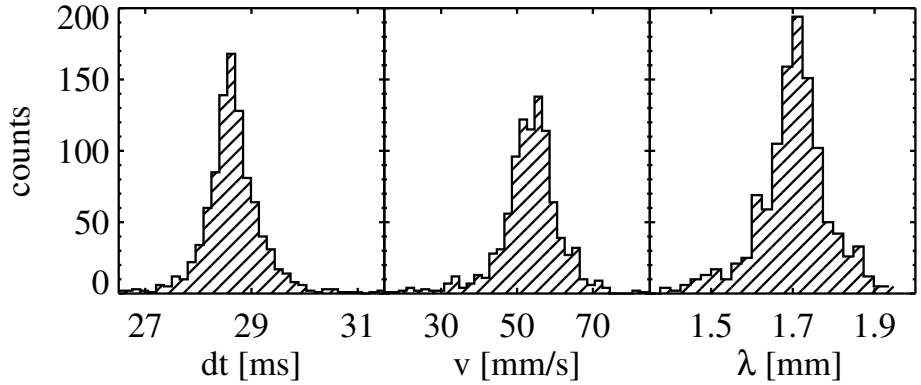

Figure 4.7: *Distributions of the wave parameters determined from the periodgram.*

in this picture (corresponding to a fixed time moment) was plotted by averaging over a 4.56 mm wide horizontal area of the central part of the image, as shown in the inset in Figure 4.3. The wave parameters were determined from the periodgram with the method of intensity contours (Section 3.3.1). Their distributions are shown in Figure 4.7.

The means of the data were determined by fitting a robust Gaussian to the smoothed histograms. The average phase velocity turned out to be $\langle v \rangle = (56 \pm 4)$ mm/s, the average wave period was $\langle dt \rangle = (28.8 \pm 0.9)$ ms, and the wavelength was $\langle \lambda \rangle = (1.73 \pm 0.05)$ mm. (The error in the phase velocity stems from the linear fit to the slope, the error in the period from pixel noise and the error in the wavelength from the camera resolution.) The phase velocity changed slightly with height ($< 20\,\%$), while the period remained practically unchanged. With the velocity of 5.6 cm/s, the waves were relatively fast, for example compared with those examined in [79], which had a phase velocity of 1.6 cm/s.

4.1.6 Particle dynamics

The sequence of images obtained with the high-speed camera are of high quality, and tracing the microparticles from one frame to the other was possible. The uncertainty

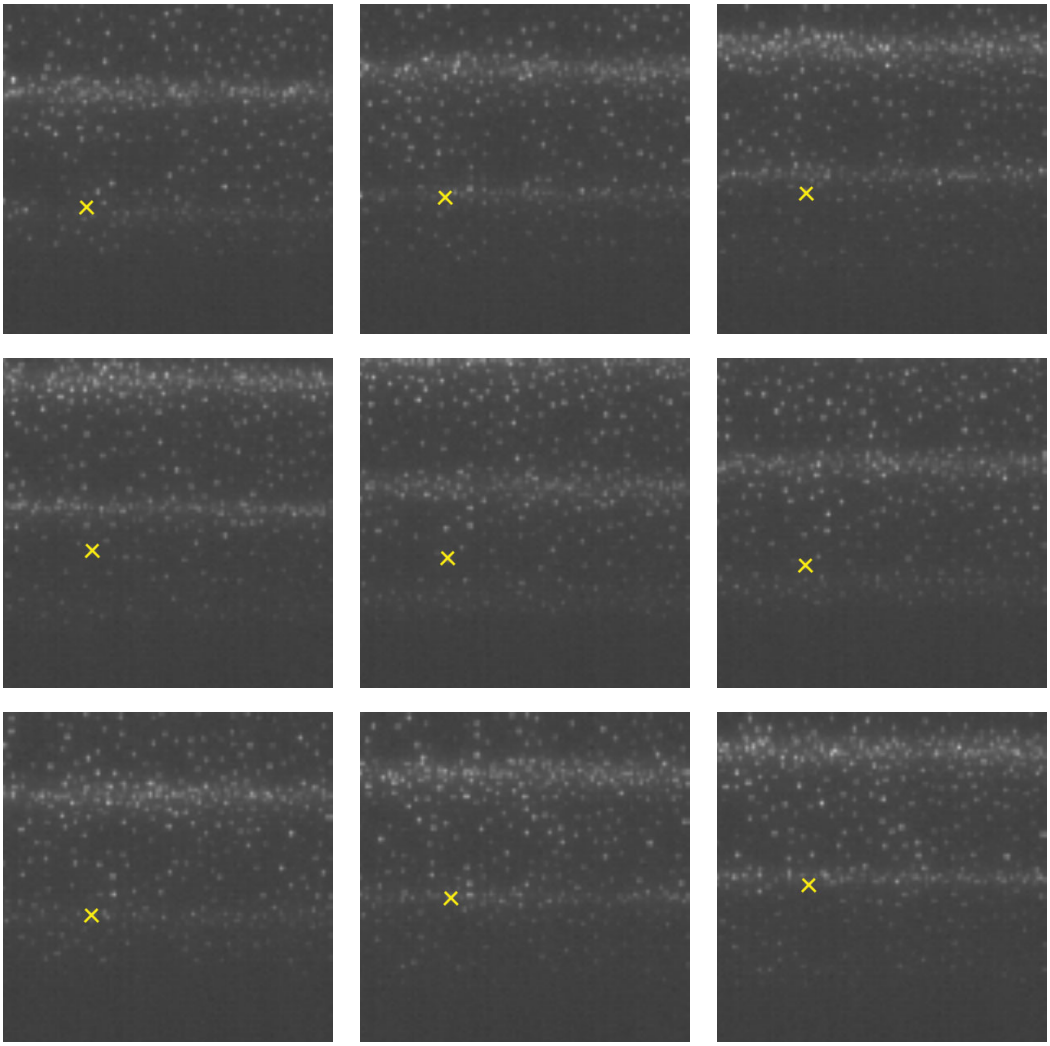

(a) *Images showing a single traced particle, which is marked with a yellow cross. The time steps between the frames are 5 ms, the field of view is 4.5×4.5 mm², the sequence runs from left to right and top to bottom. It corresponds to a little less than the first half of the measurements shown below.*

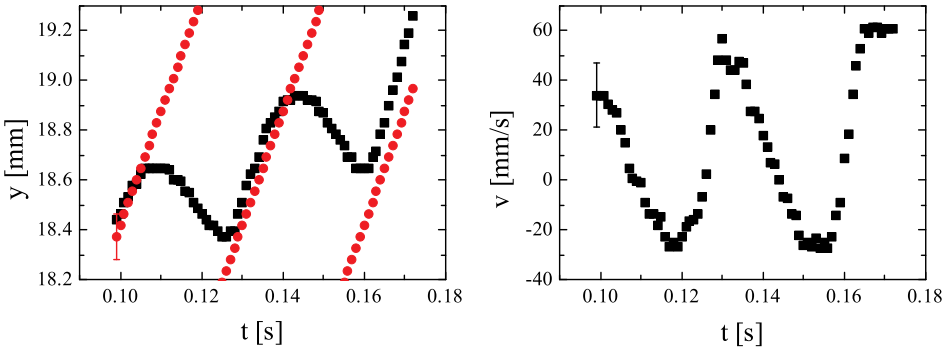

(b) *Left: Found particle positions (black squares) and wave front positions (red circles). Right: Derived vertical particle velocities as a function of time. For clarity, error bars are shown for the first points only.*

Figure 4.8: *A single traced particle, its vertical position and velocity.*

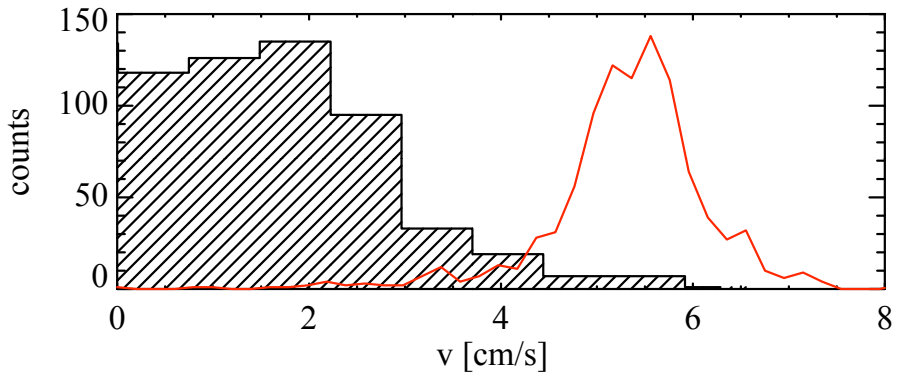

Figure 4.9: *Histogram of the velocities of the well-resolved particles and the wave speed distribution (red line).*

in the determined particle positions was estimated as ±9.1 µm, resulting in an error of the velocity of individual particles of ±12.9 mm/s. Figure 4.8 shows an example of one particle interacting with the passing wave fronts. As can be seen in Figure 4.8a, the particle first was caught by the wave, moved with it upwards for some distance, while at the same time slowly moving *within* the wave front from its top to its bottom (top row in Figure 4.8a). Then, the particle left the wave ridge and relaxed back towards its original position (middle row), until caught by the next wave front (bottom row). These stages were repeated quasi-periodically. The drift stage corresponds to a resonant interaction.

Figure 4.8b shows the measured particle positions and the wave front positions as well as the velocities derived from the particle positions. The particle was accelerated up to a velocity of (6±1) cm/s, which corresponds to the wave velocity.

Sometimes, the particles were even carried along with the wave, but this was a rare process under the present experimental conditions. Figure 4.9 demonstrates this by showing the velocities of the well-resolved particles and the distribution of the wave velocities.

Chaotic or convective type motions of particles were very weak in the center of the cloud. They were amplified towards the edges, where circulations existed, though relatively feeble similar to those observed in [183]. In the following, only the central part of the microparticle cloud, which was free of circulations, is considered.

Particles were lost from the viewing plane mainly due to enhanced scattering on the denser wave ridges. To ensure good statistics, only the tracks consisting of more than 20 positions were used in the analysis. For convenience, the identified tracks are divided into two groups: Longer trajectories crossing at least several ridges are termed as 'well resolved' (about 130 events). They can serve as a probe of either a long-range or an in-front wave field. The remaining trajectories (about 2700 events) often broke off at wavefronts and formed a halo underneath the wave ridges. Hence, they are natural (and statistically well-defined) tests of the out-of-front field structure.

The net force acting on the particles can be calculated from the particle positions using the relationship

$$F_{\mathrm{net}} = m_{\mathrm{d}} a + \gamma_{\mathrm{Ep}} m_d v, \tag{4.8}$$

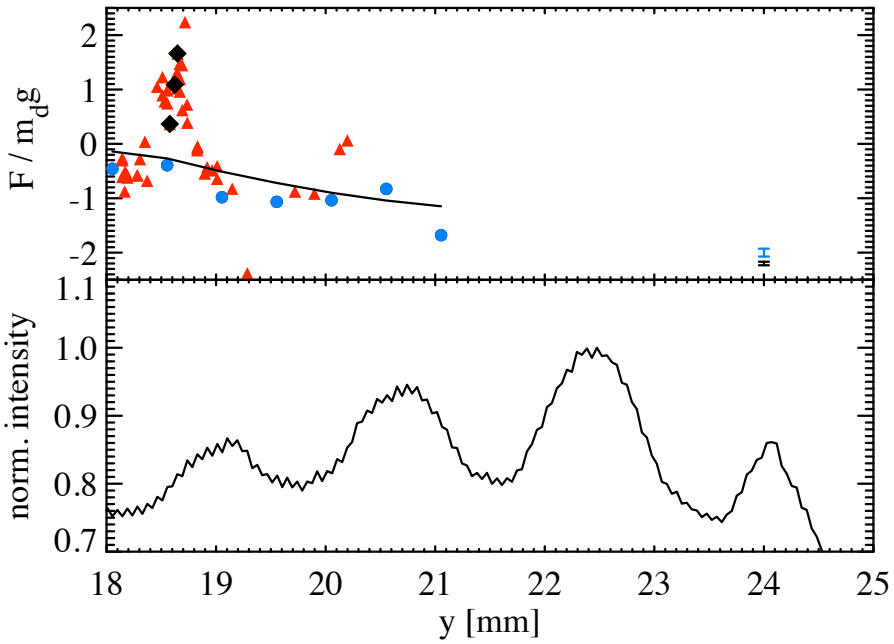

Figure 4.10: *(top) Net force acting on the particles in one phase of the wave as a function of height above the lower electrode, red triangles: well resolved particles, blue dots: current mean force acting on all traced particles, dashed line: total mean of all traced particles, black diamonds: force-field calculated along the trajectory of the particle shown in Figure 4.8. The error bars corresponding to the standard errors are shown to the right. (bottom) Positions of wave ridges vs. height above the lower electrode taken in the same phase from the periodgram (Figure 4.6). Note that the positions of force peaks (a) are shifted backwards compared with the maxima of the emission intensity.*

where m_d designates again the mass of the microparticles, and a and v are the particle acceleration and velocity. The Epstein drag coefficient γ_Ep [166] as in equation (2.39) here has the value $\gamma_\mathrm{Ep} = 236\,\mathrm{s}^{-1}$.

Figure 4.10 shows the result of the calculations taken in the same phase of the waves with the well-resolved particles (long tracks) and with all traced particles (mainly short tracks). In both cases, a periodical rise and fall in the force due to the periodic passage of the wave is clearly observable. The mean force in the second case is less than that calculated with the long-track particles, mostly because of the tracking problems mentioned above. For comparison this plot is superimposed with the force extracted from the trajectory of the resonant particle in Figure 4.9 in the same phase. A movie showing the force in different wave phases and demonstrating the upward propagation of the wave is available online [211]. The total mean of the force irrespective of the wave phase (the line in Figure 4.10) turned out to be non-zero and increased in magnitude with height. The distribution of this mean field is fitted well by the line

$$F = -\Omega_0^2 m_\mathrm{d}(y - y_0). \tag{4.9}$$

Here, Ω_0 is the angular frequency (the spring constant) and y_0 is the rest position. The measurement yields $\Omega_0 = (56 \pm 4)\,\mathrm{s}^{-1}$.

4.1.7 Forces

An important topic is the origin of the forces experienced by the particles inside a wave ridge. Using the model for the thermal conductivity for two-component materials described in [212], the expected variation in the thermophoretic force due to the presence of the microparticles was measured as $\Delta F_{\mathrm{th}}/F_{\mathrm{th}} \sim 10^{-7}$. The additional force due to particle overheating [213] was also very small: $F/F_{\mathrm{th}} \sim 10^{-4}$ for the present experimental conditions. Hence, the expected variation of the thermophoretic force caused by the influence of the microparticles is negligible.

Earlier it was shown that the waves were excited when the electric field exceeded a critical value E_{crit}, and that the collective excitations were controlled by particle fluxes and energy conservation. The particle flux can be characterized by a simple balance taken forward (subscript 1) and backward (2) of the wave front:

$$n_1(c - v_1) - n_2(c - v_2) + \frac{d}{dt}(nL) = 0, \tag{4.10}$$

where $n_{1(2)} = 3/(4\pi\Delta_{1(2)}^3)$ are the particle densities, and $\Delta_{1(2)}$ and $v_{1(2)}$ denote the particle separations and velocities. The wave velocity is designated by c as above, and nL is the particle density inside the wave ridge multiplied by the width of the ridge. Using tracing results in the estimate (in a domain $18\,\mathrm{mm} < y < 19\,\mathrm{mm}$ corresponding to the peak force in Figure 4.10): $\Delta_1 = 173\,\mu\mathrm{m}$, $\Delta_2 = 295\,\mu\mathrm{m}$, and the averaged (unperturbed) particle separation $\langle\Delta\rangle = 232\,\mu\mathrm{m}$.

Using these values yields $n_1 = 4.6 \cdot 10^{10}\,\mathrm{m}^{-3}$, $n_2 = 9.3 \cdot 10^{9}\,\mathrm{m}^{-3}$, and the averaged cloud density $\langle n\rangle = 1.9 \cdot 10^{10}\,\mathrm{m}^{-3}$, so that the compression factor equals: $(n_1 - \langle n\rangle)/\langle n\rangle \simeq 1.4$.

To estimate plasma parameters results of Langmuir probe measurements performed in [140] under similar conditions, but in a different chamber geometry, are extrapolated. An electron temperature T_e of (3–4) eV was measured, therefore here $T_e = 3.5\,\mathrm{eV}$ is assumed. Extrapolating results of measurements in the central part of the chamber provides an estimate of the ion density of $n_i = 2 \cdot 10^{14}\,\mathrm{m}^{-3}$ ($4 \cdot 10^{14}\,\mathrm{m}^{-3}$ according to simulations of the PK-3 Plus chamber [91]) for the present conditions.

Utilizing these values and $Z_{\mathrm{d}} = 2300$ as estimated below, the dust acoustic speed (2.64) is $c_{\mathrm{DAW}} = 3.7\,\mathrm{cm/s}$. This yields a Mach number $\mathcal{M} = c/c_{\mathrm{DAW}} = 1.5$, confirming that the waves were really non-linear.

4.1.8 Charges

In order to estimate the charges of the microparticles, it is assumed that the kinetic energy E_{kin} of the fast microparticles outside of the wave fronts (index 1) was partially converted into potential electric energy U_{E} when they were stopped by the electrostatic repulsion of the microparticles inside the dense wave ridge (index 2). Using the usual screening of the

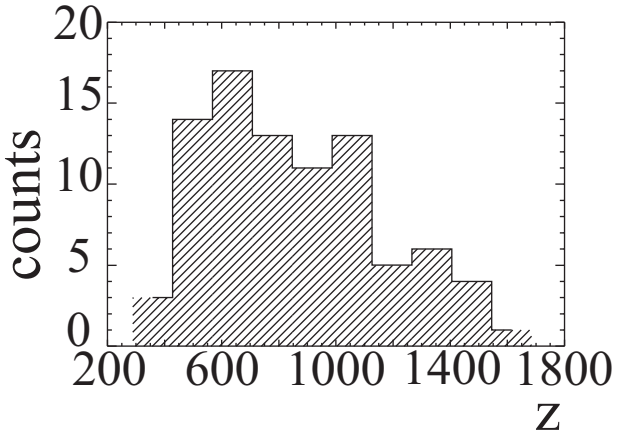

Figure 4.11: *Re-normalized charge distribution of well resolved particles calculated with equation (4.14).*

electric potential on length scales of λ_D, the excess of electric potential energy inside the wave ridge is given by

$$U_\mathrm{E} = \frac{q_\mathrm{d}^2 \lambda_\mathrm{D}^2}{\epsilon_0}(n_2 - n_1), \tag{4.11}$$

assuming a simple model of symmetric screening [151, 153] and a constant charge of the microparticles, q_d. The energy balance then reads as

$$E_{\mathrm{kin},1} = E_{\mathrm{kin},2} + U_\mathrm{E} \tag{4.12}$$

$$\frac{q_\mathrm{d}^2 \lambda_\mathrm{D}^2}{\epsilon_0}(n_2 - n_1) = \frac{1}{2} m_\mathrm{d} \left((c - v_1)^2 - (c - v_2)^2 \right). \tag{4.13}$$

Here, c is again the speed of the wave ridges, and $v_{1,2}$ denotes the velocity of the microparticles outside, inside the wave ridges respectively. Expressing the densities $n_{1,2}$ with the particle distances $\Delta_{1,2}$ leads to a relationship for the "normalized particle charge":

$$z \equiv \frac{Z_d \lambda_\mathrm{D}}{\langle \Delta \rangle} = \left(\frac{4\pi\epsilon_0 m_d}{6\langle \Delta \rangle^2 e^2} \frac{(c - v_1)^2 - (c - v_2)^2}{\Delta_2^{-3} - \Delta_1^{-3}} \right)^{1/2}. \tag{4.14}$$

Figure 4.11 shows the distribution of z for the well resolved particles. By fitting a robust Gaussian to the data a mean value of $\langle z \rangle = 871 \pm 87$ at a confidence level of 95% is found.

With the ion Debye length as screening length and the plasma parameters estimated above, relationship (4.14) yields $Z_d \simeq 2300$ for the particle charge, and $P_{\mathrm{H}\max} = Z_d n_2 / n_i \simeq 0.5$ for the Havnes parameter [142].

Note that the OML theory [151, 153] predicts a charge of $Z_\mathrm{d} = 2800$ ($P_\mathrm{H} = 0.5$) – 3600 ($P_\mathrm{H} = 0$). The DML theory [157], taking into account ion collisions (see Section 2.2.1), yields a charge of $Z_\mathrm{d} = 2200$, while the radial motion theory [161] predicts a charge of $Z_\mathrm{d} = 640$. Therefore, the result obtained above is well within the theoretically expected range, and the simple explanation of the wave excitation seems feasible.

Using the charge $Z_\mathrm{d} = 2300$, the strength of the total electric field acting on the particles inside the wave ridges can be estimated. From Figure 4.10, $F_{\max}/m_\mathrm{d} g \approx 2.5$ is obtained, and thus $E_{\max} = (F_{\max} - F_\mathrm{th} + m_\mathrm{d} g) / (-e Z_\mathrm{d}) \approx 22\,\mathrm{V/m}$, which is one order of magnitude smaller than the electric field in the sheath.

4.1.9 Conclusion

In this section, non-linear highly resolved wave structures, which were self-excited in a complex plasma under the action of thermophoresis, are analyzed. The method of periodgrams was applied to study the wavelength, frequency and phase velocity of the waves. Microparticle tracing allowed to investigate the propagation and magnitude of the forces acting on the microparticles.

The analysis shows that the self-excitation was due to the free energy in plasma ions drifting relative to the microparticles. This excitation mechanism also explains the observed pressure dependence of the excitation threshold.

Using a simple model of the microparticle dynamics, it was possible to estimate the grain charge, which agrees well with that calculated using known theories.

Waves were neither observed when the particles were completely suspended in the center of the chamber by the thermophoretic force nor during dedicated experiments during a parabolic flight. Microgravity conditions are, however, very well suited for the study of externally excited waves.

4.2 Waves under microgravity conditions

To investigate waves in complex plasmas under microgravity conditions, the PK-3 Plus setup on board the ISS was used[2]. The plasma chamber was filled with Neon gas at a pressure of 16 Pa with a small symmetrical gas flux. The peak-to-peak RF voltage applied to the electrodes was (45–48) V, the peak-to-peak current was (5.5–8.5) mA, and the RF power was set to 300 mW. During the active stage of the experiment, the gas cycles were stopped. After igniting the discharge, monodisperse MF particles with a diameter of (9.12±0.09) µm and a density of 1510 kg/m^3 were inserted into the plasma. The particles were illuminated from the side with a vertically extended laser sheet, the scattered light of which was recorded with a CCD camera at a frame rate of 50 Hz. (Analogous to the experiments on Earth, the direction perpendicular to the electrodes is termed *vertical*, and, correspondingly, the direction parallel to the electrodes is called *horizontal*.) A small temperature gradient between the top and bottom electrodes of $\sim$ 3 K/m was applied, pointing towards the upper electrode.

The field of view was 35.7 mm×26.0 mm, and the spatial resolution was 49.6 µm/pixel in the horizontal and 45.05 µm/pixel in the vertical direction, respectively.

In addition to the RF voltage, a variable modulation voltage with frequencies f_{mod} between 1 and 48 Hz was applied to the electrodes. The frequency bands were: (0–7) Hz with a step of 0.5 Hz, (7–21) Hz with a step of 2 Hz, and (21–48) Hz with a step of 3 Hz.

Since the particle cloud was more sensitive to the lower frequencies, and a response of the system as linear as possible was desired, the amplitude A of the modulating voltage in the range of modulation frequencies f_{mod} between 1 and 9 Hz was varied as

$$A = A_{\mathrm{max}} \cdot f_{\mathrm{mod}}/f_{\mathrm{max}}, \tag{4.15}$$

[2]This work was published in [214] with the co-authors S. K. Zhdanov, H. M. Thomas, A. V. Ivlev, M. Rubin-Zuzic, G. E. Morfill, V. I. Molotkov, A. M. Lipaev, V. E. Fortov, and T. Reiter.

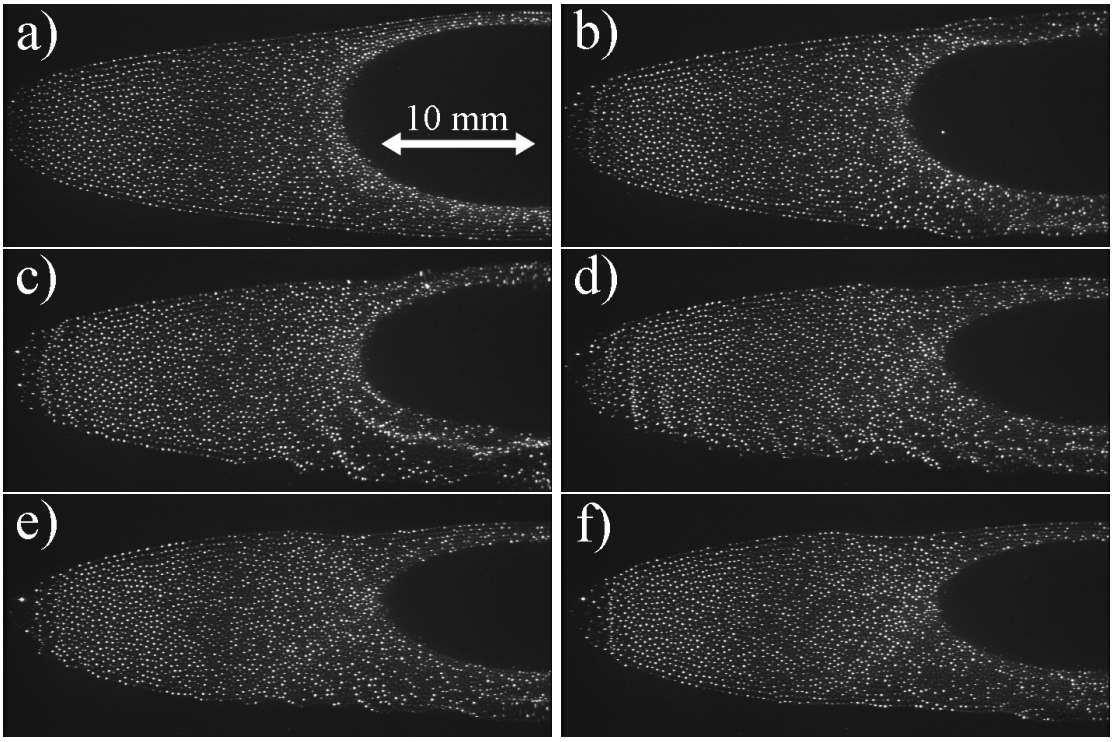

Figure 4.12: *Snap shots of the particle cloud at different modulation frequencies: a) breathing mode with weak horizontal waves (0 Hz); b) slashing mode and initial stage of vertical wave ridges (3 Hz); c), d), and e) stages of oblique waves: initial intensification and bending of the wave ridges (5 Hz), the wave activity involves all the cloud (11 Hz), and final stage with spatially separated horizontal and vertical wave fronts (15 Hz), f) high frequency mode (24 Hz). Note a local constriction of the cloud clearly seen at stages (d), (e), and (f), indicating the appearance of circulation zones.*

where $A_{\max} = 13.2\,\mathrm{V}$ and $f_{\max} = 9\,\mathrm{Hz}$. Above $f_{\mathrm{mod}} = 9\,\mathrm{Hz}$, the modulation amplitude was kept constant.

It is supposed that the variation of the excitation amplitude affects mainly the amplification of the waves rather than their dispersion. Nevertheless, it is impossible to distinguish between effects caused by the change in the modulation amplitude and those caused by the change in the modulation frequency. However, as characteristic changes also took place when the amplitude was kept constant, the effects described below are believed to be caused mainly by changing the modulation frequency. At least for $f_{\mathrm{mod}} > 9\,\mathrm{Hz}$, this assumption certainly holds.

4.2.1 Observations

Figure 4.12 shows configurations of the complex plasma at various applied external modulation frequencies, and an overview of the surveyed phases is given in Table 4.1. Without any external excitation (Figure 4.12a), the plasma was relatively stable. Almost in the center of the system, there was a void (particle free region), the size of which decreased

f_{mod} [Hz]	localization	observations
0	LEFT	weak horizontal waves, weak horizontal oscillations
	BOTTOM	no waves; weak vertical oscillations
	OBLIQUE	no waves; breathing-type oscillations
1.0–3.5	LEFT	horizontal waves, vertical oscillations at f_{mod}
	BOTTOM	vertical slashing mode at f_{mod}
	OBLIQUE	vertical slashing mode at f_{mod}
3.5–9.0	LEFT	horizontal waves, vertical oscillations with f_{mod}
	BOTTOM	vertically propagating nonlinear ridges
	OBLIQUE	nonlinear oblique waves
9.0–15.0	LEFT	nonlinear horizontal waves
	BOTTOM	nonlinear vertical waves
	OBLIQUE	nonlinear oblique waves completely connect the zones of dominantly vertical and dominantly horizontal propagation
15.0–17.0	LEFT	intense horizontal waves
	BOTTOM	intense vertical waves
	OBLIQUE	weak oblique waves accompanied by high frequency slashing
17.0–48.0	LEFT	weak horizontal waves
	BOTTOM	attenuated vertical wave-ridges
	OBLIQUE	no waves

Table 4.1: *Observed phases of the cloud dynamics for the various modulation frequencies* f_{mod}.

during the course of the experiment. The particle cloud was a little bit asymmetric: More particles were concentrated in the region below the void than above it, and the bottom part was visibly wider. This was due to the applied temperature gradient.

The cloud was weakly breathing (that is, it oscillated almost radially with respect to the geometric center) at a frequency $\simeq 5\,\mathrm{Hz}$. The bottom particles, which were closest to the lower electrode, oscillated almost vertically. There were some weak horizontal self-excited waves in the left part of the cloud, which could be observed even without any external excitation. The breathing mode might have been initiated by a weak heartbeat-type instability [74, 215], in which the void oscillates almost radially.

With an applied low frequency external excitation ($f_{\mathrm{mod}} < 3\,\mathrm{Hz}$), the cloud oscillated vertically as a whole at f_{mod} in the slashing mode (Figure 4.12b). Then, at $f_{\mathrm{mod}} > 3\,\mathrm{Hz}$, the character of the oscillations changed: Additional, vertically travelling waves appeared in the bottom part of the cloud. The horizontal waves in the left part of the cloud grew stronger. This can be seen in Figure 4.12b–d.

At $f_{\mathrm{mod}} \simeq 4.5\,\mathrm{Hz}$, the zone of actively propagating vertical waves was extended to the left and *oblique* waves started to spread inside the cloud. This behavior has not been reported before: In [79], the oblique waves appear spontaneously; in [98] the occurrence

of the oblique waves is caused by the nonuniform excitation (the modulation voltage is applied to the ring electrode only). In the experiments on the ISS reported in [91], no oblique waves are observed.

The zone of oblique waves is visible in Figure 4.12c,d. At $f_{\mathrm{mod}} = 9\,\mathrm{Hz}$, the zone between the dominantly vertical oscillations (bottom part) and the dominantly horizontal ones (left part), which were disconnected at $f_{\mathrm{mod}} < 9\,\mathrm{Hz}$, became completely occupied by the oblique excitations. It is worth to note that the external excitation was kept vertical.

Near the central part of the cloud, the oblique wave fronts were practically parallel to the void boundary, whereas in the left part of the cloud, they were parallel to the vertical cloud edge (the visible wave ridges were almost transverse with respect to the cloud). During the resonance, when the bottom and left waves ridges were connected, the angle of the oblique waves changed with the distance from the void from horizontal below the void to vertical in the left part (Figure 4.12d), making the wave pattern even more complicated. At higher modulation frequencies, no intense oblique waves were observed (Figure 4.12e,f), and the zones of wave activity were disconnected again. A movie showing the particle cloud dynamics during the experiment is available online [216].

4.2.2 Analysis techniques

Periodgrams

Three regions of the plasma cloud were analyzed thoroughly: one directly below the void (in the text below and in Table 4.1, this part is referred to as BOTTOM), one in the left corner of the particle cloud (which is called LEFT), and the region to the left of BOTTOM, where the waves were propagating obliquely (OBLIQUE). An additional region (Region 2 in Figure 4.13) was chosen for analysis to compare the wave patterns close to the void and far away from it. Figure 4.13, which is a superposition of ten images, shows the locations of these regions. Furthermore, two intense vortices are visible in the figure, one near the left edge of the cloud and one between the regions 2 and 3.

For each region, the mean distance between the particles was determined from the first peaks in the pair correlation functions obtained in the cloud without any external modulation. The particle number densities were calculated as $n_{\mathrm{d}} = (3/4\pi)\Delta^{-3}$, where Δ (the position of the first peak) is the mean interparticle separation. The results are $n_{\mathrm{d}} = (5.6{\pm}1.1) \cdot 10^9\,\mathrm{m}^{-3}$ (LEFT), $n_{\mathrm{d}} = (8.7{\pm}3.2) \cdot 10^9\,\mathrm{m}^{-3}$ (OBLIQUE), and $n_{\mathrm{d}} = (16{\pm}7) \cdot 10^9\,\mathrm{m}^{-3}$ (BOTTOM).

Periodgrams for all three regions are shown in Figure 4.14. The technique used to obtain the periodgrams was described in Section 3.3.1: The measured pixel intensities were added up for every wave position along the propagation direction. Thereafter, the resulting function was plotted for every frame. This procedure involves averaging, helping to improve statistics. Note that brighter regions in the figure correspond to higher particle number densities.

The parameters of the waves can be obtained directly from the periodgrams (Figure 4.14) by correlation analysis, as described in Section 3.3.1. Then, by measuring the slopes of the brightest strips of the periodgrams, the phase velocity of the waves was calculated.

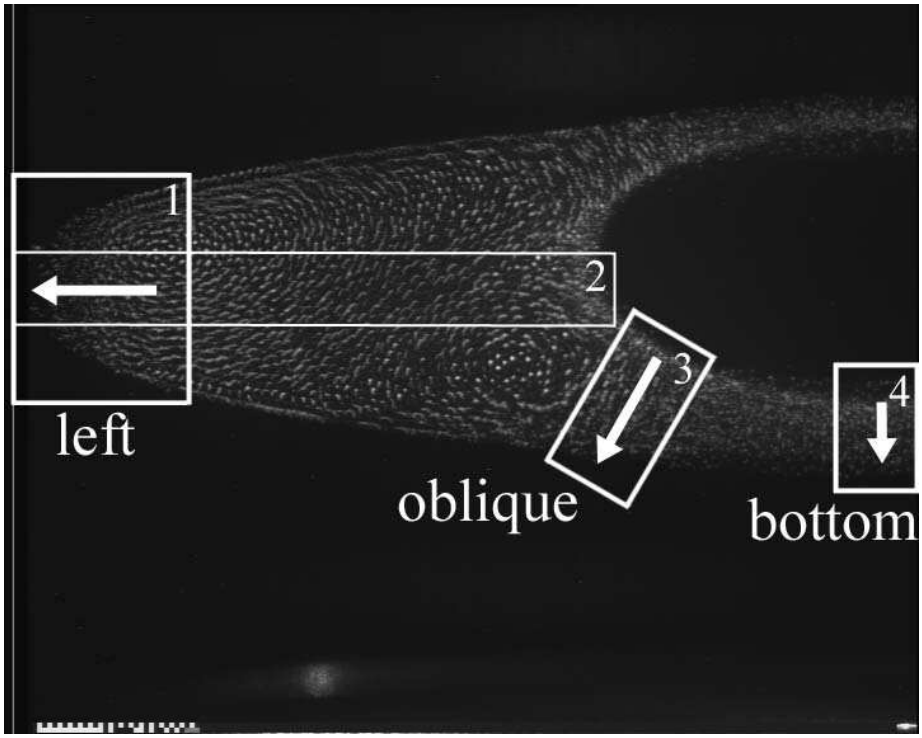

Figure 4.13: *The particle cloud is shown as a superposition of ten images displaced in time by 0.24 s to demonstrate the location of wave zones and particle circulations (time interval 13.2 s–15.36 s). The field of view is 35.7×26.0 mm². Two vortices can be clearly seen in the left part and in the bottom part of the cloud near the void. The rectangles indicate the regions used in the wave field analysis: one below the void (4,* BOTTOM*), a middle part (3,* OBLIQUE*), and an edge region (1,* LEFT*). The regions labeled 1, 3 and 4 were used to prepare Figures 4.14 and 4.17. Figure 4.15 was based on an the analysis of Region 4. Figure 4.18 shows results related to Region 3. An extended narrow stripe labeled 2 was used to prepare Figure 4.22. The arrows indicate dominant directions of observed wave propagation.*

The periodgrams for all three regions shown in Figure 4.14 reveal all dynamical stages qualitatively described above. For instance, the motion of the bottom-most rows oscillating even without external excitation is represented at the top left part of Figure 4.14(1a), while horizontal waves in the LEFT region were observable as brighter stripes with distinct slopes in the same frequency domain (Figure 4.14(1b)). In Figure 4.14(1c) some new structures appear when the external modulation was started. This is due to the vertical component of the particle displacement captured in the oblique cut (OBLIQUE region 3, Figure 4.13). "True" oblique waves started later on at $t > 45$ s and become more pronounced at $t > 60$ s (t is the time counted from the start of the experiment and shown in Figure 4.14).

Oscillations of the whole cloud in the domains with a low excitation frequency ($f_{\mathrm{mod}} =$ (1–2) Hz, $t < 28$ s) are well visible in Figure 4.14(1a, 1c). The horizontal waves shown in Figure 4.14(1b, 2b, 3b) (observed in the LEFT region, Figure 4.13) did not change periods and slopes for a long time in contrast to the vertical oscillations shown in Figure 4.14(1a,

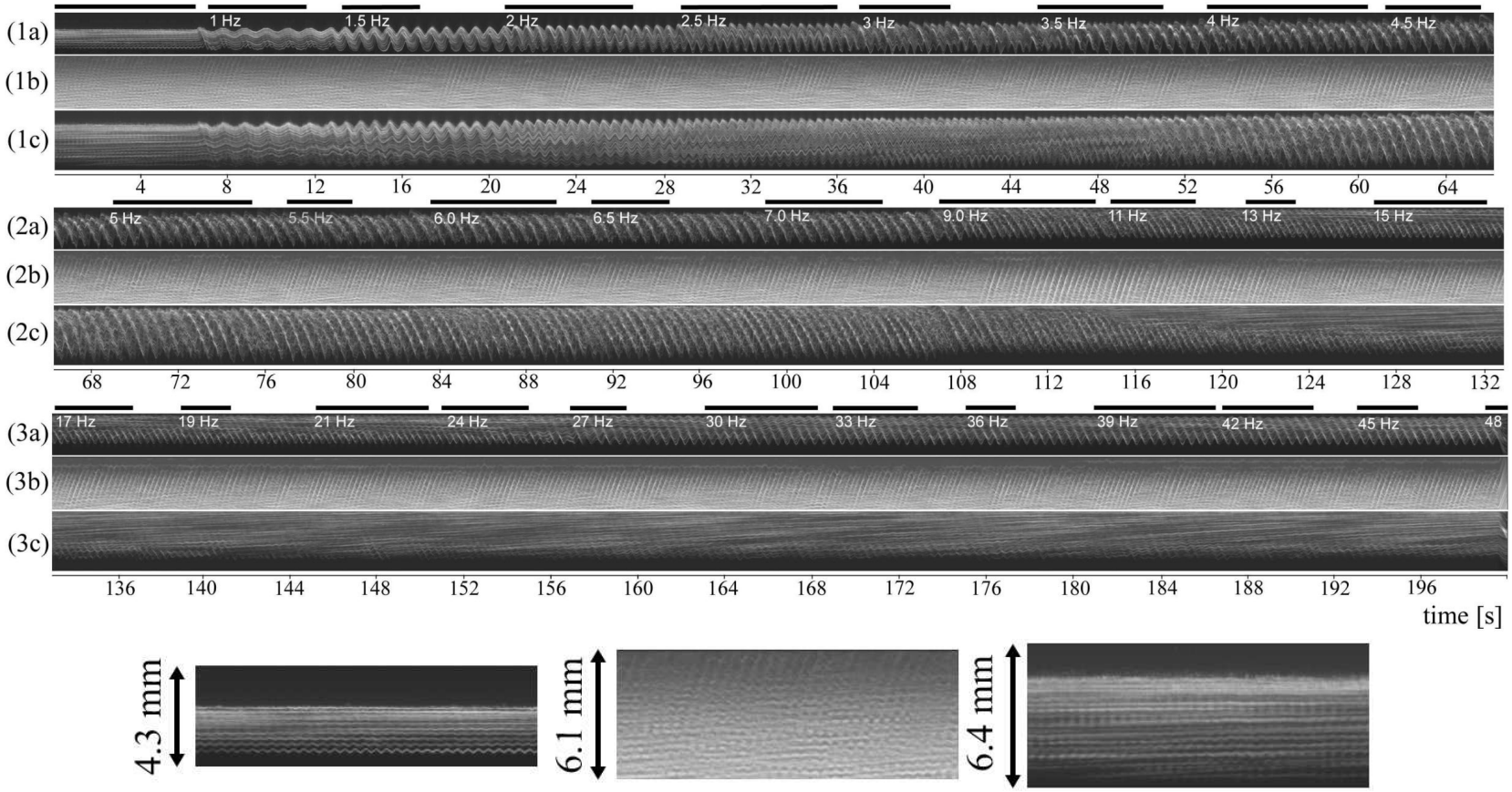

Figure 4.14: *Top: Periodgrams of vertical (a), horizontal (b) and oblique (c) waves observed during the experiment in the* BOTTOM, LEFT *and* OBLIQUE *region, respectively. For the sake of convenience the investigated frequency band is divided into three parts: (1) (0–4.5) Hz, (2) (5–15) Hz, and (3) (17–48) Hz. The rulers at the sub-band bottoms show the time counted from the start of the experiment. The regions marked in bold atop the band indicate the parts which were analyzed. Bottom: Enlarged* BOTTOM, LEFT *and* OBLIQUE *regions (initial phase without external excitation, $t \leq 7s$). The spatial scales shown on the bottom are the same for (1a)–(3a), (1b)–(3b) and (1c)–(3c), respectively.*

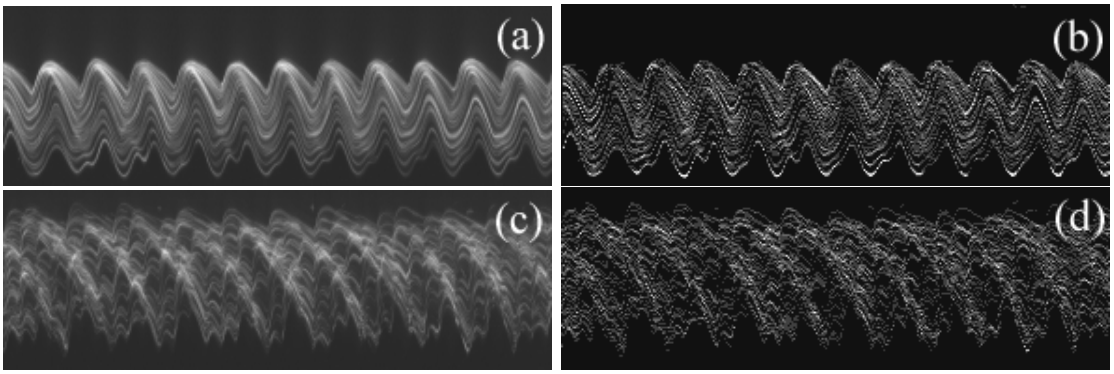

Figure 4.15: *Periodgrams of the vertical slashing mode ((a), (b): $f_{\mathrm{mod}} = 2\,Hz$), and of the nonlinear wave-ridges ((c), (d): $f_{\mathrm{mod}} = 6\,Hz$) revealed by pixel intensities ((a), (c)) and by particle trajectories ((b), (d)). The black regions on the top correspond to the void location. FoV: $4.3\,mm \times 5.9\,s$.*

2a,3a), the frequency of which varied with time.

At higher frequencies, the oblique waves disappeared (starting in the end of Figure 4.14(2c), $t \geq 116\,\mathrm{s}$), and the vertical waves occupied only the narrow stripe of the cloud (Figure 4.14(3a)), whereas the horizontal waves are clearly seen in Figure 4.14(3b), still with approximately the same constant period.

Particle tracks

Another way to determine the oscillation periods is to analyze the particle tracks. The particle positions were determined in the standard way as described in Section 3.3.2. The uncertainty in the particle positions was estimated as $\pm 5\,\mu\mathrm{m}$. Examples of periodgrams calculated by using the traced particle positions and those calculated with the help of the pixel intensities are shown in Figure 4.15. The positions of wave ridges indicated by both methods agree well with each other.

For the edge regions 1 (LEFT) and 2 in Figure 4.13, it was possible to compare results of measurements obtained by using periodgrams with those calculated by Fast Fourier Transforms (FFTs) of the particle velocities. In doing so, first the velocities for every particle track were calculated, and then the mean values were subtracted. In order to reduce the influence of sequence edge effects, a Hann window was applied[3], and finally the result was Fourier-transformed. Then the most intense peaks were identified and the corresponding frequencies were determined.

Using FFTs was only feasible for these two regions because there particle tracks were long enough to guarantee a sufficient peak resolution. The method of using FFTs has the advantage that several peaks in the frequency spectrum can be detected simultaneously (see, e.g., Figure 4.16 below).

[3]The Hann function is defined as $w(x) = 1/2\,(1 - \cos(2\pi x/N))$, where N is the number of collected samples of the signal. Before the signal is Fourier-transformed, it is multiplied by $w(x)$. This mitigates "spectral leakage" caused by the finiteness of the time sampling interval [217].

4.2.3 Measurement accuracy

For the proposed routines of measurements, there are several possible sources of errors: pixel noise[4], pixel locking, and poor statistics (see Section 3.4 for a more detailed elaboration on the error treatment). Here, the maximal error in the particle positions caused by pixel noise was measured to be of the order of 0.1 pixels. The uncertainty of velocities from the spread in positions was estimated as 0.35 mm/s, and that in forces as $1.5 \cdot 10^{-14}$ N, where the error induced by the uncertainty of the mass of the microparticles was neglected, as it is an order of magnitude smaller.

In the plots displayed in this section, the errors shown are the standard errors from obtaining the mean. For instance, the oscillation frequencies usually were determined with an uncertainty $\leq 10\%$.

4.2.4 Wave parameters

The spectrum of the waves and oscillations surveyed in the present experiments was very rich. It was expected to register DAWs (or DDWs) because these waves were observed in a number of previous studies. It was also anticipated to detect the slashing mode, since the particles were driven to shake vertically with the applied periodic modulation.

Even at first sight at the periodgrams shown in Figure 4.14, it is clear that the situation was much more complicated. At once, it is possible to distinguish the global modes (breathing and slashing modes, Figure 4.14(1a)) and the local modes. The latter were the 'sound-like' nonlinear modes (Figure 4.14(1c, 2c)), the spatial and temporal periods of which decreased with the modulation frequency. Moreover, there was a mode excited in the left part of the cloud, which was practically independent of perturbations (Figure 4.14(1b, 2b, 3b)) and had a constant period.

Figure 4.16a shows a periodgram obtained from average horizontal particle velocities without external modulation. The particle velocity field was binned in the horizontal direction (bin size 0.06 mm). The analyzed region corresponds to the LEFT Region 1 in Figure 4.13, but is a bit narrower and extended approximately twice towards the cloud center to enlarge the analyzed field of global oscillations. The propagating waves are clearly visible as inclined lines at $0 \leq x \leq 4$ mm. The vertical black (negative v_x) and white (positive v_x) lines indicate the global oscillation of the whole cloud without propagation.

Figure 4.16b shows the logarithm of the intensities of the corresponding Fourier spectrum (the FFT technique applied is described above, see Section 4.2.2). The fundamental frequency of the horizontal global oscillation, which was $f_1 = (5.3 \pm 0.2)$ Hz, and its second harmonic ($f_2 = (10.6 \pm 0.2)$ Hz) cover the whole analyzed space. The frequencies of the propagating waves near the left edge of the cloud (small x values) are visible as bright red spot in the corresponding region. They were smaller than the frequency of the global oscillation.

Figure 4.17 shows the oscillation frequencies which were determined with the three different analysis methods: (a) periodgrams, (b) direct analysis of particle tracks, and

[4]Pixel noise is caused by random fluctuations of the brightness of each pixel induced by noise in the sensor of the camera and the electronics. See Section 3.4.

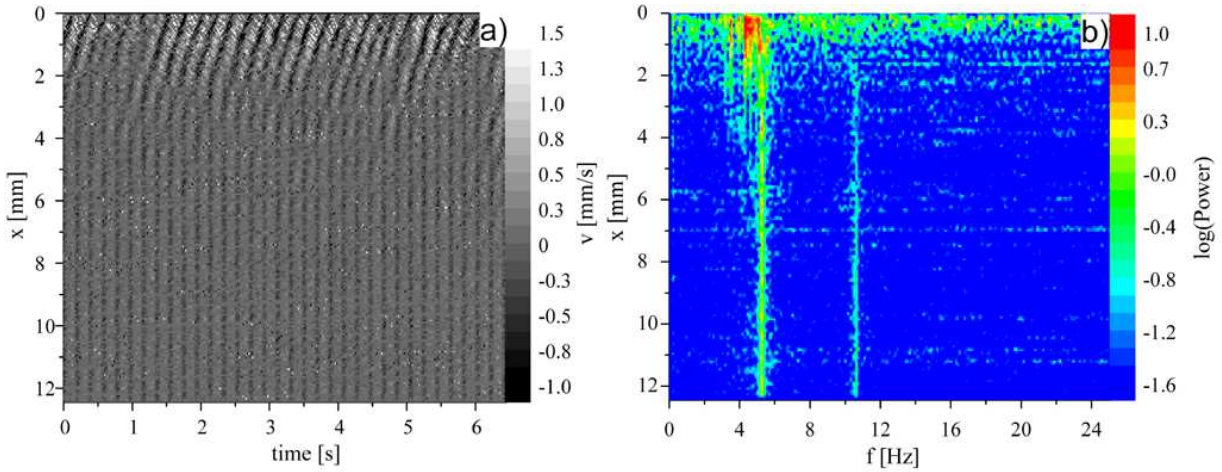

Figure 4.16: *(a) Periodgram of the average horizontal particle velocities in an extended left region (12.4×2.7 mm²). To enhance the contrast a gray-scale in the interval (−1.0 to 1.5) mm/s was used; all values $v \geq 1.5$ mm/s are shown in white, whereas all $v \leq -1.0$ mm/s are shown in black. The wave propagation in the region $x \leq 4$ mm and global oscillations of the cloud are clearly seen. (b) Fourier spectrum of individual bins in the same region. The first (fundamental) harmonic $f_1 = (5.3 \pm 0.2)$ Hz and the second superharmonic $f_2 = (10.6 \pm 0.2)$ Hz are clearly seen. The color indicates the logarithm of the intensity of the spectrum in arbitrary units, where values* $\log(\text{Power}) \geq 1.0$ *are shown in red and values* $\log(\text{Power}) \leq -1.6$ *are shown in blue.*

(c) FFTs of particle tracks. With the help of the FFTs, several peaks of the modulation frequency were detectable. Fourier spectra show the harmonics of the primary frequency and make it possible to simultaneously detect the modulation frequency and the wave frequency in a wide range of modulations.

The results of the three methods show a fairly good agreement. Only in the frequency interval $5\,\text{Hz} \leq f_{\text{mod}} \leq 8\,\text{Hz}$, the frequencies of the particles oscillating vertically determined by analysis of the particle tracks were a little higher than those obtained from periodgrams. This may be due to some systematic measurement errors arising from the peak picking procedure during the analysis of the particle tracks.

The frequency of the **horizontal waves** (left edge of the cloud) remained almost constant at a level of 4.5 Hz, independently of the applied modulation.

Initially in the oblique and bottom parts of the cloud (Figure 4.13) there were no propagating waves, only oscillations were present. The frequencies of these oscillations f_{os} were equal to the modulation frequency. This corresponds to the **vertical slashing mode**.

The **vertically propagating wave-ridges** started up with the oscillation frequency 2 Hz at $f_{\text{mod}} = 3\,\text{Hz}$. Their frequency gradually grew up to approximately 3.5 Hz while the modulation frequency increased up to $f_{\text{mod}} = 10\,\text{Hz}$. Then the wave frequency varied only slowly up to $f_{\text{mod}} \approx 25\,\text{Hz}$, where it dropped down to 3 Hz. At $f_{\text{mod}} > 25\,\text{Hz}$, it remained almost constant. Unfortunately, there was not enough resolution in the data to study this 'frequency drop' in more details.

For the **oblique waves**, the situation was similar. The only difference was that they

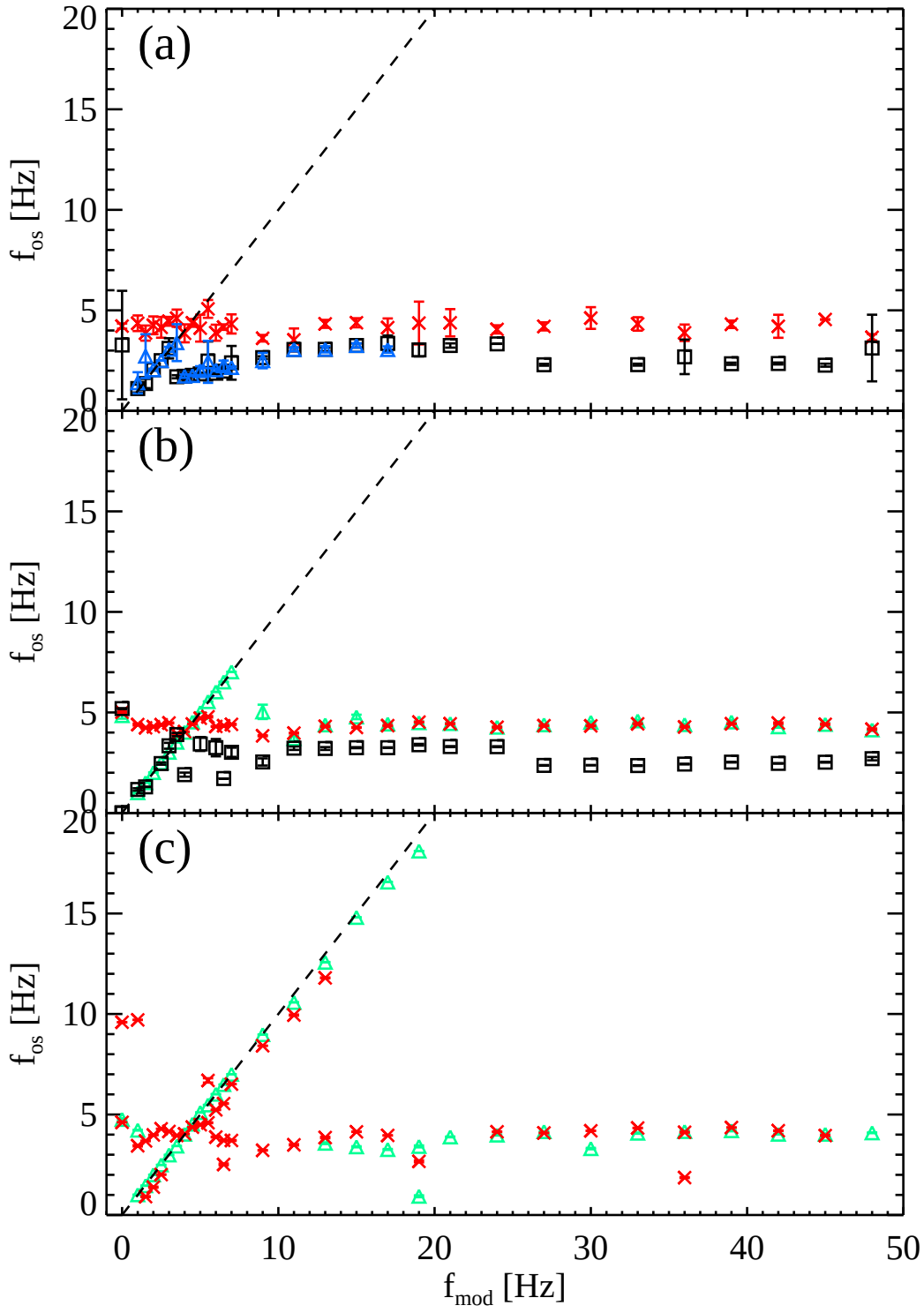

Figure 4.17: *(a) Oscillation frequencies vs. modulation frequency for the* LEFT *(red crosses),* BOTTOM *(black squares), and* OBLIQUE *(blue triangles) regions obtained by using the pixel periodgrams shown in Figure 4.14. (b) Oscillation frequencies obtained by analyzing the particle tracks directly (red crosses:* LEFT *region, horizontal movement; green triangles:* LEFT *region, vertical movement; black squares:* BOTTOM *region, vertical movement). (c) Frequencies determined with FFTs of the particle tracks (red crosses:* LEFT *region, horizontal movement, green triangles:* LEFT *region, vertical movements). The dashed lines indicate points of equal frequencies* $f_{os} = f_{mod}$.

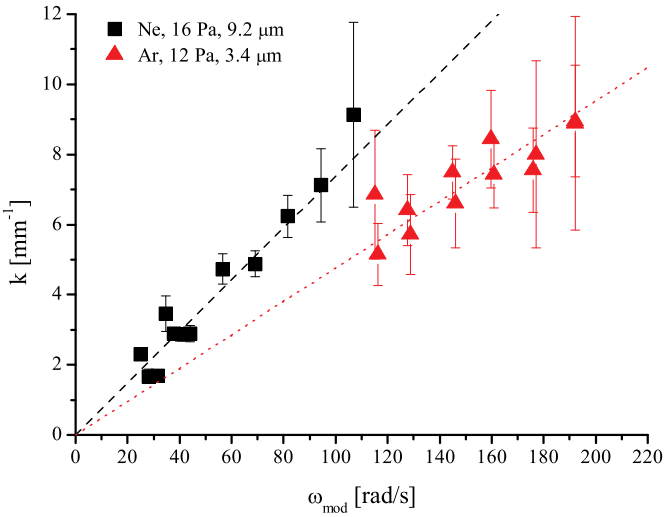

Figure 4.18: *Wave number measured in the oblique region (Figure 4.13 Region 3) using the periodgram as a function of the angular modulation frequency (black squares). The fit (black dashed line) is a least-squares fit running through zero ($\omega/k = 14$ mm/s). For reference, the data measured in [98] (red triangles) and a line corresponding to the mean of the slopes given in [98] ($\omega/k = 21$ mm/s) (red dotted line) are also shown.*

were never observed at modulation frequencies higher than 20 Hz.

The wave spectrum analysis provides information about the particle dynamics. For instance, to obtain a rough estimate of the particle charge, it is possible to assume that the horizontal waves in the left region oscillated locally at the dust plasma frequency

$$\omega_{\mathrm{pd}} = 2\pi f_{\mathrm{pd}} = \sqrt{\frac{Z_{\mathrm{d}}^2 e^2 n_{\mathrm{d}}}{m_{\mathrm{d}} \epsilon_0}}, \tag{4.16}$$

where m_{d} is the mass, $Z_{\mathrm{d}}e$ denotes the absolute value of the charge, and n_{d} represents the number density of the microparticles. Assuming $f_{\mathrm{pd}} = 5$ Hz, $m_{\mathrm{d}} = 6.2 \cdot 10^{-13}$ kg, and $n_{\mathrm{d}} = 5.6 \cdot 10^{9}\,\mathrm{m}^{-3}$ (density determined above for the LEFT region, see 4.2.2), Equation (4.16) yields $Z_{\mathrm{d}} \approx 6200$. This estimate is well inside the range predicted by the DML theory [157] ($Z_{\mathrm{d}} = 4800$–7900) for $T_{\mathrm{e}} = 4$ eV and $n_{\mathrm{e}} = (1\text{–}3) \cdot 10^{13}\,\mathrm{m}^{-3}$. For comparison, the radial motion theory [159, 161] results in a charge of $Z_{\mathrm{d}} \approx 1300$, whereas the OML theory [151, 153] yields $Z_{\mathrm{d}} \approx 14\,000$ for the same set of parameters.

Using $n_{\mathrm{i}} = 4 \cdot 10^{13}\,\mathrm{m}^{-3}$ and $T_{\mathrm{i}} = 300$ K as well as $f_{\mathrm{d}} = 5$ Hz yields a dust acoustic wave speed of $c_{\mathrm{DAW}} = \lambda_{\mathrm{D}} \cdot \omega_{\mathrm{pd}} = 5.9$ mm/s.

Velocities and spatial periods

The velocity of the **vertical waves** (Region 4, BOTTOM) was $\simeq 4$ mm/s as determined from the periodgrams. Only in the interval 3 Hz $\leq f_{\mathrm{mod}} \leq$ 5 Hz and for $f_{\mathrm{mod}} >$ 25 Hz, the velocity of the wave ridges was a bit higher, $v \simeq 5$ mm/s. The mean value and its standard error were (4.4±0.4) mm/s. The velocity of the **oblique waves** varied from (7 to 3) mm/s with an average value of (5.8±0.8) mm/s. The velocities of the **horizontal waves** in the LEFT region were (6.5–7) mm/s with an average of (6.8±0.1) mm/s. The wavelengths of these waves were around (1–2) mm almost for all modulation frequencies.

Oblique quasi-sound wave

The wavelength of the waves propagating in Region 3 (OBLIQUE) visibly varied with the modulation frequency. Hence, it was possible to study the dispersion relation of these

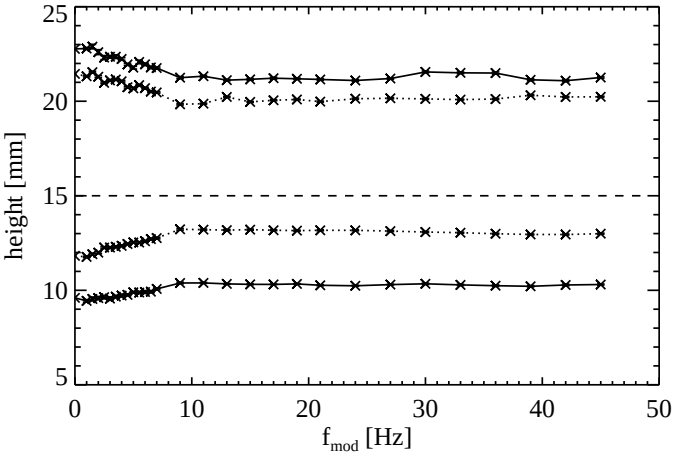

Figure 4.19: *Averaged positions of the vertical cloud edges vs. modulation frequency. Solid lines: outer edges, dotted lines: inner edges (void boundary), dashed line: center of the chamber. Note especially a 15 % compression of the cloud in the oscillatory field, which was caused by the change of the modulation amplitude according to Equation (4.15).*

waves. Figure 4.18 shows that it was a quasi-sound-like type with a slope corresponding to the wave speed of (14±3) mm/s. These waves can thus be called **oblique quasi-sound waves (OQSWs)**. The data obtained by Annibaldi et al. [98] is shown in the same Figure 4.18 for comparison (red triangles). For reference, a line corresponding to the velocity of 21 mm/s is also plotted, which is the arithmetic mean of the velocities given in [98].

Note that Figure 4.18 shows the k vs. ω_{mod} dependence rather than k vs. ω_{wave}, as has been previously recommended in a number of publications [80, 91, 98]. A priori, the wave frequency is not identical with the modulation frequency. Plotting the wave numbers as a function of the measured wave frequencies also results in a rising dependency $\omega = \omega(k)$. Fitting a linear regression line running through zero to this data yields a wave velocity of (3.5±0.4) mm/s, which is closer to the mean value measured using the periodgrams (see Section 4.2.4) than the value resulting from using the modulation frequencies. The difference between this value and the mean of the velocities given by the slopes in the periodgram might be partly due to particles drifting from the cloud center towards the edge, i.e., to the left. This drift results in a bending of the wave ridges. Furthermore, the waves were already nonlinear, with a compression factor $(n - \langle n \rangle)/\langle n \rangle \simeq 0.96$, so that they did not necessarily travel at the speed of sound.

4.2.5 Particle dynamics

Movement of the cloud and the void

The boundaries of the particle cloud were determined by plotting contours of the smoothed pixel brightness in every image. The result is shown in Figure 4.19. As is clearly seen in the figure, both the cloud size and the size of the void decreased monotonically as the modulation frequency increased in the range $0 < f_{\mathrm{mod}} \leq 9\,\mathrm{Hz}$. This was caused by a change in the amplitude of the modulation as given by Equation (4.15). At $f_{\mathrm{mod}} \geq 9\,\mathrm{Hz}$, the global cloud geometry stayed about the same. Without external modulation, the cloud width was 13 mm, it was then compressed up to 11 mm. The void was compressed more than the whole cloud. In the beginning the width of the void was 75% of that of the cloud.

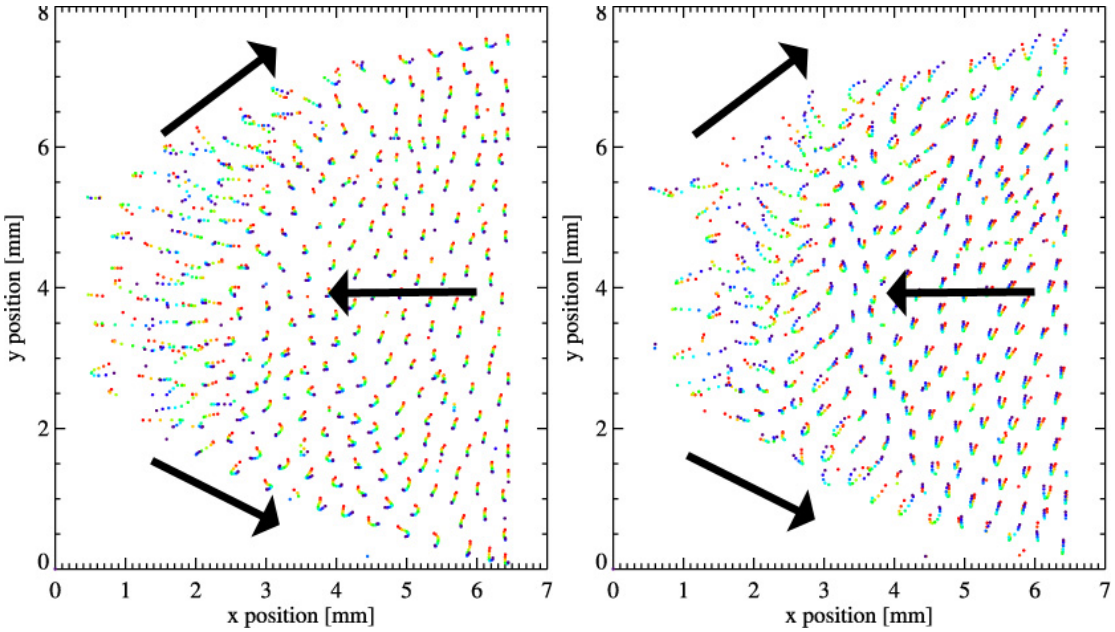

Figure 4.20: *Particle vibrations and transport at the cloud edges. Shown are two panels ((a) $f_{\mathrm{mod}} = 2\,\mathrm{Hz}$, (b) $f_{\mathrm{mod}} = 4\,\mathrm{Hz}$), each of them consists of ten superimposed consecutive images, which are color-coded (the color varies from red to purple). The enhanced particle oscillations at the periphery appear as long bent multicolored lines. This demonstrates that these particles were moving faster compared with particles in the bulk during the observation time of 200 ms. There also were noticeable clockwise/counterclockwise (top/bottom) circulations (indicated by arrows). The circulation accelerated at higher modulation frequencies.*

At $f_{\mathrm{mod}} \geq 10\,\mathrm{Hz}$, it was less, (60–65) % on average.

At the lower excitation frequencies, particle oscillations are clearly distinguishable at the outer edges of the cloud. The void boundary also oscillated approximately with the same frequency and phase (not shown in the figure), but with a much smaller amplitude. This is typical for the breathing mode. At the higher excitation frequencies, the amplitude of the void boundary oscillation decreased faster than that of the cloud edges.

Individual particle tracks

The particle behavior was comparatively simple under the given conditions. When the wavefront approached a particle, it was captured by the wavefront and moved within it for some short time. Then, the particle left the wavefront, trying to relax to its original quasi-equilibrium position. When the new wavefront arrived, this cycle started over again. This procedure was similar to that described for the self-excited waves in Section 4.1. The periodic or quasi-periodic motion was combined with vertical oscillations forced by the external modulation.

Figure 4.20 depicts superimposed particle positions in ten consecutive frames at the left edge of the cloud at modulation frequencies of 2 and 4 Hz. In both cases, the tracks near the border of the cloud elongated. This means that in both cases the particles accelerated

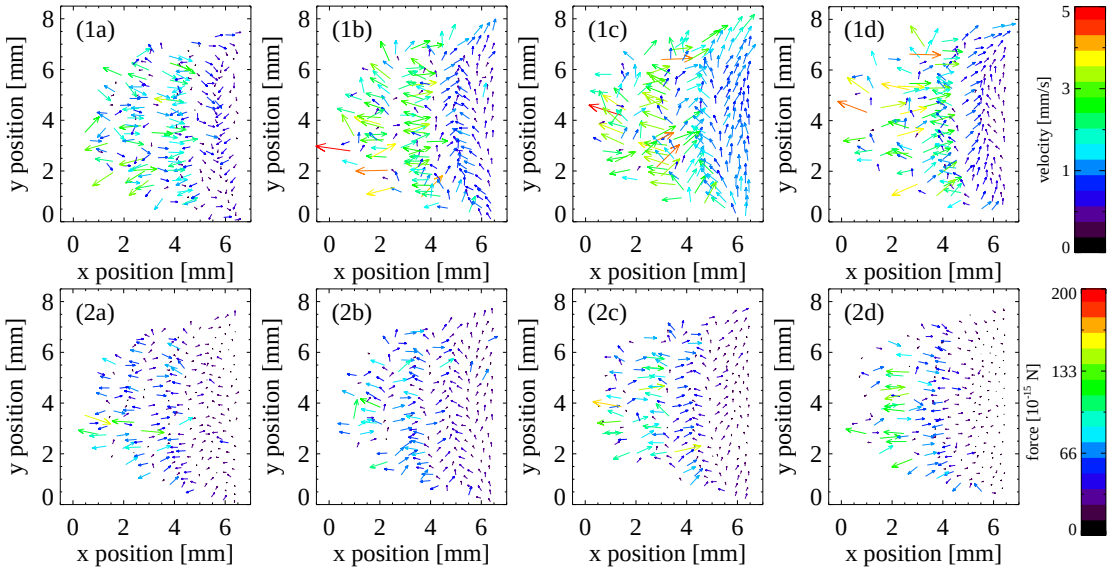

Figure 4.21: *(1) Vector maps of particle velocities (uncertainty ±0.35 mm/s) and (2) force fields (uncertainty $\pm 15 \cdot 10^{-15}$ N) at the cloud periphery for four different instants of time: (a) t = 23.50 s, (b) t = 23.58 s, (c) t = 23.66 s, and (d) t = 23.74 s. The modulation frequency was 2 Hz (compare Figure 4.14). The nonlinear waves form visible multi-ridge patterns. The additional color-coding helps to reveal the variation of the magnitude of the forces and velocities with position.*

towards the edge.

In the bulk of the cloud, the particles generally tended to move to the left, that is, from the void outwards to the edge. Inside a narrow surface layer, there was an opposite trend: The particles moved upwards to the right and downwards to the right (hence, in the direction of the void), which is also clearly visible in Figure 4.20. This shows that a "circulation dynamo" worked in the cloud (as in [183], but more complicated in nature): The top part rotated clockwise, whereas the bottom part rotated anticlockwise.

From the particle tracks, the velocities were calculated[5]. An example is shown in Figure 4.21. The propagation of the particles in wavefronts is clearly visible. The magnitude of the velocity increased closer to the cloud edge. The sequence shown in Figure 4.21 covers approximately half a period of the vertical oscillation, which is also visible in the vertical orientation of the vectors.

Forces acting on the particles

The microparticles were traced, and their velocities $\boldsymbol{v}_\mathrm{d}$ and accelerations $\boldsymbol{a}_\mathrm{d}$ were determined from the consecutive frames. The net force $\boldsymbol{F}_\mathbf{net}$ acting on the particles was calculated using Newton's second law:

$$\boldsymbol{F}_\mathbf{Ep} + \boldsymbol{F}_\mathbf{net} = m_\mathrm{d}\boldsymbol{a}_\mathbf{d}, \tag{4.17}$$

where $\boldsymbol{F}_\mathbf{Ep}$ is the Epstein drag force [166], see Equation (2.39).

[5]Using second order extrapolation for the first and last point of the tracks.

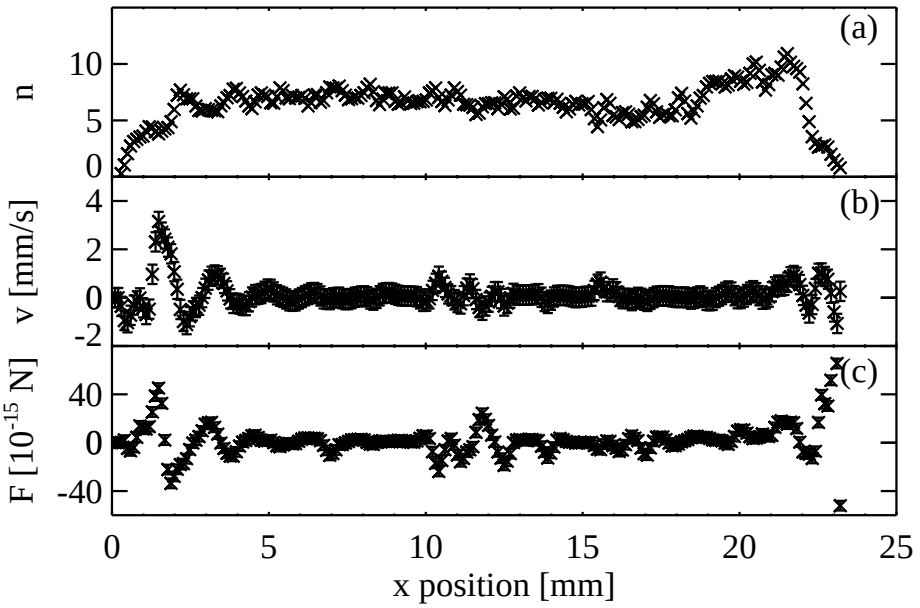

Figure 4.22: *(a) Number n of particles in the slab, (b) mean particle velocity v and (c) mean force F acting on the particles as a function of the horizontal position. The data points were calculated for a window of size 2.7×0.3 mm² along a central region extending from the left cloud edge to the void (Region (2) in Figure 4.13). In the plot, data from five frames in the same phase is superimposed, assuming a wave frequency of 4.2 Hz. The plots were smoothed over a width of 250 µm. The voltage modulation frequency was 2 Hz.*

Figure 4.21 illustrates the forces acting on the particles in the left part of the cloud as vector maps. Note the displacement of the position of strong forces compared with that of high velocities.

The force was of the order of $(10^{-13}$–$10^{-14})$ N, which is one-tenth to one-hundredth of the strength that gravity would have on the microparticles on Earth. The periodic rise and fall corresponding to the waves and the relaxation towards the original position of the particles is clearly visible.

Figure 4.22 shows the mean densities, mean velocities and mean forces acting on microparticles in a slab extending from the left edge of the cloud to the void in one phase of the horizontal waves as function of the horizontal position. As in Figure 4.21, the peak in velocity is displaced compared with the peak in force, so that first the forces acted on the particles, which were as a result accelerated to their highest velocities. There is also a shift between the peaks in number density and forces. A similar shift has already been mentioned when the self-excited waves were discussed in the previous Section 4.1 (Figure 4.10).

Closer to the void, the forces were stronger than inside the bulk of the complex plasma. The variation in particle density inside the wave ridges is also visible.

4.2.6 Conclusion

In this section, dust density waves externally excited in a complex plasma under microgravity conditions on board the ISS were investigated. In addition to the vertical oscillation with the externally imposed frequency, waves propagated both in the vertical and horizontal direction. The frequency of the horizontal oscillation did not depend on the external modulation frequency. In fact, the horizontal waves were present even without any external modulation. The frequency of the vertical waves showed some dependence on the modulation frequency.

When the modulation frequency was resonant with that of the horizontal oscillation, the excitation region of the vertically propagating waves started spreading towards the left part of the cloud. At $4.5 \leq f_{\mathrm{mod}} \leq 17\,\mathrm{Hz}$, obliquely propagating waves were observed. Their wave number depended on their frequency, resulting in a quasi-sound like dispersion relation. Around a modulation frequency of 9 Hz, the wave activity spread over the whole cloud. At higher frequencies, the oblique waves disappeared again.

Additionally, the particles were traced individually, which made it possible to determine the velocities and net forces acting on them. The microparticle dynamics were similar to those accompanying the self-excited waves observed in the ground setup and described in Chapter 4.1. Without external excitation, only the weak horizontal waves at the horizontal edge of the microparticle cloud existed. The same was true for the complex plasma in the ground setup: As the thermophoretic force compensated for gravity, the self-excited waves did not to occur. However, under these conditions, a novel feature of complex plasmas was revealed: The ability to form bubbles, blobs, and cusps. These phenomena are discussed in the following section.

4.3 Microparticle bubbles, blobs, and surface cusps

The formation of bubbles, blobs, and surface cusps was investigated[6] using the ground PK-3 Plus laboratory under gravity conditions with micrometer-sized MF particles with diameters between 3.4 and 7.2 µm. The scattered laser light was recorded with the high speed camera at a maximal frame rate of 1000 fps, and a temperature gradient was maintained between the two ground plates of the chamber to lift the particle cloud into the bulk of the plasma.

4.3.1 Observations

When gravity was approximately compensated by the thermophoretic force, and hence an "artificial" microgravity was achieved, some phenomena that occur in complex plasmas under microgravity were observed. The particles occupied the bulk of the plasma, and a void in the center of the chamber was formed, caused by the imbalance of ion drag and electrostatic forces acting on the microparticles [74]. In addition, microparticle vortex motions occurred in the off-axis region of the plasma chamber [183]. A further increase of

[6] The main results discussed in this section are published in [136] with the co-authors M. Rubin-Zuzic, S. Zhdanov, A. Ivlev, H. M. Thomas and G. E. Morfill.

the temperature gradient usually caused the microparticles to flow around the void to the top of the chamber (gravity was overcompensated).

Under certain discharge conditions, when the RF power was low and the pressure was high, so that the plasma was close to turning off, the microparticle fluid started to show remarkable behavior. First, the void boundary became unstable, with microparticles moving through the void region from the bottom to the top. Similar behavior has also been observed under microgravity conditions on board the ISS in the PKE-Nefedov and PK-3 Plus setups. An example is depicted in Figure 4.23, which shows an experiment in the PK-3 Plus setup on the ISS at low powers. Asymmetry was induced in the plasma chamber by applying a DC electric field in addition to the RF field. The particles were moving through the void in the direction towards the bottom of the picture, that is towards the negative applied potential. They flowed back upwards around the void on the side.

In the ground experiments, the experimental conditions at which the instability was observed were: power of the RF generator (45–55) mW, peak-to-peak voltage on the electrodes (28–34) V, pressure between 18 and 45 Pa depending on the particle size and number density. It was possible to change the regime of the instability towards the short-scale mode, for instance by injecting more particles, or by decreasing the RF power. Then, indentations and cusps on the surface of the microparticle cloud below the void became visible. The step-by-step development of the instability can be seen in Figure 4.24. There, the activity was caused by increasing the temperature difference between the ground plates. First, the system was stable (Figure 4.24a). While the temperature difference was increased, the indentations on the void became more pronounced and particles started to move through the void (Figure 4.24b–e). This indicates that the cloud was already in the critical condition. Later on, bubbles, cusps, and blobs appeared (Figure 4.24e,f).

The particle number density below the void was enhanced compared with the rest of the cloud. Estimates show that the electron density can be strongly depleted because the

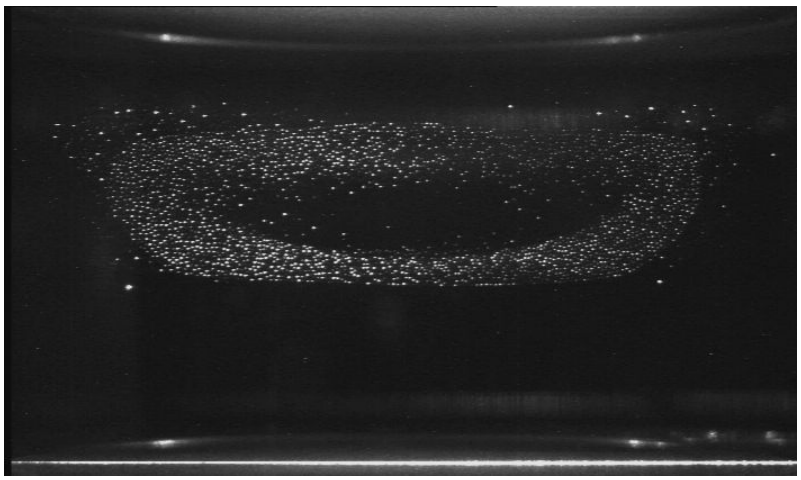

Figure 4.23: *Particles moving downwards through the void in the PK-3 Plus setup on board the ISS. A DC electric field applied to the electrodes induced asymmetry in the plasma chamber. FoV: 58.6 mm×43.1 mm.*

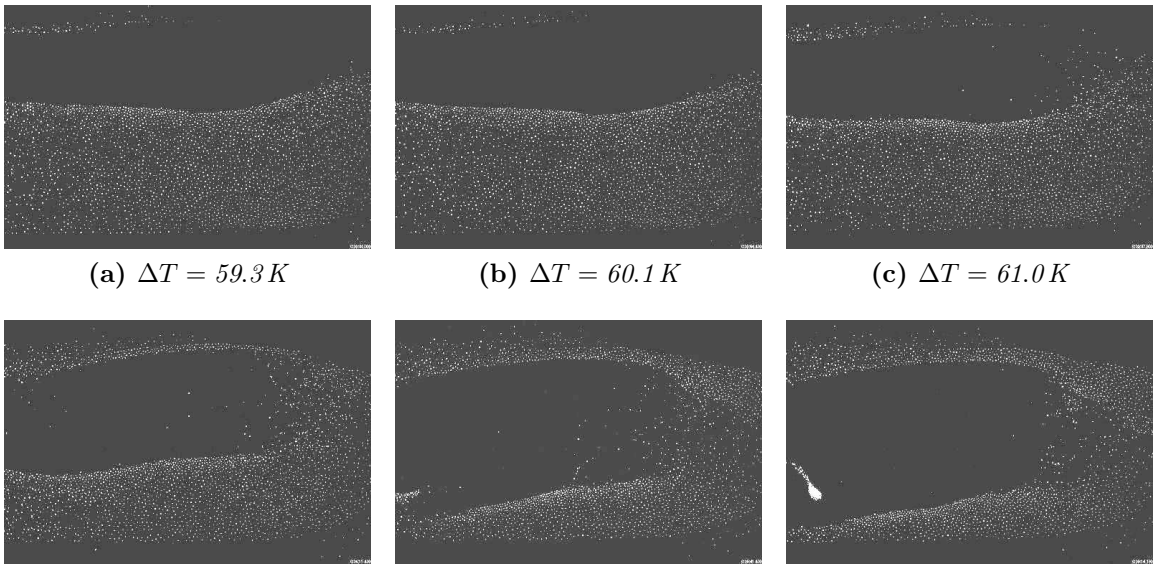

(a) $\Delta T = 59.3\,K$ **(b)** $\Delta T = 60.1\,K$ **(c)** $\Delta T = 61.0\,K$

(d) $\Delta T = 61.9\,K$ **(e)** $\Delta T = 62.8\,K$ **(f)** $\Delta T = 63.7\,K$

Figure 4.24: *Beginning stage of the instability in an Argon plasma at a gas pressure of 27.4 Pa with 6.8 µm particles. Field of view: 28×19 mm^2. The first bubble is visible at $\Delta T = 62.8\,K$ (Figure (e)).*

Havnes parameter P_{H}, see Equation (2.15), can substantially exceed unity. This might be considered an inherent feature of the instability. Figure 4.25 shows several examples of the observed fluid activity.

Unstable **bubbles** (Figure 4.25c,top) appeared in the microparticle fluid beneath the void as small empty regions within the microparticle cloud. They moved upwards, forming blisters and pushing entire layers of microparticles (the *lid*) into the void until the blister lid broke up. Frequently, the pressure inside the bubble was so strong that the ejection of the particles into the void was explosion-like (Figure 4.25top).

Under the same conditions, **blobs** appeared, which are self-contained particle droplets (Figure 4.25a), moving within the void. **Cusps** are strongly pointed tips formed in the surface of the microparticle cloud below the void, pointing upwards. Often, a spray of particles was emitted from the cusp into the void (Figure 4.25b). These sprays sometimes were also emitted from blobs. A movie showing all these phenomena is available online [136].

The instability occurred in a variety of experimental conditions (particles with diameters from (4.8 to 7.2) µm, Argon and Neon plasmas), but its increment depended strongly on the RF power, temperature gradient, pressure and particle number density. The instable phase could be switched on and off by changing any of these parameters. (The instability appeared when the RF power was lowered or the temperature gradient, pressure, or particle number density was increased.) It was not possible to initiate the instability with particles of small diameter, 3.4 µm or less.

The bubbles were always formed below the chamber center. The vertical height at which

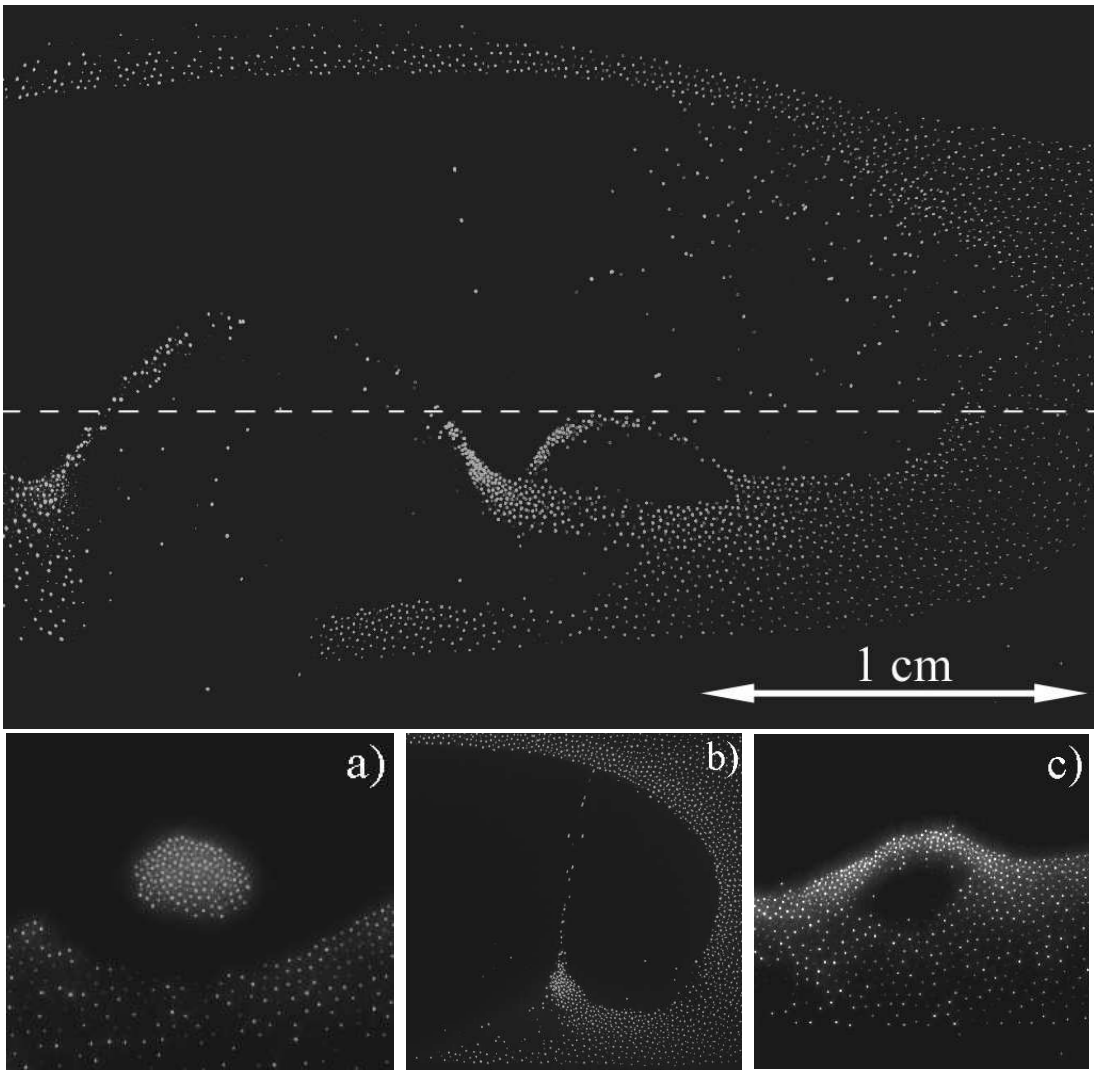

Figure 4.25: *Observed fluid activity in a complex plasma. Top: Two microparticle bubbles (6.81 µm particles, $\Delta T = 65\,K$, Argon plasma). The dashed line indicates the midplane of the plasma chamber. Bottom: a) Microparticle blob [field of view (FoV) $8\times7\,mm^2$, 6.8 µm particles]. b) Microparticle spray (FoV $11\times11\,mm^2$, 4.8 µm particles). c) Microparticle bubble (FoV $9\times9\,mm^2$, 6.8 µm particles). A movie showing bubbles, blobs, and cusps (FoV $29\times19\,mm^2$, 6.8 µm particles, $\Delta T = 64.5\,K$, Ar) is available online [136].*

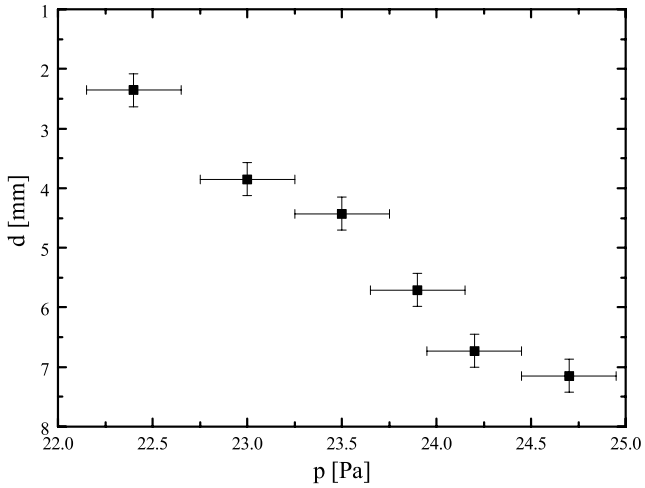

Figure 4.26: *Vertical distance d of the birth line, where the bubbles were formed, from the center of the chamber as a function of the gas pressure p measured with 6.81 µm particles at $\Delta T = 65\,K$.*

this happened is called *birth line*. Figure 4.26 shows the distance d of the birth line from the chamber center as a function of gas pressure. When the pressure was increased, the bubbles were formed closer to the lower edge of the particle cloud, until at some pressure the whole lower part of the microparticle cloud was involved in the bubble creation. The reason could be a saturation in the thermophoretic force at low pressures observed in [51] and explained by the authors as radiation cooling. Also, the temperature jump at the electrodes increases at lower pressures, reducing the effective temperature gradient maintained between the electrodes.

There was no visible correlation of the plasma glow with the bubbles. This is demonstrated in Figure 4.27: In this experiment, there was no filter positioned in front of the camera lens to block the plasma glow. The illuminating laser was regularly switched on and off, so that during intervals only the plasma glow was recorded. The contrast between the periods when the laser was on and those when it was off is clearly seen in the figure. While a small change in the plasma glow is visible over the course of several bubble events (probably due to a weak degradation of the plasma with time), there was no correlation with the advancing bubbles. To see the particles and the glow simultaneously, a lens with a small focal length was used. This method permitted to view only effects in the glow which were either very localized or very strong. A future experiment in which the setup is adjusted for a dedicated experiment to measure the plasma glow might result in more precise findings.

Figure 4.28 shows the effective current and voltage recorded in a set of four experiments dedicated to initiating the instability at various pressures by changing the temperature gradient. The experiment was scheduled as follows: A pressure was set while a temperature gradient was maintained in the chamber that was too low for bubble formation. Then, the temperature gradient was increased at a fixed pressure. The temperature gradient at which the instability appeared was recorded, and then the temperature was reduced to the initial value with a stable cloud. Next, the pressure was changed, and the sequence repeated. The instants when bubbles started are marked by solid vertical lines in the figure. At the lowest pressure, no bubbles appeared up to the maximal temperature difference of 66 K.

Figure 4.27: *Color-coded periodgram showing the formation of bubbles and the plasma glow. Scales are shown in the bottom left corner. The laser illuminating the particle cloud was switched on and off to allow recording the plasma glow only. The discharge images recorded when the laser was off are seen as vertical stripes. The colors were scaled (top) in the whole picture, (bottom) separately for the time when the laser was on/off to enhance the contrast of the intervals without laser. There is no correlation of the plasma glow with the particles ejected from the bubbles. The plasma glow became less intensive over the course of several bubble events, which was probably due to a weak degradation of the plasma with time.*

Note that the bubbles tended to appear at lower ΔT for higher pressures.

It can be seen that the asymmetry in the values of the effective currents reduced with the temperature gradient. This effect is the same at the low pressure at which no bubble formation was induced. It was probably caused by the fact that the vertical position of the particles was controlled by the applied temperature gradient. It is worth to note that the instability started at the instant at which the effective currents measured on the top and bottom electrodes were approximately equal. There was no indication of the onset of the instability in the discharge parameters such as effective voltage, current, and harmonics (not shown in the figure) in each individual experiment. There also was no indication of the fact that the instability did not occur at the lowest pressure in comparison with the previous experiments. Furthermore, there was no measurable correlation of these electrical parameters with the development of individual bubble events.

The bubble activity depended strongly on control parameters such as RF power, temperature gradient and gas pressure. It was possible to switch the activity on and off by changing any of these parameters. Sometimes a sudden change of a control parameter induced a transitory bubble, but the instability itself was not a transient phenomenon in general and could occur for a long time (for more than an hour). In the case of steady bubble activity, the microparticles that were pushed upwards to the upper void boundary

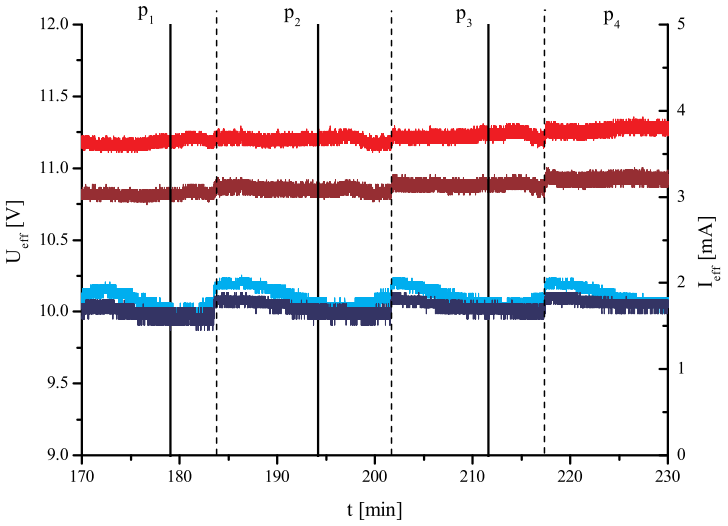

Figure 4.28: *Effective voltage (the two red upper curves) and current (the two blue lower curves) measured at the top (bottom) electrode (light, dark colors respectively) during four successive experiments. The instability was triggered by increasing the temperature differences between the ground plates ΔT. This was done at a different pressure in each experiment ($p_1 = 27.4\,Pa$, $p_2 = 25.3\,Pa$, $p_3 = 23.0\,Pa$, $p_4 = 20.6\,Pa$, pressure regimes indicated by dashed lines). The temperature regimes were $\Delta T = (58.5–64.5)\,K$ at $t = (172–180)\,min$, $\Delta T = (58.2–64.3)\,K$ at $t = (186–196)\,min$, $\Delta T = (58.2–65.0)\,K$ at $t = (202–213)\,min$, $\Delta T = (58.3–66.4)\,K$ at $t = (219–230)\,min$. The instants when bubbles started to appear are marked by solid vertical lines. The instability was not observed at the lowest pressure, p_4.*

flowed back underneath the void along the sides. Often, but not always, there were several consecutive bubbles ejected at the same position. Normally, the bubble birth points were random.

4.3.2 Hydrodynamic stability and analogies

Fast horizontal scans across the particle cloud showed that the particle blobs usually were completely isolated from the main microparticle cloud. Figure 4.29 depicts a reconstructed three-dimensional view of a blob obtained by scanning at a speed of 8 mm/s. The round shape of the main body of the blob is well visible. The blob featured a tail along which the particle density decreased compared with the rest of the blob, with an ending that appears frayed. This tail was not connected to the rest of the microparticle fluid. The bottom part of Figure 4.29 corresponds to the region below the void. Note the irregular

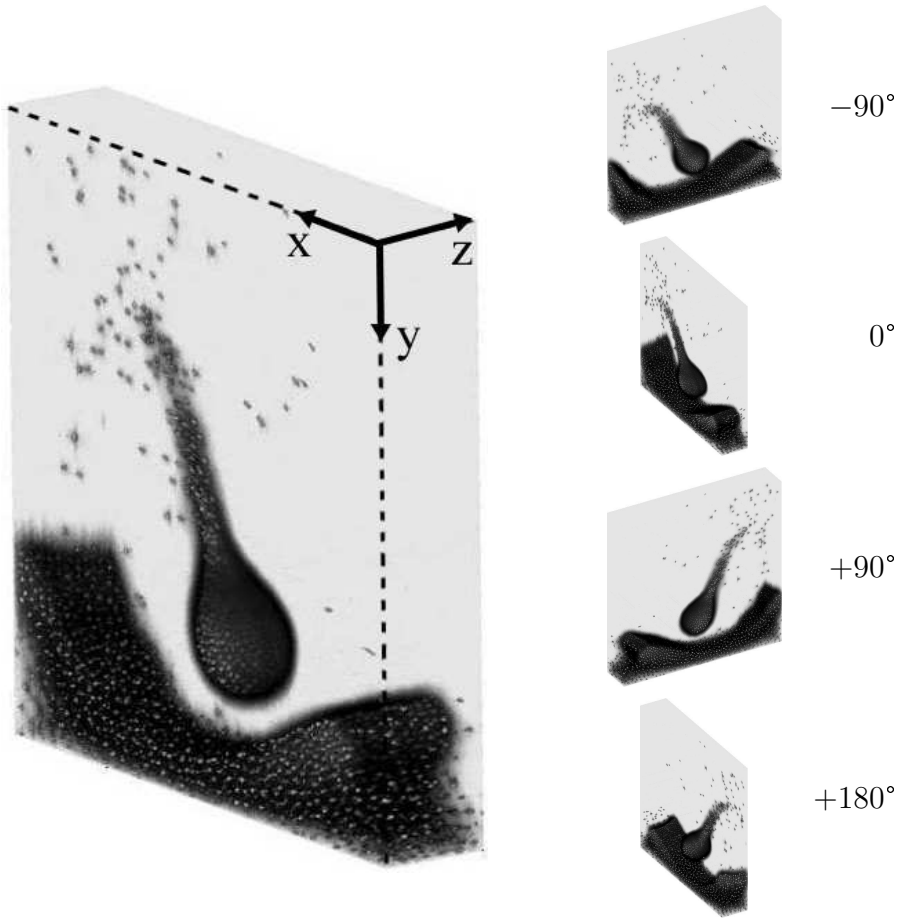

Figure 4.29: *Reconstructed three-dimensional view of a particle blob (field of view 11×2×12 mm³, particle size 6.8 µm, ΔT = 63.5 K, Argon plasma) recorded by scanning across the cloud at a speed of 8 mm/s. The pictures to the right show different projections of the same blob obtained by rotating around the vertical axis by 90° from one picture to another.*

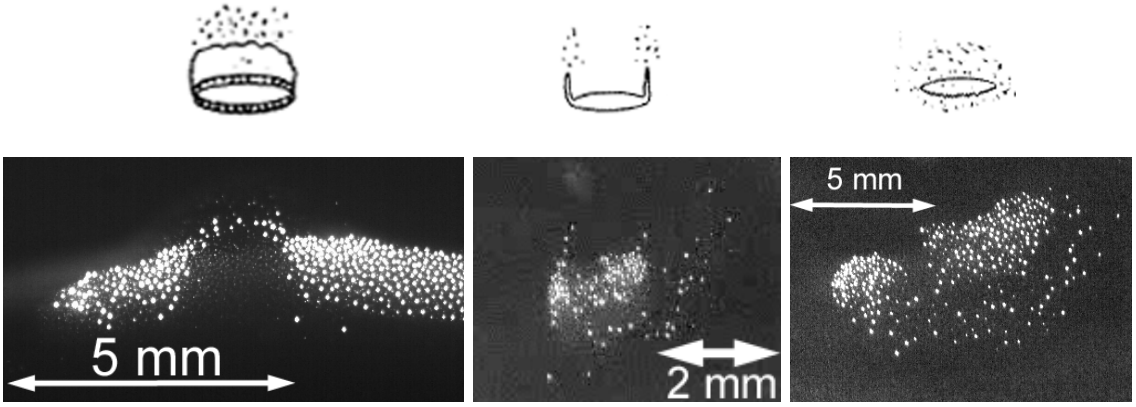

(a) *bag breakup* **(b)** *sheet stripping* **(c)** *wave crest stripping*

Figure 4.30: *Comparison between breakup types of liquid drops and microparticle blobs and bubbles. The drawings (top row) are borrowed from [123].*

structure of the void edge with indentations as mentioned above (Section 4.3.1, p. 77).

The blobs could, however, also still be connected to the rest of the microparticle cloud via a tail similar to the one seen in Figure 4.29. The blobs were observed to either be reabsorbed into the main microparticle cloud or break up eventually in a manner reminding of water drops in an air stream.

Figure 4.30 shows a comparison between the breakup mechanisms typical for water drops (see Section 1.6.2) and those observed with microparticles. The similarities are obvious: The breakup of bubbles reminds of bag breakup of drops (Figure 4.30a). Blobs sometimes also disintegrate all at once, reminiscent of wave crest stripping (Figure 4.30c). Single streams of ejected particles as in the sheet stripping breakup mechanism are often also found in the present blobs (Figure 4.30b). This is also similar as in blobs of macroscopic particles sedimenting in a fluid (Figure 4.31).

The Weber number $\mathcal{W}$, see Equation (1.5), is given by

$$\mathcal{W} = \frac{\rho v^2 l}{\alpha}. \tag{4.18}$$

It is a measure of the ratio of inertia to surface tension forces. In the case of the complex plasmas investigated here, an estimation yields $\rho \sim 0.03\,\mathrm{kg\,m^{-3}}$, $l \sim 3\,\mathrm{mm}$, and $v \sim 1\,\mathrm{cm/s}$. In order to assess the strength of the surface tension, one can consider the breaking up of the bubble lids. If during the time τ the total mass M is transported, then the surface tension coefficient α of the bubble lid break-up can be estimated as

$$\alpha \sim M/\tau^2. \tag{4.19}$$

An example of the break-up of a bubble lid is presented in Figure 4.32. Using Equation (4.19), it can be concluded $\alpha \sim (1\text{–}3) \cdot 10^{-10}\,\mathrm{kg\,s^{-2}}$. This results in $\mathcal{W} \sim 30\text{–}90$, which means that the break-ups were in the regime of bag, bag-and-stamen, and almost sheet stripping breakup [123].

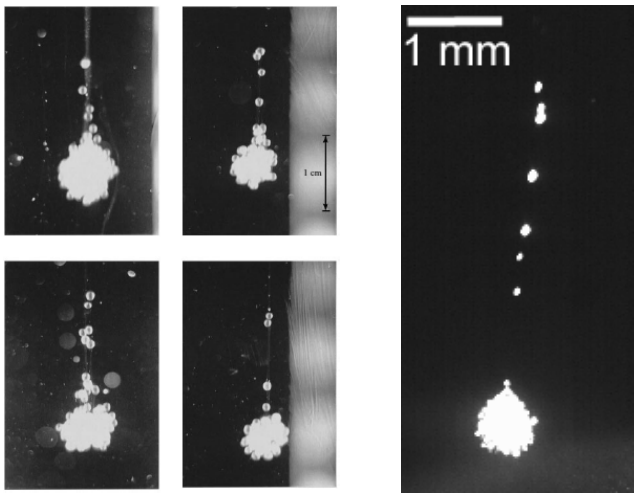

(a) *Glass particles sedimenting in glycerin. From [125].*

(b) *Microparticles in Neon, $\Delta T = 39\,K$.*

Figure 4.31: *Macroscopic particle blobs sedimenting in glycerin and a microparticle blob in a complex plasma.*

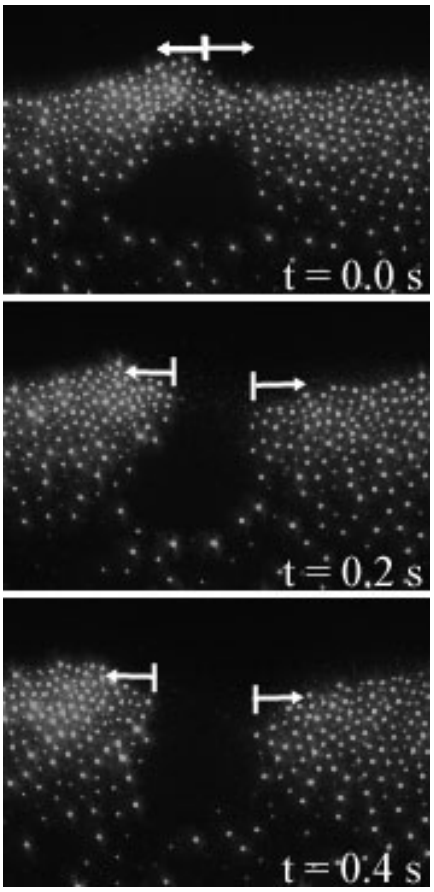

Figure 4.32: *Breaking up of a bubble lid (FoV $5 \times 3\,mm^2$). Three time moments are shown: the start-up ($t = 0.0\,s$), an intermediate one ($t = 0.2\,s$), and the final one ($t = 0.4\,s$). The arrows indicate the size of the opening as well as the direction of particle motion.*

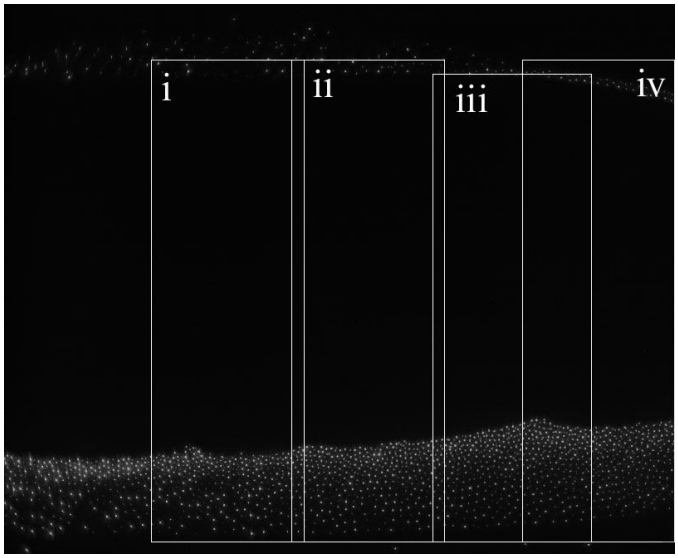

Figure 4.33: *Geometry of the regions analyzed more closely in Section 4.3.4. Note the microparticles levitated above the void. Field of view: 23×19 mm².*

4.3.3 Experiments under microgravity conditions

It is a challenge to observe liquid effects under microgravity conditions. Experiments dedicated to the formation of the observed instability were performed on board the ISS with the PK-3 Plus laboratory by the Russian cosmonauts Sergey Volkov and Yury Lonchakov. In order to induce the instability, the heating of the upper plate of the experimental chamber was turned on as strongly as possible, the pressure was set to a suitable value and the RF power was lowered. However, no bubble formation was observed: The cloud was shifted from the chamber center, but remained stable, not even the precursor stage of particles flying through the void was seen. Additionally, it was attempted to induce the instability during the DLR parabolic flight campaign with the PK-3 Plus setup, but it was not observed.

In both cases, the temperature gradient was set to values which were not as high as during the experiments on ground; during microgravity, such a strong thermophoretic force would have pushed all microparticles to the cold side of the chamber, inhibiting all possible bubble formation.

These results imply that to induce the instability, strong temperature gradients are needed. The fact that the instability was not observed with small particles (which are lifted up by a smaller temperature gradient) also supports this conclusion.

However, the enhanced stability of the microparticle cloud can be considered an advantage of experiments in "real" microgravity without the possible disturbance of creep-induced gas convection inside the discharge chamber (see Section 2.2.2).

4.3.4 Particle dynamics

Bubbles

In order to analyze the dynamics of particle movements caused by bubbles, the field of view provided by the camera was divided into four regions, as shown in Figure 4.33. An

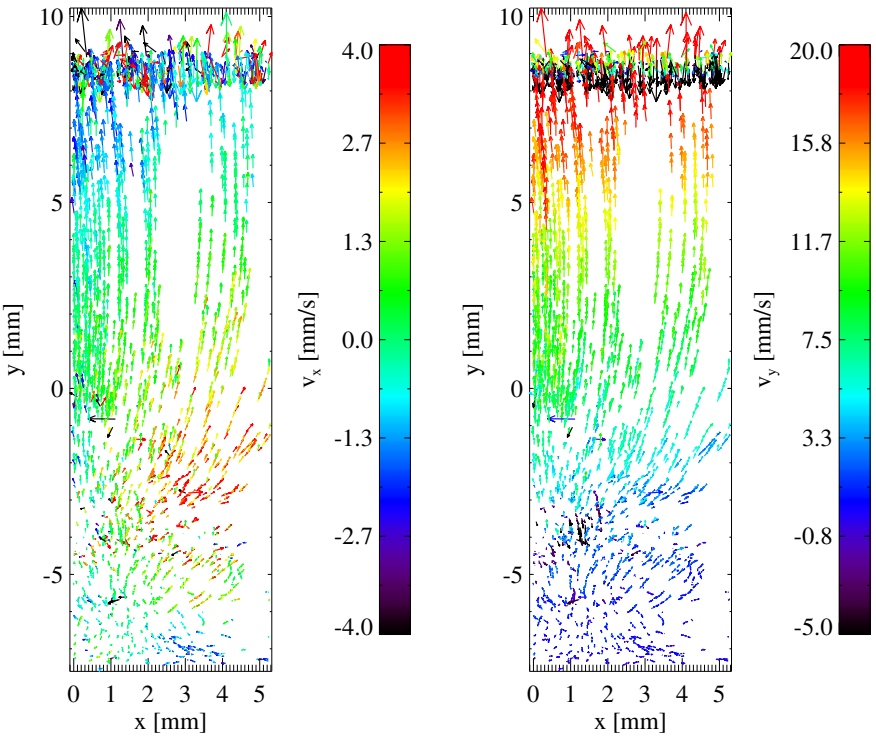

(a) *Horizontal velocities* **(b)** *Vertical velocities*

Figure 4.34: *Vector field of the velocities of the individual microparticles (uncertainty stemming from the error in the particle positions: ±2 mm/s) during a single bubble event in Region ii as shown in Figure 4.33. One tenth of the particle positions recorded during a time interval of 3.2 s length are superimposed. The vectors show the total velocities, the color code the values of the horizontal (left) and vertical (right) component. The color coding was truncated at the maximal and minimal values. The chamber center is positioned at y = 0.*

experiment was performed with (6.8±0.1) µm diameter microparticles in an Argon plasma at a temperature difference of 64.5 K and a pressure of 18 Pa. The measured electrical parameters were a mean peak-to-peak voltage of 31.4 V, a mean peak-to-peak current of 5.0 mA and a power of the RF generator of 54 mW. The particles in the four regions were traced and their velocities calculated. Figure 4.34 shows a vector plot of a single bubble event observed in Region ii.

The microparticles in the region above the void were strongly oscillating vertically, which is visible as a distinct horizontal line in the figure. The slow movement of the microparticles in the region below the void is also visible. During the bubble formation, the particles were first accelerated to the right, then the horizontal movement was stopped and converted into a slight movement to the left. In the vertical direction, the particles were strongly accelerated upwards, up to velocities of 20 mm/s and more.

All velocities in all four regions during a 14 times longer period of time are shown in Figure 4.35. The horizontal velocities are depicted in the top row, the vertical ones in

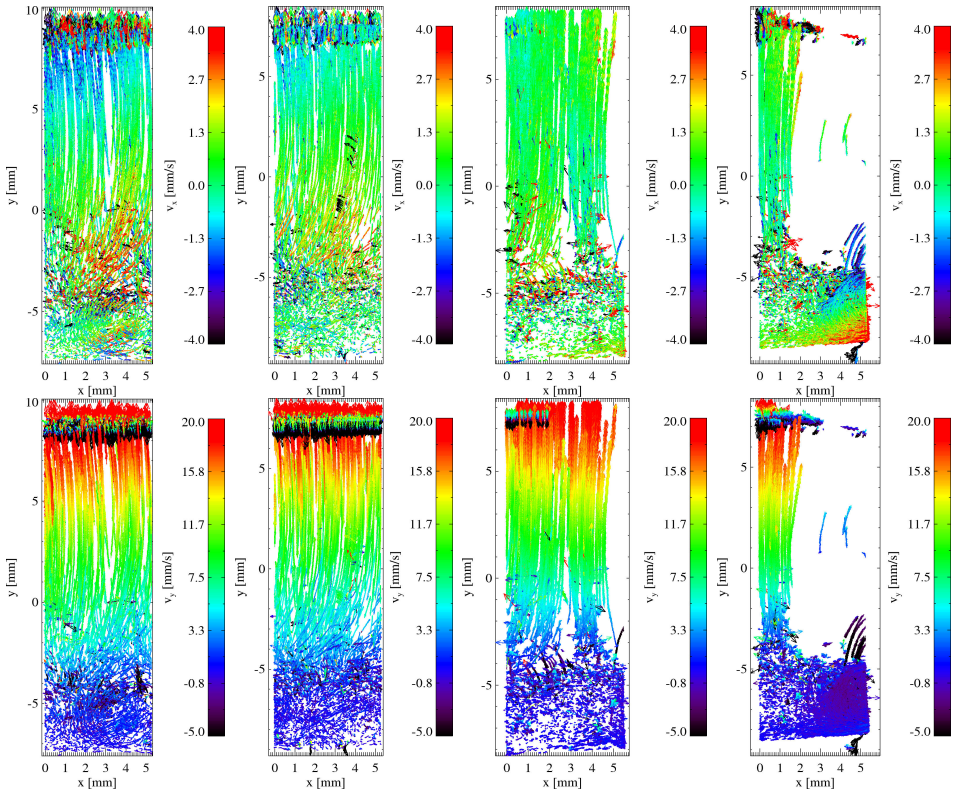

Figure 4.35: *Vector fields demonstrating velocities (uncertainty ±2 mm/s) of the microparticles during several bubble events (43.5 s in total) in Regions i–iv from left to right. As in Figure 4.34, the color-coding depicts (top) the horizontal velocities and bottom) the vertical velocities, and the velocities were truncated at the extreme values shown in the scale of the the color-coding.*

the bottom. The horizontal movement was clearly spatially dependent: There was more active movement to the left in the left regions i,ii and more to the right in the right regions iii and iv. This was due to the ion drag. (The ions were flowing to the walls of the plasma chamber from the center of the void.) The vertical movement induced by the bubble was not very different from one region to another. The particles were merely accelerated upwards.

Figure 4.36 shows the mean vertical velocity v_y, acceleration a_y, and normalized net force

$$F_y/m_d g = a_y/g + \gamma_{Ep} v_y/g \tag{4.20}$$

obtained from particle trajectories in Region ii. The mean velocity inside the particle cloud was zero. Inside the void, about 4 mm beneath the chamber center, the particles were accelerated upwards until they reached the particles above the void (not shown in the figure). Some particles fell back towards the lower part of the cloud before they reached the center of the chamber, decreasing the mean velocity in this region. Once the particles crossed the center of the chamber, they moved again with a velocity and force that increased more strongly with height than below the center. This was due to the

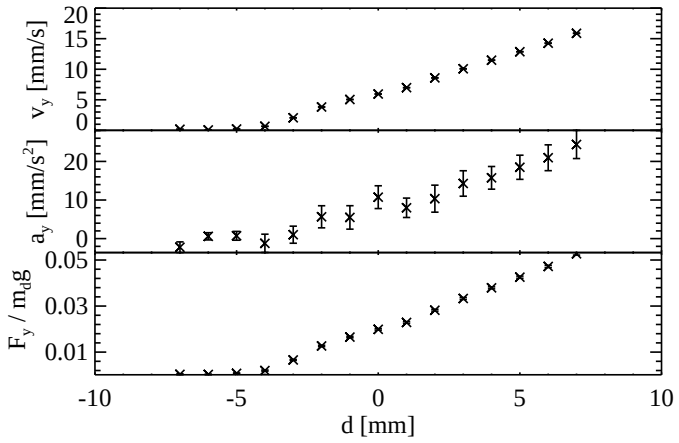

Figure 4.36: *Mean vertical velocity v_y, acceleration a_y, and normalized net force F_y/m_dg that were acting on the particles in Region ii as a function of the vertical coordinate d ($d = 0$ is the center of the chamber).*

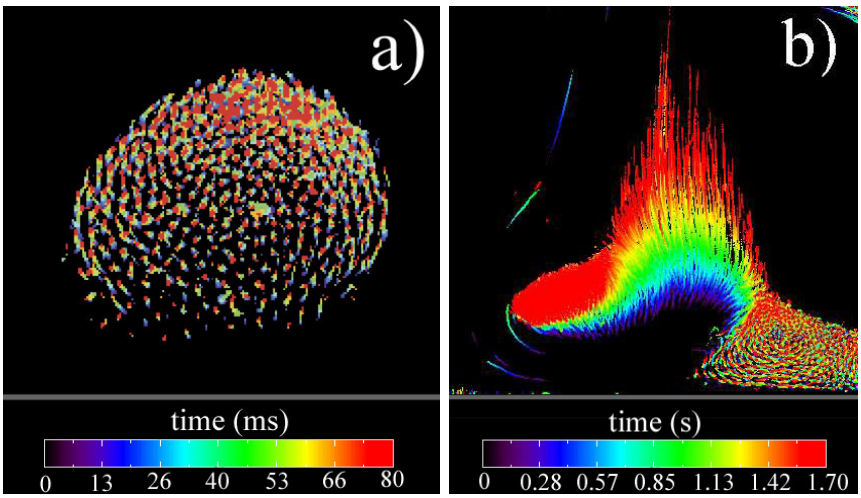

Figure 4.37: *Color-coded superposition of pictures demonstrating the movement of microparticles a) inside a blob (FoV 4×4 mm², 7.2 µm particles, ΔT = 63 K, Argon plasma) and b) while a bubble was forming (FoV 11×10 mm², 4.8 µm particles, ΔT = 49.5 K, Argon plasma).*

ions, which flowed outwards from the center of the void, and, hence, pushed the particles downwards below and accelerated them upwards above the center. It can be seen that the net force acting on the microparticles was as high as 5 % of gravity.

Blobs

The microparticle motion inside a blob and during the formation of a bubble is depicted in Figure 4.37. Figure 4.37a shows that the microparticles were moving along the edges of the blob upwards and more slowly downwards in the center of the blob, forming vortices. In Figure 4.37b, the upward accelerated motion of the microparticles during the formation of a bubble is visualized. Figure 4.37b also points to a formation mechanism of the blobs: At the later stages, the left part of the microparticle fluid is almost completely disconnected from the right part, resulting in a microparticle accumulation or blob remaining at the left side. Sometimes, blobs were also formed independently from bubbles: Being ejected from

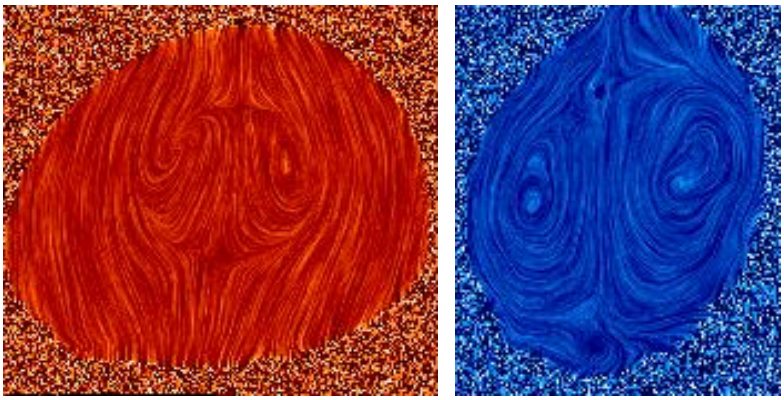

(a) *FoV 3.7×3.4 mm².* **(b)** *FoV 2.6×3.1 mm².*

Figure 4.38: *Flux lines of the flow inside two blobs, obtained with the method of LIC. The experiment was performed in Argon gas at $\Delta T = 63\,K$, and a pressure of 18.4 Pa. The left blob (a) is also depicted in Figure 4.37a.*

the microparticle fluid as a whole, they moved upwards into the void. There, they were compressed, and finally the quasi-spherical blobs were formed.

As already briefly discussed above, blobs frequently broke up by emitting a stream of particles into the void, often in the shape of a chain of particles similar to the spray shown in Figure 4.25. This is analogous to the sedimentation of particles in a fluid [125]. Blobs can also disintegrate, comparable to water drops in an air stream during wave crest stripping [122] (Figure 4.30).

Inside a blob, the microparticle cycled, forming vortices (Figure 4.37a) reminiscent of the motion observed inside a water drop [124] caused by the flow of a gas stream relative to the drop. The flux lines observed in blobs are shown in Figure 4.38. These maps were created with the method of line integral convolution (LIC) [218], which is commonly used to visualize vector fields. Here, the vector fields were obtained by identifying and tracing microparticles and then calculating an x-y-map with a velocity vector for every pixel. The LIC algorithm [219] next determined local stream lines for every pixel. A background image with random noise was then distorted along these streamlines, visualizing the movement.

Figure 4.38a shows the same blob as Figure 4.37a. The drift motion was numerically subtracted before applying the LIC. Probably, the blob was not horizontally centered on the laser plane, as the stream lines indicate that the particles left or entered into the plane on the top and bottom of the drop. In Figure 4.38b, the movement of the microparticle towards the top of the blob is visible, where they were ejected.

Cusps and sprays

In Figure 4.39 the time evolution of the formation of cusps is demonstrated. The figure shows a spray and a cusp in the system which was already analyzed in detail in pp. 86–89. The superimposed images demonstrate how the tip is formed: The initial round bump in the surface of the microparticle cloud was progressively sharpened, until at last the pointed apex was developed. This process took place on the time scale of 1–2 seconds. Sometimes particles-sprays were ejected in the later stages of this process. The conic cusp seen in the upper right corner features an angle close to the limiting angle of a Taylor cone [220] (red dashed line). Taylor cones are formed by electrically conductive liquids

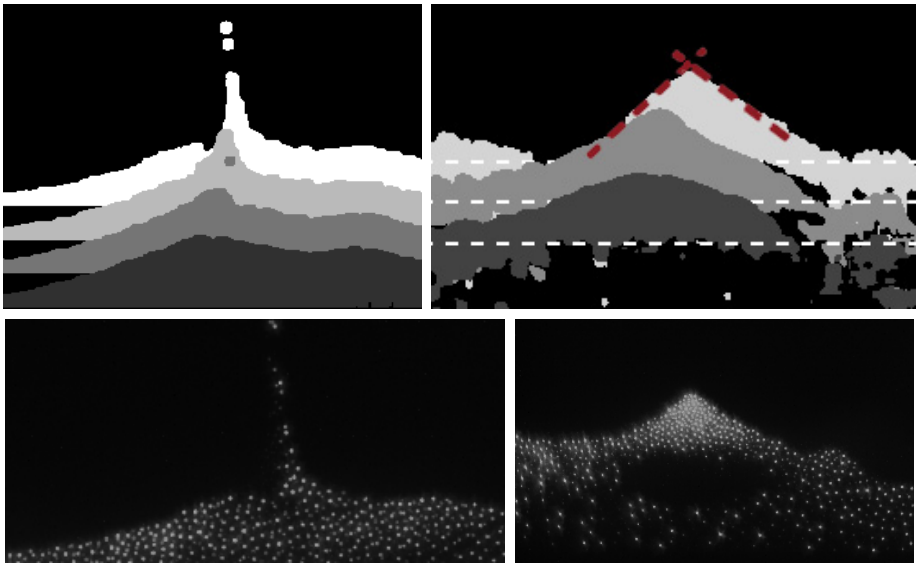

Figure 4.39: *Spray formation and evolution of a conic cusp (Argon plasma, 6.8 µm particles, temperature difference 64.5 K, pressure 18 Pa) . The FoVs are 9×4 mm^2 and 8×6 mm^2, left and right respectively. Top: The greyscale and upwards displacement, marked by horizontal lines, indicate time with steps of 0.48 s (left) and 0.4 s (right). The red dashed line shows a Taylor cone with limiting angle 98.6° [220]. Bottom: Corresponding snap shots. Note the strong compression of the particle fluid in the cusp in the image on the right.*

under the influence of forces induced by an electric field and surface tension which are approximately of the same strength. When a threshold voltage is reached, a jet is emitted from this cone, like in the cusps presented in the figure. The observation of Taylor cones is an indication of the presence of surface tension.

4.3.5 Creep effects

In order to determine what caused the upwards acceleration of the microparticles, the pressure dependence of their velocity was investigated. Figure 4.40 shows the mean particle velocity near the midplane of the chamber as a function of gas pressure. The velocity was smaller for small particles and decreased with pressure. This result excludes the Rayleigh-Bénard mechanism of gas convection as the cause of the particle movement, as the strength of this effect increases with pressure (also, the Rayleigh number (1.3) at such low pressures is five to six orders of magnitude below the critical number for the onset of Rayleigh-Bénard convection, $\mathcal{R}_{\text{crit}} = 1700$ [221]).

A mechanism that operates in rarefied gases and could explain the observations is thermal creep flow (see Section 2.2.2). Creep is induced in the direction of a temperature gradient along a wall [185, 191], and its strength is inversely proportional to pressure, therefore compatible with the measured pressure dependence depicted in Figure 4.40.

Figure 4.41 shows the critical temperature for the appearance of bubbles as a function of pressure for experiments with 6.8 µm particles and the expected temperature jump

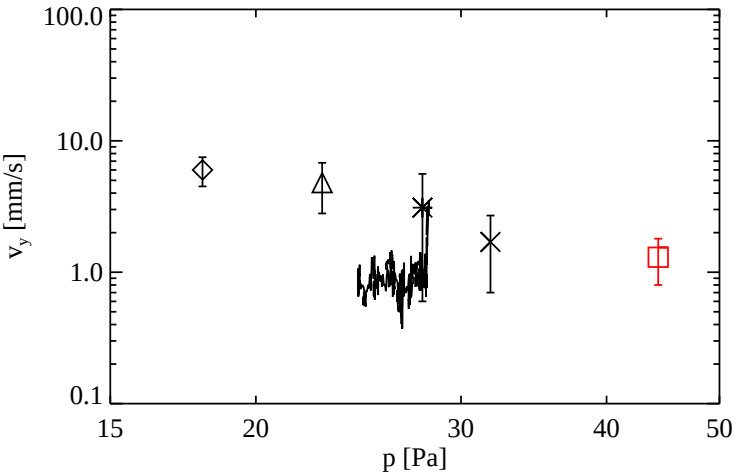

Figure 4.40: *Mean velocity of particles moving upwards versus gas pressure. The results correspond to different particle diameters* $2r_d$ *and temperature differences* ΔT *(diamond, triangle, star, and bold line:* $2r_d = 6.8\,\mu m$*,* $\Delta T = (63–64.5)\,K$*; cross and square:* $2r_d = 4.8\,\mu m$*,* $\Delta T = (45–48)\,K$*). The red square indicates measurements taken while the plasma was turned off. The bold line shows an experiment with a gradual pressure increase, in other experiments the pressure was kept constant. The error bars indicate the full width at half maximum (FWHM) of the velocity distributions.*

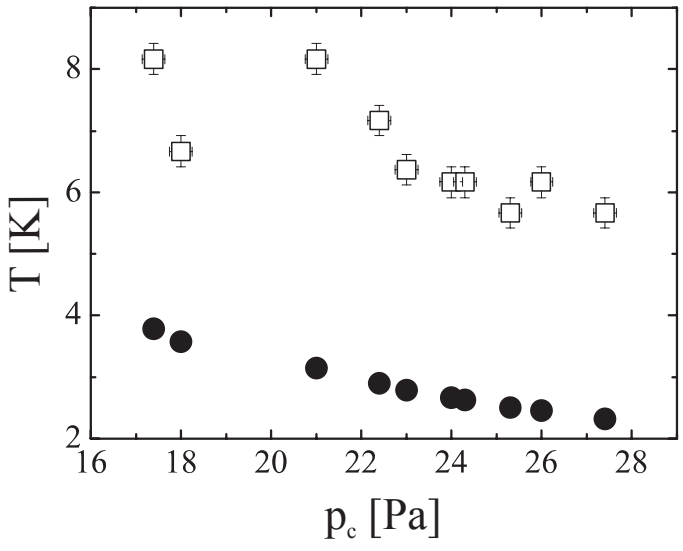

Figure 4.41: *Open symbols: excess of the critical temperature needed for the appearance of bubbles (above the equilibrium temperature needed to compensate gravity [51]). Filled symbols: total temperature jump between the electrodes and the gas predicted by [189].*

for these conditions across the Knudsen layer [189]. Both temperatures decreased with pressure and were also numerically close to each other, which shows that thermal creep flow may indeed have been present in the experimental setup.

4.3.6 Rayleigh-Taylor model

Now a phenomenological model that can explain the observed fluid activity is considered. The void boundary is stabilized by the drag force exerted by ions drifting from the center of the chamber towards the walls and electrodes. When the RF-power is lowered or the pressure increased up to the point where the plasma is near turn-off conditions, this ion flux becomes very weak. The acceleration (induced by thermophoresis or neutral drag caused by creep flow) of the microparticle fluid into the void may then lead to the development of a Rayleigh-Taylor instability at the interface [221], resembling that occurring in colloids under the influence of gravity [222, 223]. The instability in the experiments sometimes developed on a surface of rather thin "membranes" of thickness $H = (1\text{–}3)\,\mathrm{mm}$. The observed characteristic wavelength of the most unstable mode was typically $\lambda_{\max} \equiv 2\pi/k_{\max} \sim 3\,\mathrm{mm}$. Hence $H \cdot k_{\max} \geq 3$ and thus the "deep-water" regime is quite appropriate to describe the gravity-capillary waves.

The model depends on the acceleration of the destabilizing forces $\tilde{g}$ ("effective gravity", the sum of the forces exerted by thermophoresis, neutral gas flow, ion drag, and electric forces), the surface tension α, the mass density of the microparticle cloud ρ, and the damping rate coefficient γ_{Ep}. The resulting dispersion relation is

$$\omega^2 + i\gamma_{\mathrm{Ep}}\omega = -\tilde{g}k + (\alpha/\rho)k^3. \tag{4.21}$$

The maximal wave number can be derived from the condition that the differential of the growth rate vanishes. This yields $k_{\max}$ and the corresponding growth rate $\mathrm{Im}\,\omega_{\max}$

$$k_{\max} = \sqrt{\frac{\rho\tilde{g}}{3\alpha}}, \quad \mathrm{Im}\,\omega_{\max} \simeq \sqrt{\frac{4\rho\tilde{g}^3}{27\alpha\gamma_{\mathrm{Ep}}^2}}. \tag{4.22}$$

The typical observed value of the instability increment was about $\mathrm{Im}\,\omega_{\max} \simeq 2\,\mathrm{s}^{-1}$, which is more than an order of magnitude smaller than $\gamma_{\mathrm{Ep}} \simeq 50\,\mathrm{s}^{-1}$. Using this value and $\lambda_{\max}$ as observed in experiments with a typical density of $\rho \sim 0.03\,\mathrm{kg\,m}^{-3}$, Equation (4.22) provides the effective gravity $\tilde{g} \sim 0.1\,\mathrm{m\,s}^{-2}$ (which is about 1 % of g) and the surface tension $\alpha \sim 10^{-10}\,\mathrm{kg\,s}^{-2}$. The latter value is in good qualitative agreement with $\alpha \sim (1\text{–}3)\cdot 10^{-10}\,\mathrm{kg\,s}^{-2}$, which was estimated above by considering the mass transported during the opening of a bubble lid. Thus, capillary effects may indeed play an essential role in the observed instability.

Note that the alternative mechanism that can in principle provide the selection of the most unstable mode—particle diffusion—is not sufficient to be noticeable in the experiments presented here: Following [224], the wavenumber of the most unstable mode determined by diffusion is

$$k_{\max} \simeq (\frac{1}{16}\tilde{g}/D^2)^{1/3}. \tag{4.23}$$

Taking the value of the particle self-diffusion, $D \sim k_B T_g / m_\mathrm{d} \gamma_\mathrm{Ep} \sim 10^{-10}\,\mathrm{m^2\,s^{-1}}$ [225] (T_g: gas temperature, m_d: microparticle mass) as the upper limit for D results in $k_\mathrm{max} \gtrsim 2 \cdot 10^5\,\mathrm{m^{-1}}$, which corresponds to λ_max smaller than the interparticle distance. This mechanism therefore is not suitable to explain the observed instability.

Another effect which could contribute to the confinement of the blobs are local space charges. This model has first been proposed as a model of the atom by Thompson [226]: the electrons are embedded in a neutralizing ion background which generates a parabolic confining potential. Totsuji et al. [227] numerically investigate a spherical plasma chamber with a complex plasma under microgravity conditions and demonstrate the possibility of the formation of layers in the spherical complex plasma ball, reminding of Coulomb clusters [228]. In the present experiment, no such layers were observed in the microparticle blobs. This implies that the blobs were in a quasi-fluid state, not in the thermodynamic ground state.

Capillary effects are known to be important for cusps [229, 230]. The sharpness of the cusp tip is controlled by the capillary number $\mathcal{C}$

$$\mathcal{C} = \eta v / \alpha, \tag{4.24}$$

where η is the dynamic viscosity and v the stream velocity. Using the critical value of $\mathcal{C} = 0.25$ predicted in [229], ρ and α as given above, as well as a kinematic viscosity value $\nu = 1\,\mathrm{mm^2\,s^{-1}}$ typical for complex plasmas [63, 231] yields $v \sim 1\,\mathrm{mm\,s^{-1}}$, which is well in the interval of the observations.

All these examples demonstrate that the Rayleigh-Taylor model is feasible and consistent. Future work includes analyzing the growth mechanism of the instabilities on the surface of the liquid complex plasma and comparing with predictions from the Rayleigh-Taylor theory, and a further investigation of the confining mechanism of the blobs, including possible ion drag terms and space charges.

4.3.7 Conclusion

For the first time, a new phenomenon occurring near the surface of fluid complex plasmas was investigated—the formation of microparticle bubbles, blobs, and surface cusps under the influence of thermophoresis. The behavior of microparticles was similar to that observed in fluid drops and with sedimenting particles, including the breakup mechanism and vortex motion of particles inside the blobs. The forces acting on the microparticles were analyzed and the velocity scaling with pressure was shown to be compatible with a possible flow induced by thermal creep inside the plasma chamber. Various effects were observed that indicate the presence of surface tension, such as the formation of cusps with angles corresponding to those of Taylor cones, the self-confinement of blobs inside the void, and the break-up of bubble lids. Furthermore, qualitative agreement was found with the Rayleigh-Taylor instability.

Chapter 5

Summary and outlook

Plasmas are ubiquitous in the universe and become more and more common in technical applications on Earth as well. In these plasmas, dust occurs often as an additional particle species and can have both beneficial and harmful consequences. In the field of complex plasmas, microparticles are introduced purposefully into a plasma. These systems have the advantage that the individual particles can be visualized in experiments, enabling a study on the kinetic (atomistic) level. Complex plasmas provide excellent model systems to investigate effects which are common in other fields of physics, for example melting and recrystallization, and waves and transport phenomena.

In this thesis, fluid complex plasmas were used to experimentally explore dynamical effects. Two main analysis methods were developed and employed to interpret the results of measurements and observations: periodgrams and microparticle tracing. Periodgrams provide a very good overview of the processes occurring in the system and make it possible to determine averaged characteristics. Tracing the particles allows a detailed study involving the trajectories of individual particles, and makes the calculation of velocity and force fields practicable.

The PK-3 Plus laboratory, which is based on a parallel plate radio-frequency plasma reactor, was used for the presented work. Experiments were performed on ground, during a parabolic flight and on board the International Space Station (ISS). The setup used on ground and in parabolic flight experiments was equipped with a high speed data recording system, which provides the means to investigate the particle dynamics at high temporal resolution, and also to perform fast scans through the system, resulting in three-dimensional measurements.

During the experiments, it was possible to maintain a vertical temperature gradient in the plasma chamber, and the microparticles could thus be subjected to an adjustable "effective gravity" caused by the thermophoretic force, counteracting, compensating, or even overcompensating gravity.

Important elements of any self-organization process in different media under external forcing are autowaves, which occur in a vast variety of systems. In the complex plasmas studied here, autowaves are excited at low gas pressures or at high discharge currents by the ions streaming towards the chamber walls and electrodes.

In this thesis, self-excited dust density waves were investigated under external forcing induced by thermophoresis. When gravity was compensated for, there were no waves self-excited in the system. Only when the thermophoretic force was stronger or weaker than gravity, waves could be observed. In unstable conditions, the oscillations of the

microparticles started at the edge of the particle cloud closest to either the upper or lower electrode. They spread over the entire cloud at lower pressures. The dependence of the critical pressure at which the waves were excited on the thermophoretic forcing was examined. It was shown that the observed scaling is explained by the theory proposed in literature based on the drag of ions streaming to the electrodes, mainly in the sheath regions.

At the nonlinear stage, the self-excited waves were clearly seen as denser traveling wave ridges. The particle movement was traced between and inside the wave ridges at a high spatial and temporal resolution. It was shown that the microparticles inside the wave were captured by the waves fronts, traveled within them for a short distance, and then left the wave ridge, attempting to relax back towards their original position. All this was part of a global coherent process, spread over the entire cloud. The associated velocity and force fields were measured, and the microparticle charge was estimated using a model based on the balance of the incoming and outgoing particle fluxes. The calculated charge value agrees well with that predicted theoretically.

Whether intense self-excited waves in complex plasmas exist under microgravity conditions is still under debate in the complex plasma community. In this thesis, it was shown that waves were not self-excited by lowering the gas pressure during a parabolic flight experiment in the PK-3 Plus setup under conditions similar to those used to study waves on the ground. However, a very weak horizontal oscillation localized at the cloud edges was observed on board the ISS even without external excitation in an experiment studied in the course of this work.

Microgravity conditions are optimal for investigating externally exited waves. In an experiment presented in this thesis, a low frequency modulation voltage was applied to the electrodes of the PK-3 Plus chamber on board the ISS. It was demonstrated that the response of the microparticles was more complicated than previously thought. Even without external modulation, weak horizontal waves and a breathing mode of the whole cloud were present. When the modulation frequency was applied, a global vertical slashing mode was excited at the modulation frequency. Increasing the modulation frequency widened the wave spectrum: At a frequency of 3 Hz the intense shaking of the microparticles induced periodic nonlinear wave ridges in the bottom and top parts of the cloud. The modulation also intensified the horizontal waves localized at the horizontal cloud edges. At higher frequencies ($f_{\mathrm{mod}} \geq 4.5\,\mathrm{Hz}$) additional oblique quasi-sound wave ridges started to propagate through the cloud. At a modulation frequency of (9–13) Hz, the horizontal and vertical regions of wave excitation were connected by the oblique waves. At even higher modulation frequencies ($f_{\mathrm{mod}} > 17$ Hz), the oblique waves were suppressed.

The wave dispersion relation was measured in the interval of 0 to 17 Hz of modulation frequencies and compared with literature values. In addition, the microparticles were traced and their trajectories analyzed. The distribution of velocity and force fields was studied and contrasted with the distribution of the waves ridges. It was established that in the microparticle cloud, several complex plasma modes (breathing, slashing, waves) were superimposed depending on the applied modulation frequency.

Low-gravity conditions can be simulated by applying a thermophoretic force to the system under the influence of gravity. Under those conditions, when the discharge power

was low, a novel phenomenon of fluid complex plasmas emerged—the formation of bubbles, blobs, and surface cusps. It was possible to turn the instability on and off by adjusting control parameters such as temperature gradient, cloud density or gas pressure.

The detailed dynamics of bubbles, blobs, cusps and the accompanying motion of the microparticles was investigated. It was demonstrated that many similarities with phenomena in conventional fluids and with particles sedimenting in a fluid exist, for instance, many break-up mechanisms are observed in all three systems. Fast horizontal scans were performed to analyze the three-dimensional structure of the blobs, revealing that the blobs were self-contained. Microparticle tracing revealed that the particles moved in vortices inside the blobs.

The microparticle velocities and the forces acting on them were analyzed as a function of vertical and horizontal position, indicating the influence of ion drag inside the void. It was also shown that the velocity scaling with pressure was compatible with a possible convection of the gas induced by thermal creep, which is an effect occurring in low pressure gases in which a temperature gradient along a wall is present.

Even at the small "nano-scales" of few hundreds of particles, several effects indicating the presence of surface tension were observed, such as the fact that the angles of the cusps often resembled those of Taylor cones, and the compression into blobs of loose ensembles of microparticles ejected into the void.

A model based on the Rayleigh-Taylor instability was proposed as the driving mechanism of the instability. The predictions of the model are in fairly good agreement with the observations. Experiments dedicated to the investigation of the instability under microgravity conditions were also briefly discussed. They indicate that strong temperature gradients are necessary for the triggering of the instability.

Many possible future investigations on dynamical effects in fluid complex plasmas provide interesting research opportunities. Additional experiments on board the ISS are planned in a cooperation between the MPE and the Christian-Albrechts-Universität zu Kiel to solve the debate about the existence of intense self-excited waves under microgravity conditions [118].

The investigations of self-excited waves can be continued using the ground setup with thermophoresis. An interesting topic in this context are bifurcations; in the experiments presented in this thesis, branching of the wave ridges occurred at the edges of the cloud. It would be worthwhile to investigate the conditions under which these bifurcations appear, whether they travel in space, and what their kinetic origins are.

Concerning externally excited waves, the question under which conditions it is possible to assume that the wave frequency is equal to the modulation frequency still remains open. This assumption is widely used in literature when the dispersion relation of dust acoustic waves is studied. Another interesting subject for investigations is the origin of the weak horizontal oscillations insensitive to the modulations discussed briefly in this thesis. The physics of the "self-activity" is still under debate.

It is essential to uncover the convection-related effect that is probably present in the system. To visualize a possible gas flux (maybe induced by thermal creep), measurements

with a schlieren photographic system[1] might be performed. A better study of the plasma glow with a specially adapted optics system might demonstrate a non-homogeneous plasma production. The physics of surface tension in complex plasmas has also not yet been explained in detail. More experiments, simulations and elaborate models are required.

Additional advanced observations are required to further investigate the mechanism of the Rayleigh-Taylor instability in fluid complex plasmas. This type of instability might also exist at the interfaces between clouds of microparticles of different sizes. It might be induced experimentally by manipulating these microparticles such that the two clouds interpenetrate each other.

Moreover, the method of periodgrams introduced in this thesis is applicable to many other dynamical effects in complex plasmas. It already has found application to complex plasmas in DC [233] and RF discharges [186, 234, 235]. And, of course, the possibility of true investigations on the kinetic level that complex plasmas provide will make many additional, exciting studies possible: With these systems, effects can be examined down to the limits of cooperative phenomena. The "corpuscular (discrete)" effects provide insights into nano-phenomena from a very different approach, for instance, surface and membrane physics can be studied in both the continuum approximation and down to the regions where cooperative behavior starts.

[1] With those systems, density gradients in gases can be visualized locally by imagining along a sharp edge. This technique has been successfully applied at gas pressures as low as 50 Pa [232].

Appendix A

Other charging mechanisms

The main charging mechanism of the microparticles, charging by ions and electrons collected on the grain surface, is already treated in Section 2.2.1. Estimates show that, under the given laboratory conditions, all other charging mechanisms are weaker than the collection of ions and electrons and will be neglected. The other possible mechanisms are [2, 236]:

- **secondary electron and ion emission**: Electrons or ions impinging on the grain surface can penetrate through the surface, be scattered on or be re-emitted together with secondary electrons and ions, affecting the charge of the microparticle. The yield of secondary emission depends on the particle material and the impact energy and is usually much larger for electron impact than for ion impact [237]. It is only important for high energies of the impacting particles [236], e.g., for electron impact $E > 50\,\mathrm{eV}$ [8]. These energies can be obtained in plasmas mainly in the tail of the electron distribution. Walch, Horányi, and Robertson [238] showed that under laboratory conditions, the secondary electron emission induced by electrons with energies of some eV can be neglected; it only becomes important for suprathermal electrons.

  Ions moving towards the grain are neutralized by electrons tunneling through the potential barrier during the approach or at the surface. The recombination energy gained in this process can also affect the emission of additional electrons [236].

- **photoemission**: If the energy of an impacting photon is greater than the work function of the microparticle, an electron escapes from the surface. For most materials, the work function W_p does not exceed 6 eV [239]. For metals under low and moderate radiation fluxes ($< 1\,\mathrm{W\,cm^{-2}}$), W_p is of the order of (2–3) eV, for semiconductors and dielectrics it is slightly higher [240]. Therefore, UV radiation suffices to affect the charge of the particles. This method has been used to obtain positively charged microparticles by exposing the system to solar radiation by Fortov et al. [60]. In RF plasmas, the plasma itself emits some UV radiation, but the radiation intensity is not enough to noticeably affect the microparticle charge.

- **thermionic emission**: When a microparticle is strongly heated, the ions and electrons on the surface also gain thermal energy. They are emitted from the microparticle when their thermal energy becomes larger than the binding energy. Energy which heats the microparticles in a plasma is transferred by collected ions and electrons and during their recombination [196]. Swinkels et al. [213] measured the temperature of

1.2 µm MF microparticles in an Argon RF plasma and demonstrated a slight overheating of the particles (grain temperatures between 100 and 200 °C depending on the RF power). The minimal power used was 2 W, which is an order of magnitude larger than typical powers used in the PK-3 Plus chamber. Akdim and Goedheer [241] showed that in the PKE-Nefedov chamber, typical particle temperatures are of the order of room temperature. All the obtained temperatures are too small for thermionic emission to make a substantial contribution to the electron flux; dielectric particles usually melt before thermionic emission becomes important [11]. If microparticles with a high melting point are used, they can for instance be heated with a laser to high temperatures. Shukla and Mamun [2] estimate the required intensity of a laser for thermionic emission to be important as $300\,\mathrm{W\,cm^{-2}}$, which can be reached by an infrared laser. Fortov et al. [242] studied CeO_2 microparticles immersed in a thermal plasma produced by a two-flame burner. Electrons, ions, atoms and microparticles all had temperatures of (1700–2200) K, and the microparticles were charged positively by thermionic emission.

- **field emission**: If a grain possesses a strong electric potential, ions or electrons are emitted from the surface. This effect limits the obtainable potential of the grains to $\phi = (100\,r_\mathrm{d})\,\mathrm{V}$ (r_d in µm) [236], i.e., it would be 1000 V at $r_\mathrm{d} = 10\,\mu\mathrm{m}$. In RF discharges, ϕ is of the order of a few Volt.

- **radioactivity**: Grains in a radioactive environment can be charged by secondary electron emission induced by a penetration of a nuclear particle or become radioactive themselves and emit charged particles [243]. This effect may be important in fusion reactors, but in the present experiment, no radioactive particles are used.

- **impact ionization**: When an ion or a neutral atom hits the grain surface with a high velocity, either the incoming particle or atoms on the grain surface can be ionized, leading to the escape of electrons. This effect is only important for high neutral gas densities or high relative velocities [2].

Appendix B

Simulation of temperature gradient

The plasma chamber used in the experiments presented in this thesis is exposed to a strong temperature gradient. In order to simulate the distribution of the temperature in the chamber and shown in Chapter 3.2.1, the heat transfer by conduction is considered. It is given by the heat equation

$$\rho c_{\mathrm{p}} \frac{\partial T}{\partial t} - \boldsymbol{\nabla} (\kappa \boldsymbol{\nabla} T) = Q, \tag{B.1}$$

where ρ denotes the density, c_{p} is the specific heat capacity, and κ represents the thermal conductivity of the heat conducting fluid. Q is a potential heat source. To take a possible convection into account, a convective term is added, which yields [244]

$$\delta_{\mathrm{ts}} \rho c_{\mathrm{p}} \frac{\partial T}{\partial t} - \boldsymbol{\nabla} (\kappa \boldsymbol{\nabla} T) = Q - \rho c_p \boldsymbol{v} \cdot \boldsymbol{\nabla} T, \tag{B.2}$$

where $\boldsymbol{v}$ is the velocity of the fluid, and an incompressible fluid flow $\boldsymbol{\nabla} \cdot \boldsymbol{v} = 0$ is assumed. The time scaling coefficient δ_{ts} is later set to 1.

The convection and conduction model of FEMLAB 3.0 without heat sources and in steady-state mode is used to solve this equation. Further assumptions are

- a fixed temperature of 30 ℃ at the upper and 95 ℃ at the lower boundary
- heat flux along the vertical walls of the chamber, but no inward heat flux from the sides
- isotropic thermal conductivity κ
- no initial velocities of the fluid.

The geometry of the PK-3 Plus chamber[1] was modeled. The chamber was assumed to be filled with Argon at a density of $\rho = 3 \cdot 10^{-4}\,\mathrm{kg\,m^{-3}}$. The heat capacity $c_{\mathrm{p}} = 520\,\mathrm{J/(kg\ K)}$ and thermal conductivity $\kappa = 17.9 \cdot 10^{3}\,\mathrm{W/(m\ K)}$ [65] were used.

The software uses the finite element method with lagrange-quadratic elements to solve Equation B.2. The result is output in the form of Figure 3.5, which depicts the distribution of the temperature gradient and the temperature in the PK-3 Plus chamber.

[1] total height (length) 5.4 cm (10 cm), height (length) of electrodes and guard ring combined 1.2 cm (9 cm).

List of Figures

List of Tables

Bibliography

[1] M. Goossens. *An introduction to plasma astrophysics and magnetohydrodynamics*. Ed. by W. B. Burton. Kluwer Academic Publishers, 2003. See p. 1.

[2] P. K. Shukla and A. A. Mamun. *Introduction to Dusty Plasma Physics*. Bristol: Institute of Physics Publishing, 2002. See pp. 1, 2, 22, 23, 28, 29, 35, 99, 100.

[3] V. A. Rakov and M. A. Uman. *Lightning: physics and effects*. Cambridge University Press, 2007. See p. 2.

[4] H. J. Christian and M. A. McCook. *A Lightning Primer*. Online. Accessed on 04. March 2009. URL: http://thunder.nsstc.nasa.gov/primer/primer2.html. See p. 2.

[5] N. G. D. Center. *Introduction to the Ionosphere*. Online. Accessed on 04. March 2009. URL: http://www.ngdc.noaa.gov/stp/IONO/ionointro.html. See p. 2.

[6] P. Bradu. *L'Univers des Plasmas*. Paris: Flammarion, 1999. See p. 2.

[7] N. F. Ness. "Observed Properties of the Interplanetary Plasma." *Ann. Rev. Astron. Astrophys.* **6**, 79–114 (1968). DOI: 10.1146/annurev.aa.06.090168.000455. See p. 2.

[8] V. Land. *Computing the Complex - Dusty plasmas in the presence of magnetic fields and UV radiation*. PhD thesis. FOM-Instituut voor Plasmafysica Rijnhuizen, 2007. See pp. 2, 99.

[9] T. P. Snow and B. J. McCall. "Diffuse Atomic and Molecular Clouds." *Ann. Rev. Astron. Astrophys.* **44**, 367–414 (2006). DOI: 10.1146/annurev.astro.43.072103.150624. See p. 2.

[10] H. M. Thomas and G. E. Morfill. "Melting dynamics of a plasma crystal." *Nature* **379**, 806–809 (1996). DOI: 10.1038/379806a0. See pp. 2, 6, 27.

[11] V. Fortov et al. "Complex (dusty) plasmas: Current status, open issues, perspectives." *Phys. Rep.* **421**, 1 –103 (2005). DOI: 10.1016/j.physrep.2005.08.007. See pp. 2, 4–6, 24, 33, 100.

[12] J. H. Vincent. *Aerosol Sampling*. Wiley, 1989. See p. 2.

[13] S. Robertson and Z. Sternovsky. "Smoky Plasma." *IEEE Trans. Plas. Sci.* **35**, 314–322 (2007). DOI: 10.1109/TPS.2007.892135. See p. 2.

[14] C. K. Goertz. "Dusty plasmas in the solar system." *Rev. Geophys.* **27**, 271–292 (1989). DOI: 10.1029/RG027i002p00271. See p. 2.

[15] *Nasa Images*. URL: http://www.nasaimages.org. See p. 3.

[16] B. A. Smith et al. "Encounter with Saturn: Voyager 1 Imaging Science Results." *Science, New Series* **212**, 163 –191 (1981). DOI: 10.1126/science.212.4491.163. See p. 2.

[17] B. A. Smith et al. "A New Look at the Saturn System: The Voyager 2 Images." *Science, New Series* **215**, 504–537 (1982). DOI: 10.1126/science.215.4532.504. See p. 2.

[18] C. A. McGhee et al. "HST observations of spokes in Saturn's B ring." *Icarus* **173**, 508 –521 (2005). DOI: 10.1016/j.icarus.2004.09.001. See p. 2.

[19] C. J. Mitchell et al. "Saturn's Spokes: Lost and Found." *Science* **311**, 1587 (2006). DOI: 10.1126/science.1123783. See p. 2.

[20] C. K. Goertz and G. Morfill. "A model for the formation of spokes in Saturn's ring." *Icarus* **53**, 219 –229 (1983). DOI: 10.1016/0019-1035(83)90143-4. See p. 2.

[21] J. R. Hill and D. A. Mendis. "On the braids and spokes in Saturn's ring system." *Moon & Planets* **24**, 431 –436 (1981). DOI: 10.1007/BF00896908. See p. 2.

[22] U. Konopka et al. "Charge-induced gelation of microparticles." *New J. Phys.* **7**, 227 (2005). DOI: 10.1088/1367-2630/7/1/227. See p. 3.

[23] J. Y. Cho and M. C. Kelley. "Polar Mesosphere Summer Radar Echoes: Observations and Current Theories." *Rev. Geophys.* **31**, 243–265 (1993). See p. 3.

[24] O. Havnes et al. "First detection of charged dust particles in the Earth's mesosphere." *J. Geophys. Research* **101(A5)**, 10839 –10847 (1996). See p. 3.

[25] O. Havnes, T. Aslaksen, and A. Brattli. "Charged Dust in the Earth's Middle Atmosphere." *Physica Scripta* **T89**, 133 –137 (2001). DOI: 10.1238/Physica.Topical.089a00133. See p. 3.

[26] K. Narihara et al. "Observation of dust particles by a laser scattering method in the JIPPT-IIU tokamak." *Nucl. Fusion* **37**, 1177 –1182 (1997). DOI: 10.1088/0029-5515/37/8/I12. See p. 3.

[27] V. N. Tsytovich and J. Winter. "On the role of dust in fusion devices." *Phys.-Usp.* **41**, 815–822 (1998). DOI: 10.1070/PU1998v041n08ABEH000431. See p. 3.

[28] J. Winter. "Dust in fusion devices - experimental evidence, possible sources and consequences." *Plasma Phys. Control. Fusion* **40**, 1201 –1210 (1998). DOI: 10.1088/0741-3335/40/6/022. See p. 3.

[29] J. P. Sharpe, D. A. Petti, and H.-W. Bartels. "A review of dust in fusion devices: Implications for safety and operational performance." *Fusion Eng. Design* **63-64**, 153 –163 (2002). DOI: 10.1016/S0920-3796(02)00191-6. See p. 3.

[30] S. Rosanvallon et al. "Dust in ITER: Diagnostics and removal techniques." *J. Nuc. Materials* **Article in Press**, (2009). DOI: 10.1016/j.jnucmat.2008.12.195. See p. 3.

[31] M. A. Lieberman and A. J. Lichtenberg. *Principles of Plasma Discharges and Materials Processing*. 2nd ed. Hoboken, New Jersey, USA: John Wiley & Sons, 2005. See pp. 3, 19, 21, 22.

[32] L. Boufendi and A. Bouchoule. "Industrial developments of scientific insights in dusty plasmas." *Plasma Sources Sci. Technol.* **11**, A211 –A218 (2002). DOI: 10.1088/0963-0252/11/3A/332. See p. 4.

[33] G. S. Selwyn et al. "In situ contamination measurements by HeNe laser light scattering: A case study." *J. Vac. Sci. Technol. A* **8**, 1726 (1990). DOI: 10.1116/1.576838. See p. 4.

[34] K. D. Bleecker, A. Bogaerts, and W. Goedheer. "Modelling of nanoparticle coagulation and transport dynamics in dusty silane discharges." *New J. Phys.* **8**, 178 (2006). DOI: 10.1088/1367-2630/8/9/178. See p. 4.

[35] G. S. Selwyn, J. E. Heidenreich, and K. L. Haller. "Particle trapping phenomena in radio frequency plasmas." *Appl. Phys. Lett.* **57**, 1876 (1990). DOI: 10.1063/1.104021. See p. 4.

[36] K. Ostrikov. "Reactive plasmas as a versatile nanofabrication tool." *Rev. Mod. Phys.* **77**, 489 –511 (2005). DOI: 10.1103/RevModPhys.77.489. See p. 4.

[37] T. Shimizu et al. "Characterization of Microwave Plasma Torch for Decontamination." *Plasma Process. Polym.* **5**, 577 –582 (2008). DOI: 10.1002/ppap.200800021. See p. 4.

[38] R. F. Wuerker, H. Shelton, and R. V. Langmuir. "Electrodynamic Containment of Charged Particles." *J. Appl. Phys.* **30**, 342 (1959). DOI: 10.1063/1.1735165. See p. 5.

[39] H. Ikezi. "Coulomb solid of small particles in plasmas." *Phys. Fluids* **29**, 1764 (1986). DOI: 10.1063/1.865653. See p. 5.

[40] J. Chu and L. I. "Direct observation of Coulomb crystals and liquids in strongly coupled rf dusty plasmas." *Phys. Rev. Lett.* **72**, 4009–4012 (1994). DOI: 10.1103/PhysRevLett.72.4009. See p. 5.

[41] H. Thomas et al. "Plasma Crystal: Coulomb Crystallization in a Dusty Plasma." *Phys. Rev. Lett.* **73**, 652–657 (1994). See p. 5.

[42] Y. Hayashi and K. Tachibana. "Observation of Coulomb-Crystal Formation from Carbon Particles Grown in a Methane Plasma." *Jpn. J. Appl. Phys.* **33**, L804 –L806 (1994). DOI: 10.1143/JJAP.33.L804. See p. 5.

[43] A. Melzer, T. Trottenberg, and A. Piel. "Experimental determination of the charges on dust particles forming Coulomb lattices." *Phys. Lett. A* **191**, 301–308 (1994). DOI: 10.1016/0375-9601(94)90144-9. See pp. 5, 10.

[44] V. E. Fortov et al. "Shock wave formation in a dc glow discharge dusty plasma." *Phys. Rev. E* **71**, 036413 (2005). See p. 6.

[45] M. Rubin-Zuzic et al. "Kinetic development of crystallisation fronts in complex plasmas." *Nature Physics* **2**, 181 (2006). DOI: 10.1038/nphys242. See p. 6.

[46] C. A. Knapek et al. "Recrystallization of a 2D Plasma Crystal." *Phys. Rev. Lett.* **98**, 015004 (2007). DOI: 10.1103/PhysRevLett.98.015004. See p. 6.

[47] M. Mikikian et al. "Formation and behaviour of dust particle clouds in a radio-frequency discharge: results in the laboratory and under microgravity conditions." *New. J. Phys.* **5**, 19 (2003). DOI: 10.1088/1367-2630/5/1/319. See pp. 6, 15.

[48] H. M. Thomas et al. "Complex plasma laboratory PK-3 Plus on the International Space Station." *New J. Phys.* **10**, 033036 (2008). DOI: 10.1088/1367-2630/10/3/033036. See pp. 6, 8, 22, 31, 37, 40.

[49] J. C. Maxwell. "On Stresses in Rarified Gases Arising from Inequalities of Temperature." *Phil. Trans. Royal Soc. London* **170**, 231 –256 (1879). See pp. 6, 32.

[50] A. Einstein. "Zur Theorie der Radiometerkr/"afte." *Z. Physik* **27**, 1–6 (1924). DOI: 10.1007/BF01328006. See p. 6.

[51] H. Rothermel et al. "Gravity Compensation in Complex Plasmas by Application of a Temperature Gradient." *Phys. Rev. Lett.* **89**, 175001 (2002). DOI: 10.1103/PhysRevLett.89.175001. See pp. 6, 31, 80, 92.

[52] Novespace. *Private communications*. 2009. See p. 7.

[53] H. J. Rath. *ZARM Center of Applied Space Technology and Microgravity*. Online. Accessed on 9 March 2009. URL: http://www.zarm.uni-bremen.de/. See p. 7.

[54] N. Reinke and D. Gonzalez. *TEXUS - DLR*. Online. Accessed on 9 March 2009. URL: http://www.dlr.de/rd/desktopdefault.aspx/tabid-2282/3421_read-5228/. See p. 7.

[55] Novespace. *Website*. Online. URL: http://www.novespace.fr/. See p. 7.

[56] ESA. *European Users Guide to Low Gravity Platforms*. Online. URL: http://spaceflight.esa.int/users/index.cfm?act=default.page&level=1c&page=2130. See p. 7.

[57] G. E. Morfill et al. "Condensed Plasmas under Microgravity." *Phys. Rev. Lett.* **83**, 1598–1601 (1999). DOI: 10.1103/PhysRevLett.83.1598. See pp. 7, 29.

[58] A. P. Nefedov et al. "PKE-Nefedov: plasma crystal experiments on the International Space Station." *New Journ. Phys.* **5**, 33 (2003). DOI: 10.1088/1367-2630/5/1/333. See pp. 7, 8, 12.

[59] H. M. Thomas et al. "PKE-Nefedov—Complex Plasma Research on the International Space Station." *Micrograv. Sci. Technol.* **16**, 317 –321 (2005). DOI: 10.1007/BF02945998. See pp. 7, 8.

[60] V. E. Fortov et al. "Dusty plasma induced by solar radiation under microgravitational conditions: An experiment on board the Mir orbiting space station." *J. Exp. Theo. Phys.* **87**, 1087 –1097 (1998). DOI: 10.1134/1.558598. See pp. 8, 99.

[61] A. P. Nefedov et al. "The dynamics of macroparticles in a direct current glow discharge plasma under micro-gravity conditions." *New J. Phys.* **5**, 108 (2003). DOI: 10.1088/1367-2630/5/1/108. See p. 8.

[62] A. V. Ivlev et al. "Fluid Complex Plasmas—Studies at the Particle Level." *AIP Conf. Proc.* **982**, 577 –583 (2008). DOI: 10.1063/1.2897861. See pp. 8, 9.

[63] V. Nosenko and J. Goree. "Shear Flows and Shear Viscosity in a Two-Dimensional Yukawa System (Dusty Plasma)." *Phys. Rev. Lett.* **93**, 155004 (2004). DOI: 10.1103/PhysRevLett.93.155004. See pp. 9, 94.

[64] G. E. Morfill et al. "Highly resolved Fluid Flows: 'Liquid Plasmas' at the Kinetic Level." *Phys. Rev. Lett.* **92**, (2004). DOI: 10.1103/PhysRevLett.92.175004. See pp. 9, 10.

[65] *CRC Handbook of Chemistry and Physics*. Online. Accessed on 27/02/2009 and 8/4/2009. URL: http://www.hbcpnetbase.com/. See pp. 9, 101.

[66] D. Samsonov et al. "Mach Cones in a Coulomb Lattice and a Dusty Plasma." *Phys. Rev. Lett.* **83**, 3649–3652 (1999). DOI: 10.1103/PhysRevLett.83.3649. See p. 9.

[67] A. Melzer et al. "Laser-excited Mach cones in a dusty plasma crystal." *Phys. Rev. E* **62**, 4162 –4176 (2000). DOI: 10.1103/PhysRevE.62.4162. See p. 9.

[68] V. Nosenko et al. "Observation of Shear-Wave Mach Cones in a 2D Dusty-Plasma Crystal." *Phys. Rev. Lett* **88**, 135001 (2002). DOI: 10.1103/PhysRevLett.88.135001. See p. 9.

[69] R. Dgani and N. Soker. "Instabilities in Moving Planetary Nebulae." *Astrophys. J.* **495**, 337 –345 (1998). DOI: 10.1086/305257. See p. 9.

[70] G. E. Morfill et al. "From Fluid Flows to Crystallization: New Results from Complex Plasmas." *Physica Scripta* **T107**, 59–64 (2004). See pp. 9, 10.

[71] A. Melzer, M. Klindworth, and A. Piel. "Normal Modes of 2D Finite Clusters in Complex Plasmas." *Phys. Rev. Lett.* **87**, 115002 (2001). DOI: 10.1103/PhysRevLett.87.115002. See p. 10.

[72] A. Melzer. "Mode spectra of thermally excited two-dimensional dust Coulomb clusters." *Phys. Rev. E* **67**, 016411 (2003). DOI: 10.1103/PhysRevE.67.016411. See p. 10.

[73] T. Sheridan et al. "Breathing-mode resonance of a complex plasma disk." *Phys. Lett. A* **329**, 88 –93 (2004). DOI: 10.1016/j.physleta.2004.06.079. See p. 10.

[74] J. Goree et al. "Theory of dust voids in plasmas." *Phys. Rev. E* **59**, 7055–7067 (1999). DOI: 10.1103/PhysRevE.59.7055. See pp. 10, 63, 76.

[75] N. N. Rao, P. K. Shukla, and M. Y. Yu. "Dust-acoustic waves in dusty plasmas." *Planet. Space Sci.* **38**, 543–546 (1990). DOI: 10.1016/0032-0633(90)90147-I. See pp. 10, 11, 36.

[76] V. E. Fortov. "Overview of Ordered Dust Structures in Dusty Plasmas." *Physica Scripta* **T107**, 90–97 (2004). See p. 10.

[77] M. Rosenberg. "Ion-dust streaming instability in processing plasmas." *J. Vac. Sci. Technol. A* **14**, 631 –633 (1996). DOI: 10.1116/1.580157. See p. 10.

[78] N. D'Angelo and R. L. Merlino. "Current-driven dust-acoustic instability in a collisional plasma." *Planet. Space Sci.* **44**, 1593 –1598 (1996). DOI: 10.1016/S0032-0633(96)00069-4. See p. 10.

[79] A. Piel et al. "Obliquely Propagating Dust-Density Plasma Waves in the Presence of an Ion Beam." *Phys. Rev. Lett.* **97**, 205009 (2006). DOI: 10.1103/PhysRevLett.97.205009. See pp. 11–13, 51, 55, 63.

[80] R. L. Merlino et al. "Laboratory studies of waves and instabilities in dusty plasmas." *Phys. Plasmas* **5**, 1607 –1614 (1998). DOI: 10.1063/1.872828. See pp. 11, 12, 72.

[81] F. Melandsø. "Lattice waves in dust plasma crystals." *Phys. Plasmas* **3**, 3890–901 (1996). See p. 11.

[82] X. Wang, A. Bhattacharjee, and S. Hu. "Longitudinal and Transverse Waves in Yukawa Crystals." *Phys. Rev. Lett.* **86**, 2569 (2000). DOI: 10.1103/PhysRevLett.86.2569. See p. 11.

[83] S. Nunomura et al. "Wave Spectra in Solid and Liquid Complex (Dusty) Plasmas." *Phys. Rev. Lett.* **94**, 045001 (2005). DOI: 10.1103/PhysRevLett.94.045001. See p. 11.

[84] J. Pramanik et al. "Experimental Observations of Transverse Shear Waves in Strongly Coupled Dusty Plasmas." *Phys. Rev. Lett.* **88**, 175001 (2002). DOI: 10.1103/PhysRevLett.88.175001. See p. 11.

[85] A. Piel, V. Nosenko, and J. Goree. "Laser-excited shear waves in solid and liquid two-dimensional dusty plasmas." *Phys. Plasmas* **13**, 042104 (2006). DOI: 10.1063/1.2196327. See p. 11.

[86] M. Rosenberg. "Ion- and dust-acoustic instabilities in dusty plasmas." *Planet. Space Sci.* **41**, 229–233 (1993). DOI: 10.1016/0032-0633(93)90062-7. See p. 11.

[87] A. Barkan, R. L. Merlino, and N. D'Angelo. "Laboratory observation of the dust-acoustic wave mode." *Phys. Plasmas* **2**, 3563–3565 (1995). See pp. 11, 12, 27.

[88] G. Praburam and J. Goree. "Experimental observation of very low-frequency macroscopic modes in a dusty plasma." *Phys. Plasmas* **3**, 1212 (1996). DOI: 10.1063/1.871745. See p. 11.

[89] C. Thompson et al. "Dust acoustic waves in a direct current glow discharge." *Phys. Plasmas* **4**, 2331–2335 (1997). DOI: 10.1063/1.872238. See pp. 11, 12.

[90] V. I. Molotkov et al. "Dust acoustic waves in a dc glow-discharge plasma." *JETP* **89**, 477–480 (1999). DOI: 10.1134/1.559006. See pp. 11, 12, 54.

[91] S. Khrapak et al. "Compressional waves in complex (dusty) plasmas under microgravity conditions." *Phys. Plasmas* **10**, 1–4 (2003). DOI: 10.1063/1.1525283. See pp. 11–13, 59, 64, 72.

[92] M. Thoma et al. "Parabolic Flight Experiments with PK-4." *Microgravity sci. technol.* **18**, 47–50 (2006). See p. 11.

[93] V. V. Yaroshenko, H. M. Thomas, and G. E. Morfill. "Dust density waves in a complex plasma layer." *Phys. Plasmas* **14**, 082104 (2007). DOI: 10.1063/1.2768035. See p. 11.

[94] N. N. Rao. "Linear and nonlinear dust-acoustic waves in non-ideal dusty plasmas." *J. Plasma Physics* **59**, 561 –574 (1998). DOI: 10.1017/S0022377898006473. See p. 11.

[95] B. Eliasson and P. K. Shukla. "Dust acoustic shock waves." *Phys. Rev. E* **69**, 067401 (2004). DOI: 10.1103/PhysRevE.69.067401. See p. 11.

[96] J. B. Pieper and J. Goree. "Dispersion of Plasma Dust Acoustic Waves in the Strong-Coupling Regime." *Phys. Rev. Lett.* **77**, 3137 – 3140 (1996). DOI: 10.1103/PhysRevLett.77.3137. See pp. 11, 12.

[97] V. E. Fortov et al. "Dust-acoustic wave instability at the diffuse edge of radio frequency inductive low-pressure gas discharge plasma." *Phys. Plasmas* **10**, 1199 (2003). DOI: 10.1063/1.1563667. See pp. 11, 12.

[98] S. V. Annibaldi et al. "Dust-acoustic dispersion relation in three-dimensional complex plasmas under microgravity." *New J. Phys.* **9**, 327 (2007). DOI: 10.1088/1367-2630/9/9/327. See pp. 11, 12, 36, 63, 71, 72.

[99] H. R. Prabhakara and V. L. Tanna. "Trapping of dust and dust acoustic waves in laboratory plasmas." *Phys. Plasmas* **3**, 3176 (1996). DOI: 10.1063/1.871620. See p. 11.

[100] E. Thomas and R. L. Merlino. "Dust particle motion in the vicinity of dust acoustic waves." *IEEE Trans. Plasma Sci.* **29**, 152–157 (2001). DOI: 10.1109/27.923685. See pp. 11, 12.

[101] V. E. Fortov et al. "Large-amplitude dust waves excited by the gas-dynamic impact in a dc glow discharge plasma." *Phys. Rev. E* **69**, 016402 (2004). DOI: 10.1103/PhysRevE.69.016402. See pp. 11, 12.

[102] E. Thomas, Jr. "Measurements of spatially growing dust acoustic waves in a dc glow discharge plasma." *Phys. Plasmas* **13**, 042107 (2006). DOI: 10.1063/1.2193540. See pp. 11, 12.

[103] E. Thomas Jr., R. Fisher, and R. L. Merlino. "Observations of dust acoustic waves driven at high frequencies: Finite dust temperature effects and wave interference." *Phys. Plasmas* **14**, 123701 (2007). DOI: 10.1063/1.2815795. See pp. 11–13.

[104] P. Bandyopadhyay et al. "Experimental observation of strong coupling effects on the dispersion of dust acoustic waves in a plasma." *Phys. Lett. A* **368**, 491 –494 (2007). DOI: 10.1016/j.physleta.2007.04.048. See p. 11.

[105] J. H. Chu, J.-B. Du, and L. I. "Coulomb solids and low-frequency fluctuations in RF dusty plasmas." *J. Phys. D: Appl. Phys.* **27**, 296–300 (1994). DOI: 10.1088/0022-3727/27/2/018. See pp. 11, 12.

[106] T. Trottenberg, D. Blick, and A. Piel. "Dust confinement and dust-acoustic waves in weakly magnetized anodic plasmas." *Phys. Plasmas* **13**, 042105 (2006). DOI: 10.1063/1.2196347. See pp. 11, 12.

[107] M. Schwabe et al. "Highly resolved self-excited density waves in a complex plasma." *Phys. Rev. Lett.* **99**, 095002 (2007). DOI: 10.1103/PhysRevLett.99.095002. See pp. 12, 52, 127.

[108] V. A. Vasiliev et al. *Autowave Processes in Kinetic Systems*. Ed. by M. Hazewinkel. VEB Deutscher Verlag der Wissenschaften, 1987. See p. 11.

[109] L. B. Zuev et al. "On a New Type of Plastic Deformation Waves in Solids." *Russian Phys J* **44**, 169–177 (2001). DOI: 10.1023/A:1011321903620. See pp. 11, 13, 53.

[110] N. Garnier and A. Chiffaudel. "Nonlinear Transition to a Global Mode for Traveling-Wave Instability in a Finite Box." *Phys. Rev. Lett.* **86**, 75–78 (2001). DOI: 10.1103/PhysRevLett.86.75. See pp. 11, 13.

[111] J. Kr/'asa, R. M. Perkin, and L. Pekárek. "The evolution from regular to irregular motion of ionization waves in neon." *J. Phys. D: Appl. Phys.* **7**, 2541 –2544 (1974). See p. 11.

[112] S. J. M. H. Hulscher and C. M. Dohmen-Janssen. "Introduction of special section on Marine Sand Wave and River Dune Dynamics." *J. Geophys. R.* **110**, F04S01 (2005). DOI: doi:10.1029/2005JF000404. See p. 11.

[113] H. Nishimori and N. Ouchi. "Formation of ripple patterns and dunes by wind-blown sand." *PRL* **71**, 197–200 (1993). DOI: 10.1103/PhysRevLett.71.197. See p. 11.

[114] G. Sauermann, K. Kroy, and H. J. Herrmann. "Continuum saltation model for sand dunes." *Phys. Rev. E* **64**, 031305 (2001). See p. 11.

[115] P. Barnard. *Giant Underwater Sand Waves Seaward of the Golden Gate Bridge*. online. Accessed on 8 April 2009. Sept. 2006. URL: http://soundwaves.usgs.gov/2006/09/research.html. See p. 13.

[116] N. D'Angelo. "Coulomb solids and low-frequency fluctuations in RF dusty plasmas." *J. Phys. D: Appl. Phys.* **28**, 1009–1010 (1995). DOI: 10.1088/0022-3727/28/5/024. See p. 11.

[117] V. E. Fortov et al. "Mechanism of dust-acoustic instability in a direct current glow discharge plasma." *Phys. Plasmas* **7**, 1374–1380 (2000). DOI: 10.1063/1.873954. See pp. 11, 54.

[118] H. Thomas. *Private communications*. 2009. See pp. 12, 97.

[119] P. Lenard. "Über Regen." *Meteorol. Zeitschr.* 249 (1904). See p. 14.

[120] A. Wierzba. "Deformation and breakup of liquid drops in a gas stream at nearly critical Weber numbers." *Exp. Fluids* **9**, 59 –4 (1990). DOI: 10.1007/BF00575336. See p. 14.

[121] G. Machu et al. "Coalescence, torus formation and breakup of sedimenting drops: experiments and computer simulations." *J. Fluid Mech.* **447**, 299–336 (2001). DOI: 10.1017/S0022112001005882. See p. 14.

[122] D. Joseph, J. Belanger, and G. Beavers. "Breakup of a liquid drop suddenly exposed to a high-speed airstream." *International Journal of Multiphase Flow* **25**, 1263–1303 (1999). See pp. 14, 90.

[123] M. Pilch and C. A. Erdmann. "Use of breakup time data and velocity history data to predict the maximum size of stable fragments for acceleration-induced breakup of a liquid drop." *Int. Journal Multiphase Flow* **13**, 741 –757 (1987). DOI: 10.1016/0301-9322(87)90063-2. See pp. 14, 84.

[124] S. I. Han, S. Stapf, and B. Blümich. "NMR Imaging of Falling Water Drops." *Phys. Rev. Lett.* **87**, 144501 (2001). DOI: 10.1103/PhysRevLett.87.144501. See pp. 14, 90.

[125] J. M. Nitsche and G. K. Batchelor. "Break-up of a falling drop containing dispersed particles." *J. Fluid Mech.* **340**, 161–175 (1997). See pp. 14, 85, 90.

[126] J. F. Davidson, D. Harrison, and J. R. F. G. de Carvalho. "On the Liquidlike Behavior of Fluidized Beds." *Ann. Rev. Fluid Mech.* **9**, 55–86 (1977). See p. 15.

[127] G. K. Batchelor and J. M. Nitsche. "Expulsion of particles from a buoyant blob in a fluidized bed." *J. Fluid Mech.* **278**, 63 –81 (1994). DOI: 10.1017/S0022112094003617. See p. 15.

[128] H. R. Snyder, R. P. Currier, and M. S. Murillo. "Plasma fluidized bed imaging and possible strong coupling effects." *Appl. Phys. Lett.* **76**, 2511 (2000). DOI: 10.1063/1.126392. See p. 15.

[129] D. Savignac and P. Leiderer. "Charge-Induced Instability of the 4He Solid-Duperfluid Interface." *Phys. Rev. Lett.* **49**, 1869 (1982). See p. 15.

[130] O. Arp et al. "Dust Coulomb Balls: Three-Dimensional Plasma Crystals." *Phys. Rev. Lett.* **93**, 165004 (2004). DOI: 10.1103/PhysRevLett.93.165004. See pp. 15, 31.

[131] B. M. Annaratone et al. "Complex-plasma manipulation by radiofrequency biasing." *Plasma Phys. Control. Fusion* **46**, B495 –B509 (2004). DOI: 10.1088/0741-3335/46/12B/041. See p. 15.

[132] T. Antonova et al. "Measurement of the Interaction Force among Particles in Three-Dimensional Plasma Clusters." *Phys. Rev. Lett.* **96**, 115001 (2006). DOI: 10.1103/PhysRevLett.96.115001. See p. 15.

[133] A. D. Usachev et al. "Formation of a Boundary-Free Dust Cluster in a Low-Pressure Gas-Discharge Plasma." *Phys. Rev. Lett.* **102**, 045001 (2009). DOI: 10.1103/PhysRevLett.102.045001. See p. 15.

[134] U. Konopka et al. "Complex Plasmas in Strong Magnetic Field Environments." In: *AIP Conference Proceedings*. Vol. 799. 2005, 181–184. DOI: 10.1063/1.2134595. See p. 15.

[135] H.-Y. Chu et al. "Observation of Laser-Pulse-Induced Travelling Microbubbles in Dusty Plasma Liquids." *Phys. Rev. Lett.* **90**, 075004 (2003). DOI: 10.1103/PhysRevLett.90.075004. See p. 15.

[136] M. Schwabe et al. "Formation of Bubbles, Blobs, and Surface Cusps in Complex Plasmas." *Phys. Rev. Lett.* **102**, 255005 (2009). DOI: 10.1103/PhysRevLett.102.255005. See pp. 17, 76, 78, 79, 127.

[137] D. Bohm. "Minimum Kinetic Energy for a Stable Sheath." In: *The Characteristics of Electrical Discharges in Magnetic Fields*. Ed. by A. Guthrie and R. Wakerling. New York: McGraw-Hill Book Company, Inc., 1949, 77–86. See p. 21.

[138] V. E. Fortov et al. "Dusty plasmas." *Physics - Uspekhi* **47**, 447 –492 (2004). DOI: 10.1070/PU2004v047n05ABEH001689. See pp. 21, 23, 27, 34.

[139] A. Ganguli and R. D. Tarey. "Understanding plasma sources." *Current Science* **83**, 279 (2002). See p. 22.

[140] M. Klindworth, O. Arp, and A. Piel. "Langmuir probe diagnostics in the IMPF device and comparison with simulations and tracer particle experiments." *J. Phys. D: Appl. Phys.* **39**, 1095–1104 (2006). DOI: 10.1088/0022-3727/39/6/015. See pp. 22, 59.

[141] V. N. Tsytovich, G. E. Morfill, and H. M. Thomas. "Complex Plasmas: I. Complex Plasmas as Unusual State of Matter." *Plasma Phys. Rep.* **28**, 623–651 (2002). See pp. 22, 23.

[142] O. Havnes, G. E. Morfill, and C. K. Goertz. "Plasma potential and grain charges in a dust cloud embedded in a plasma." *J. Geophys. Res.* **89**, 10999 –11003 (1984). See pp. 22, 60.

[143] V. N. Tsytovich and U. de Angelis. "Kinetic theory of dusty plasmas II. Dust–plasma particle collision integrals." *Phys. Plasmas* **7**, 554 (2000). DOI: 10.1063/1.873841. See p. 23.

[144] P. Ricci et al. "Plasma kinetics in dusty plasmas." *Phys. Plasmas* **8**, 769 (2001). DOI: 10.1063/1.1344197. See p. 23.

[145] A. Bouchoule et al. *Dusty Plasmas*. John Wiley & Sons Ltd., 1999. See p. 23.

[146] G. Morfill, A. V. Ivlev, and J. R. Jokipii. "Charge Fluctuation Instability of the Dust Lattice Wave." *Phys. Rev. Lett.* **83**, 971 –974 (1999). DOI: 10.1103/PhysRevLett.83.971. See p. 23.

[147] A. V. Ivlev, U. Konopka, and G. Morfill. "Influence of charge variation on particle oscillations in the plasma sheath." *Phys. Rev. E* **62**, 2739 –2744 (2000). DOI: 10.1103/PhysRevE.62.2739. See p. 23.

[148] H. Mott-Smith and I. Langmuir. "The theory of collectors in gaseous discharges." *Phys. Rev* **28**, 727 (1926). DOI: 10.1103/PhysRev.28.727. See p. 24.

[149] D. Bohm. "The Characteristics of Electrical Discharges in Magnetic Fields." In: ed. by A. Guthrie and R. K. Wakerling. McGraw-Hill Book Company, 1949. Chap. 3. See p. 24.

[150] I. B. Bernstein and I. N. Rabinowitz. "Theory of electrostatic probes in a low-density plasma." *Phys. Fluids* **2**, 112 (1959). DOI: 10.1063/1.1705900. See p. 24.

[151] J. D. Swift and M. R. J. Schwar. *Electrical probes for plasma diagnostics*. London: ILIFFE Books, 1970. See pp. 24, 60, 71.

[152] J. G. Lafromboise and L. W. Parker. "Probe design for orbit-limited current collection." *Phys. Fluids* **16**, 629 (1973). DOI: 10.1063/1.1694398. See p. 24.

[153] T. Matsoukas and M. Russel. "Particle charging in low-pressure plasmas." *J. Appl. Phys.* **77**, 4285–4292 (1995). DOI: 10.1063/1.359451. See pp. 24, 25, 60, 71.

[154] S. A. Khrapak et al. "Particle charge in the bulk of gas discharges." *Phys. Rev. E* **72**, 016406 (2005). DOI: 10.1103/PhysRevE.72.016406. See p. 25.

[155] B. M. Annaratone, M. W. Allen, and J. E. Allen. "Ion currents to cylindrical Langmuir probes in RF plasmas." *J. Phys. D: Appl. Phys.* **25**, 417 –424 (1992). DOI: 10.1088/0022-3727/25/3/012. See p. 25.

[156] M. Lampe et al. "Trapped ion effect on shielding, current flow, and charging of a small object in a plasma." *Phys. Plasmas* **10**, 1500 (2003). DOI: 10.1063/1.1562163. See p. 26.

[157] G. E. Morfill et al. "The 'classical tunnelling effect' - observations and theory." *New J. Phys.* **8**, 7 (2006). DOI: 10.1088/1367-2630/8/1/007. See pp. 26, 31, 60, 71.

[158] S. Khrapak and G. Morfill. "Basic Processes in Complex (Dusty) Plasmas: Charging, Interactions, and Ion Drag Force." *Contrib. Plasmas Phys.* **49**, 148 –168 (2009). DOI: 10.1002/ctpp.200910018. See p. 26.

[159] J. E. Allen, R. L. F. Boyd, and P. Reynolds. "The collection of positive ions by a probe immersed in a plasma." *Proc. Phys. Soc.* **B70**, 297 –304 (1957). See pp. 26, 71.

[160] C. M. C. Nairn, B. M. Annaratone, and J. E. Allen. "On the theory of spherical probes and dust grains." *Plasma Sources Sci. Technol.* **7**, 478–490 (1998). DOI: 10.1088/0963-0252/7/4/006. See p. 26.

[161] R. V. Kennedy and J. E. Allen. "The floating potential of spherical probes and dust grains. Part 1. Radial motion theory." *J. Plasma Phys.* **67**, 243–250 (2002). DOI: 10.1017/S0022377802001691. See pp. 26, 60, 71.

[162] J. E. Daugherty, R. K. Porteous, and D. B. Graves. "Electrostatic forces on small particles in low-pressure discharges." *J. Appl. Phys.* **73**, 1617 (1993). DOI: 10.1063/1.353194. See p. 27.

[163] V. E. Fortov et al. "Crystallization of a dusty plasma in the positive column of a glow discharge." *JETP Lett.* **64**, 92–98 (1996). DOI: 10.1134/1.567149. See p. 27.

[164] U. Konopka. *Wechselwirkungen geladener Staubteilchen in Hochfrequenzplasmen*. PhD thesis. Ruhr-Universität-Bochum, 2000. See pp. 27, 28, 35.

[165] U. Konopka. "Dynamics and Structure of Complex Plasmas in Magnetic Fields." In: *11th Workshop on the Physics of Dusty Plasmas*. 2006. See p. 28.

[166] P. Epstein. "On the resistance experienced by spheres in their motion through gases." *Phys. Rev.* **23**, 710–733 (1924). See pp. 28, 58, 74.

[167] B. Liu, J. Goree, and V. Nosenko. "Radiation pressure and gas drag forces on a melamine-formaldehyde microsphere in a dusty plasma." *Phys. Plasmas* **10**, 9–20 (2003). DOI: 10.1063/1.1526701. See p. 28.

[168] T. G. Northrop and T. J. Birmingham. "Plasma drag on a dust grain due to Coulomb collisions." *Planet. Space Sci.* **38**, 319 –326 (1989). DOI: 10.1016/0032-0633(90)90096-9. See p. 29.

[169] M. S. Barnes et al. "Transport of Dust Particles in Glow-Discharge Plasmas." *Phys. Rev. Lett.* **68**, 313–316 (1992). DOI: 10.1103/PhysRevLett.68.313. See p. 29.

[170] S. A. Khrapak et al. "Ion drag force in complex plasmas." *Phys. Rev. E* **66**, (2002). See pp. 29, 30.

[171] A. V. Ivlev et al. "Ion drag force in dusty plasmas." *Plasma Phys. Control. Fusion* **46**, B267–B279 (2004). See p. 29.

[172] M. H. Thoma et al. "Measurement of the ion drag force in a complex dc-plasma using the PK-4 experiment." *Ukr. J. Phys.* **50**, 179–183 (2005). URL: http://www.ujp.bitp.kiev.ua/files/papers/500215p.pdf. See p. 30.

[173] S. A. Khrapak et al. "Scattering in the Attractive Yukawa Potential in the Limit of Strong Interaction." *Phys. Rev. Lett.* **90**, 225002 (2003). DOI: 10.1103/PhysRevLett.90.225002. See p. 30.

[174] V. Nosenko et al. "Measurement of the ion drag force in a collisionless plasma with strong ion-grain coupling." *Phys. Plasmas* **14**, 103702 (2007). DOI: 10.1063/1.2783221. See p. 30.

[175] A. V. Ivlev et al. "Kinetic approach for the ion drag force in a collisional plasma." *Phys. Rev. E* **71**, (2005). DOI: 10.1103/PhysRevE.71.016405. See p. 30.

[176] S. A. Khrapak and G. E. Morfill. "Dusty plasmas in a constant electric field: Role of the electron drag force." *Phys. Rev. E* **69**, (2004). DOI: 10.1103/PhysRevE.69.066411. See p. 30.

[177] J. Aitken. "On the formation of small clear spaces in dusty air." *Trans. R. Soc. Edinb.* **32**, 239–22 (1884). See p. 30.

[178] F. Zheng. "Thermophoresis of spherical and non-spherical particles: a review of theories and experiments." *Adv. Colloid Interface Sci.* **97**, 253–276 (2002). DOI: 10.1016/S0001-8686(01)00067-7. See pp. 30, 31.

[179] R. N. Varney. "Drift Velocities of Ions in Krypton and Xenon." *Phys. Rev.* **88**, 362–364 (1952). DOI: 10.1103/PhysRev.88.362. See pp. 31, 35.

[180] L. Waldmann. "Über die Kraft eines inhomogenen Gases auf kleine suspendierte Kugeln." *Z. Naturforschung* **14A**, 589 –599 (1959). See p. 31.

[181] M. A. Gallis, D. J. Rader, and J. R. Torczynski. "Thermophorsis in Rarefied Gas Flows." *Aerosol Sci. Techn.* **36**, 1099 –1117 (2002). DOI: 10.1080/02786820290092168. See p. 31.

[182] L. Couëdel et al. "Residual dust charges in discharge afterglow." *Phys. Rev. E* **74**, 026403 (2006). DOI: 10.1103/PhysRevE.74.026403. See pp. 31, 32.

[183] M. Rubin-Zuzic et al. "Circulation dynamo in complex plasma." *New J. Phys.* **9**, 39 (2007). DOI: 10.1088/1367-2630/9/2/039. See pp. 31, 57, 74, 76.

[184] M. Kroll et al. "Digital in-line holography of dusty plasmas." *Phys. Plasmas* **15**, 063703 (2008). DOI: 10.1063/1.2932109. See p. 31.

[185] S. Mitic et al. "Convective Dust Clouds Driven By Thermal Creep in a Complex Plasma." *Phys. Rev. Lett.* **101**, 235001 (2008). DOI: 10.1103/PhysRevLett.101.235001. See pp. 31, 32, 91.

[186] R. Heidemann et al. "Dissipative Dark Soliton in a Complex Plasma." *Phys. Rev. Lett.* **102**, 135002 (2009). DOI: 10.1103/PhysRevLett.102.135002. See pp. 31, 98.

[187] R. M. Smoluchowski von Smolan. "Ueber Wärmeleitung in verdünnten Gasen." *Ann. Phy.* **300**, 101 –130 (1898). DOI: 10.1002/andp.18983000110. See p. 32.

[188] P. Lasareff. "Über den Temperatursprung an der Grenze zwischen Metall und Gas." *Ann. Phys.* **342**, 233 –246 (1911). DOI: 10.1002/andp.19123420203. See p. 32.

[189] L. S. Pan et al. "Determination of temperature jump coeffcient using the direct simulation Monte Carlo method." *J. Micromech. Microeng.* **12**, 41 –52 (2002). DOI: 10.1088/0960-1317/12/1/307. See pp. 32, 92, 93.

[190] H. Vestner. "Forces on Small Particles in Nonhomogeneou s Polyatomic Gases." *Z. Naturforsch.* **29a**, 1244 –1252 (1974). See p. 32.

[191] E. H. Kennard. *Kinetic Theory of Gases*. New York: McGraw-Hill Book Company, 1938, 327. See pp. 32, 91.

[192] Y. Sone. "Flows induced in a rarefied gas and their ghost effect on the behavior of a gas in the continuum limit." *Annu. Rev. Fluid Mech.* **32**, 779 –811 (2000). See p. 32.

[193] O. Reynolds. "On certain Dimensional Properties of Matter in the Gaseous State." *Phil. Trans. R. Soc. Lond.* **170**, 727 –845 (1879). DOI: 10.1098/rstl.1879.0078. See p. 32.

[194] S. P. Bakanov. "Thermophoresis in gases at small Knuden numbers." *Sov. Phys. Usp.* **35**, 783–792 (1992). DOI: 10.1070/PU1992v035n09ABEH002263. See p. 32.

[195] V. N. Tsytovich. "Dust plasma crystals, drops, and clouds." *Phys.-Usp.* **40**, 53 –94 (1997). DOI: 10.1070/PU1997v040n01ABEH000201. See p. 34.

[196] S. A. Khrapak and G. E. Morfill. "Grain surface temperature in noble gas discharges: Refined analytical model." *Phys. Plasmas* **13**, 104506 (2006). DOI: 10.1063/1.2359282. See pp. 34, 99.

[197] M. Nambu, S. V. Vladimirov, and P. K. Shukla. "Attractive forces between charged particulates in plasmas." *Phys. Lett. A* **203**, 40–42 (1995). DOI: 10.1016/0375-9601(95)00380-L. See p. 34.

[198] M. Lampe, G. Joyce, and G. Ganguli. "Interactions between dust grains in a dusty plasma." *Phys. Plasmas* **7**, 3851–3861 (2000). DOI: 10.1063/1.1288910. See p. 34.

[199] A. Melzer, V. A. Schweigert, and A. Piel. "Transition from Attractive to Repulsive Forces between Dust Molecules in a Plasma Sheath." *Phys. Rev. Lett.* **83**, 3194–3197 (1999). DOI: 10.1103/PhysRevLett.83.3194. See p. 34.

[200] R. Kompaneets et al. "Dust clusters with non-Hamiltonian particle dynamics." *Phys. Plasmas* **13**, 072104 (2006). DOI: 10.1063/1.2212396. See p. 34.

[201] A. V. Ivlev et al. "First Observation of Electrorheological Plasmas." *Phys. Rev. Lett.* **100**, 095003 (2008). DOI: 10.1103/PhysRevLett.100.095003. See p. 35.

[202] M. Schwabe et al. *Fast PK-3 Plus Experimental Safety and Data Package*. Perpared for the 13th DLR parabolic flight campaign. Feb. 2009. See p. 39.

[203] *Website*. URL: http://www.microparticles.de. See p. 39.

[204] U. Konopka. *Private communications*. 2007. See p. 43.

[205] Y. Feng, J. Goree, and B. Liu. "Accurate particle position measurement from images." *Rev. Sci. Instrum.* **78**, 053704 (2007). DOI: 10.1063/1.2735920. See pp. 45–47.

[206] Y. Ivanov and A. Melzer. "Particle positioning techniques for dusty plasma experiments." *Rev. Sci. Instrum.* **78**, 033506 (2007). DOI: 10.1063/1.2714050. See pp. 45, 46.

[207] A. Piel, M. Klindworth, and A. Melzer. "Obliquely propagating dust-density waves." *Phys. Rev. E* **77**, 026407 (2008). DOI: 10.1103/PhysRevE.77.026407. See p. 50.

[208] K. Menzel et al. "Structure and dynamics of dust density waves under microgravity." In: *12th Workshop on the Physics of Dusty Plasmas*. Boulder, CO 2009. See p. 50.

[209] O. Arp et al. "Experimental Investigation of Dust Density Waves and Plasma Glow." In: *12th Workshop on the Physics of Dusty Plasmas*. Boulder, CO 2009. See p. 50.

[210] K. Menzel. *Private communications*. at WPDP 12. May 2009. See p. 51.

[211] M. Schwabe. *Website*. 2007. URL: http:/www.mpe.mpg.de/~mschwabe/waves.html. See p. 58.

[212] J. Wang et al. "A new approach to modelling the effective thermal conductivity of heterogeneous materials." *Int. J Heat a. Mass Transf.* **49**, 3075–3083 (2006). DOI: 10.1016/j.ijheatmasstransfer.2006.02.007. See p. 59.

[213] G. H. P. M. Swinkels et al. "Microcalorimetry of dust particles in a radio-frequency plasma." *J. Appl. Phys.* **88**, 1747–1755 (2000). DOI: 10.1063/1.1302993. See pp. 59, 99.

[214] M. Schwabe et al. "Nonlinear waves externally excited in a complex plasma under microgravity conditions." *New J. Phys.* **10**, 033037 (2008). DOI: 10.1088/1367-2630/10/3/033037. See pp. 61, 127.

[215] M. Mikikian et al. "Self-excited void instability in dusty plasmas: plasma and dust cloud dynamics during the heartbeat instability." *New J. Phys.* **9**, 268 (2007). DOI: 10.1088/1367-2630/9/8/268. See p. 63.

[216] M. Schwabe. *Website*. 2007. URL: http:/www.mpe.mpg.de/~mschwabe/isswaves.html. See p. 64.

[217] I. V. I. Solutions. *IDL 7.0 Manual*. 2008. See p. 67.

[218] B. Cabral and L. C. Leedom. "Imaging vector fields using line integral convolution." In: *Proceedings of the 20th annual conference on Computer graphics and interactive techniques*. 1993. See p. 90.

[219] M. Galloy. *Website*. 2008. URL: http://michaelgalloy.com. See p. 90.

[220] N. M. Zubarev. "Formation of Conic Cusps at the Surface of Liquid Metal in Electric Field." *JETP Lett.* **73**, 544 –548 (2001). DOI: 10.1134/1.1387524. See pp. 90, 91.

[221] S. Chandrasekhar. *Hydrodynamic and Hydromagnetic Stability*. Ed. by W. Marshall and D. H. Wilkinson. International Series of Monographs on Physics. Oxford University Press, 1961. See pp. 91, 93.

[222] C. P. Royall et al. "Noneqiulibrium Sedimentation of Colloid on the Particle Scale." *Phys. Rev. Lett.* **98**, 188304 (2007). DOI: 10.1103/PhysRevLett.98.188304. See p. 93.

[223] A. Wysocki et al. "Direct observation of hydrodynamic instabilities in a driven non-uniform colloidal dispersion." *Soft Matter* **5**, 1340–1344 (2009). DOI: 10.1039/b821250c. See p. 93.

[224] R. E. Duff, F. H. Harlow, and C. W. Hirt. "Effects of Diffusion on Interface Instability between Gases." *Phys. Fluids* **5**, 417 (1962). DOI: 10.1063/1.1706634. See p. 93.

[225] E. M. Lifshitz and L. Pitaevskii. *Physical Kinetics*. Ed. by L. D. Landau and E. M. Lifshitz. Pergamon Press, Oxford, 1981. See p. 94.

[226] J. J. Thompson. "On the structure of the atom." *Philos. Mag.* **7**, 237 –265 (1904). See p. 94.

[227] H. Totsuji et al. "Structure of spherical Yukawa clusters: A model for dust particles in dusty plasmas in an isotropic environment." *Phys. Rev. E* **72**, 036406 (2005). DOI: 10.1103/PhysRevE.72.036406. See p. 94.

[228] W.-T. Juan et al. "Observation of dust Coulomb clusters in a plasma trap." *Phys. Rev. E* **58**, R6947 –R6950 (1998). DOI: 10.1103/PhysRevE.58.R6947. See p. 94.

[229] J.-T. Jeong and H. K. Moffat. "Free-surface cusps associated with flow at low Reynolds number." *J. Fluid Mech.* **241**, 1–22 (1992). DOI: 10.1017/S0022112092001927. See p. 94.

[230] X. Cheng et al. "Towards the zero-surface-tension limit in granular fingering instability." *Nature Phys.* **4**, 234 –237 (2008). DOI: 10.1038/nphys834. See p. 94.

[231] A. V. Ivlev, S. K. Zhdanov, and G. E. Morfill. "Free Thermal Convection in Complex Plasma with Background-Gas Fraction." *Phys. Rev. Lett.* **99**, 135004 (2007). DOI: 10.1103/PhysRevLett.99.135004. See p. 94.

[232] P. B. Barber, D. A. Swift, and B. A. Tozer. "Time resolved Schlieren and interferometer studies of a low pressure discharge." *Brit. J. Appl. Phys.* **14**, 207 –211 (1963). DOI: 10.1088/0508-3443/14/4/312. See p. 98.

[233] S. Zhdanov. *Private communications*. 2009. See p. 98.

[234] C.-T. Liao et al. "Lagrangian-Eulerian Micromotion and Wave Heating in Nonlinear Self-Excited Dust-Acoustic Waves." *Phys. Rev. Lett.* **100**, 185004 (2008). DOI: 10.1103/PhysRevLett.100.185004. See p. 98.

[235] S. Zhdanov et al. "Electromechanical Effect in Complex Plasmas." *arXiv*, 0809.2663v1 (2008). See p. 98.

[236] E. C. Whipple. "Potentials of surfaces in space." *Rep. Prog. Phys.* **44**, 1197 –1250 (1981). DOI: 10.1088/0034-4885/44/11/002. See pp. 99, 100.

[237] J. Goree. "Charging of particles in a plasma." *Plasma Sources Sci. Technol.* **3**, 400 –406 (1994). DOI: 10.1088/0963-0252/3/3/025. See p. 99.

[238] B. Walch, M. Horányi, and S. Robertson. "Charging of Dust Grains in Plasma with Energetic Electrons." *Phys. Rev. Lett.* **75**, 838 –841 (1995). DOI: 10.1103/PhysRevLett.75.838. See p. 99.

[239] A. P. Nefedov et al. "Formation of Liquidlike and Crystalline Structures in Dusty Plasmas." *JETP Letters* **72**, 218 –226 (2000). See p. 99.

[240] S. V. Vladimirov, K. Ostrikov, and A. A. Samarian. *Physics and applications of complex plasmas*. Imperial College Press, 2005. See p. 99.

[241] M. R. Akdim and W. J. Goedheer. "Modeling the effect of dust on the plasma parameters in a dusty argon discharge under microgravity." *Phys. Rev. E* **67**, 066407 (2003). DOI: 10.1103/PhysRevE.67.066407. See p. 100.

[242] V. E. Fortov et al. "Emission properties and structural ordering of strongly coupled dust particles in a thermal plasma." *Phys. Lett. A* **219**, 89 –94 (1996). DOI: 10.1016/0375-9601(96)00464-1. See p. 100.

[243] J. Winter, V. E. Fortov, and A. P. Nefedov. "Radioactive dust levitation and its consequences for fusion devices." *J. Nucl. Mat.* **290 - 293**, 509 –512 (2001). DOI: 10.1016/S0022-3115(00)00524-9. See p. 100.

[244] *FEMLAB 3 Documentation*. Comsol. See p. 101.

Curriculum vitae

Mierk Anne Britt Schwabe

Personal data

Address	Mathilde-Boyen-Str. 4 80939 München Germany
E-Mail	mierk.schwabe@gmx.de
Birth date	October 15, 1980 in Preetz, Germany
Nationality	German

Research

08/2006–today	PhD student, MPE, Garching, Germany Topic: *Dynamical effects in fluid complex plasmas*
05/2005–05/2006	Diploma student, MPE, Garching, Germany Topic: *Microparticles as Probes in a Highly Magnetized Plasma*

Education

09/2006–today	LMU München, Munich, Germany - Physics (PhD)
10/2000–09/2006	TU München, Munich, Germany - Physics (Diploma)
09/2003–07/2004	Université Pierre et Marie Curie, Paris, France - Physics, Computer Science
08/1998–06/2000	Gymnasium Altenholz, Altenholz, Germany - Abitur
09/1997–07/1998	Washington-Lee High School, Arlington, VA, USA
08/1991–06/1997	Gymnasium Altenholz, Altenholz, Germany

Awards

2008	Best Student Poster Presentation, EPS Conference on Plasma Physics
2007	Best Student Poster Presentation, IPELS Conference

2000	Bookprize of the German Physical Society for Special Accomplishments in Physics
1998	1st Prize of the Space Settlement Design Contest by the NASA Ames Research Center

Teaching Experience

2007–today	Supervision of student lab experiments on plasma crystals at the Technical University Munich

Munich, August 2009

Publications

Refereed journal articles

- M. Schwabe, M. Rubin-Zuzic, S. Zhdanov, H. M. Thomas, and G. E. Morfill. *Highly Resolved Self-Excited Density Waves in a Complex Plasma*, Physical Review Letters, Vol. **99**, 095002 (2007) [107]
- M. Schwabe, S.K. Zhdanov, H.M. Thomas, A.V. Ivlev, M. Rubin-Zuzic, G.E. Morfill, V.I. Molotkov, A.M. Lipaev, V.E. Fortov, and T. Reiter. *Nonlinear waves externally excited in a complex plasma under microgravity conditions*, New Journal of Physics, Vol. **10**, 033037 (2008) [214]
- M. Schwabe, M. Rubin-Zuzic, S. Zhdanov, A. V. Ivlev, H. M. Thomas, and G. E. Morfill. *Formation of bubbles, blobs, and surface cusps in fluid complex plasmas*, Physical Review Letters, Vol. **102**, 255005 (2009) [136]

Contributions to international conferences and workshops

- 9th International Workshop on the Interrelationship between Plasma Experiments in Laboratory and Space, Palm Cove, Australia. August 2007. Poster presented: *Self-excited density waves in a complex plasma under the influence of thermophoresis.* Winner of student prize for the best poster presentation.
- Workshop on the Physics of Complex Plasmas, The University of Sydney, Sydney, Australia. August 2007. Talk presented: *Self-excited dust density waves*
- Dusty Plasmas In Applications, Odessa, Ukraine, August 2007. Talk presented: *Density Waves Self-Excited in a Complex Plasma.*
- 5th International Conference on Physics of Dusty Plasmas, Ponta Delgada, Azores, Portugal. May 2008. Poster presented: *Waves In Complex Plasmas: From "Hyper-gravity" To Microgravity.*
- 35th EPS Plasma Physics Conference, Hersonissos, Crete, Greece, June 2008. Poster presented: *Dust Waves in Complex Plasmas Under Microgravity Conditions.* Winner of student prize for the best poster presentation.
- DLR – MPE Symposium, Garching, Germany. November 2008. Talk presented: *Bubbles, blobs, and surface cusps in fluid complex plasmas.*
- 12th Workshop on the Physics of Dusty Plasmas, Boulder, Colorado, USA, May 2009. Talk presented: *Bubbles, Blobs, and Surface Cusps in Liquid Complex Plasmas.*

Acknowledgments

The work presented in this thesis would not have been possible without the support and guidance of many people, whom I would like to thank with all my heart.

First of all, my supervisor, Prof. Gregor Morfill, made everything possible by providing the opportunity to work in the Theory and Complex Plasma group at the MPE. Thank you for building such a wonderful group at the institute, and also for your support, guidance and the freedom you gave me in choosing the direction of research.

I would like to thank Dr. Hubertus Thomas for his invaluable support in all questions regarding physics, but also in all the projects I wanted to undertake as part of this thesis. Thank you for always taking the time to give advice and encouragement, to listen to ideas and sometimes only the problems I encountered, and for including me in the PK-3 Plus team and trusting me with the responsibility you have.

I am deeply grateful to Dr. Sergey Zhdanov for all the short and not-so-short discussions about physics. Thank you for all the explanations, inspiration and suggestions, and for letting me argue with you about them. You are a wonderful teacher!

I also owe both Hubertus and Sergey for reading this manuscript and giving many helpful suggestions.

I would like to thank Dr. Milenko Rubin-Zuzic for his experimental aptness—he only had to visit the lab once to find a whole bunch of new effects—and for letting me continue investigating these effects. Thank you also for lots of advice and discussions.

My thanks go to the other theoreticians in our group, especially Dr. Alexej Ivlev for the help with explaining the origins of the bubble instability and Dr. Sergey Khrapak for the simulations of the PK-3 Plus chamber and theoretical predictions concerning the strength of the electric and ion drag forces.

I am obliged to the engineers of our group, especially Tanja Hagl, Christian Deysenroth and Dr. Hermann Rothermel, for the technical support with PK-3 Plus in the ground laboratory, during the preparation and execution of the parabolic flight experiment, and with the experiment on the ISS.

My thanks go also to the rest of the PK-3 Plus team for building and maintaining the PK-3 Plus laboratory and welcoming me into the group. I would like to thank especially Dr. Vladimir Molotkov, Dr. Andrej Lipaev and Prof. Fortov of the JIHT for the invaluable work of the part of the team in Russia. And of course I'm extremely grateful for the perfect work of the cosmonauts and astronauts who conduct our experiments on the space station, the very professional ground support at the Mission Control Center Цуп in Korolyov and by RKK Energia, and to all the people who designed and tested the hardware, brought it into space, and continue to support the operation on board the ISS.

I would like to thank the Bundesministerium für Wirtschaft und Technologie (BMWi)

and the Deutsches Zentrum für Luft- und Raumfahrt (DLR) for financially supporting PK-3 Plus (DLR/BMWi Grant No. 50WP0203).

I am very grateful to Peter Huber and Dr. Michael Kretschmer, my office mates, for all the laughter, help, and for listening when needed. Many thanks go to Dr. Uwe Konopka and Robert Sütterlin for sharing lots of code and also for programming advice and, in Uwes case, help with experimental techniques and hardware.

I would like to also thank the rest of complex plasma group for producing such a great atmosphere and for always helping one another: Sebastian Albrecht, Dr. Tetyana Antonova, Dr. Pintu Bandyopadhyay, Philip Brandt, Dr. Manis Chaudhuri, Dr. Lénaïc Couëdel, Chengran Du, Martin Fink, Ralf Heidemann, Florian Huber, Dr. Herwig Höfner, Ke Jiang, Dr. Boris Klumov, Christina Knapek, Dr. Roman Kompaneets, Dr. Yangfang Li, Dr. Vladimir Nosenko, Slobodan Mitic, Dr. Mikhael Pustylnik, Christian Rau, Dr. Satoshi Shimizu, Dr. Tetsuji Shimizu, Günter Stadler, Bernd Steffes, Karl Tarantik, Prof. Dr. Markus Thoma, Prof. Dr. Vadim Tsytovich, Günter Wildgruber, Lisa Woerner, Valeriy Yaroshenko, Dr. Victoria Yarushenko, and Dr. Julia Zimmermann. Special thanks go to our secretaries, Elsbeth Collmar and Angelika Langer, for their support whenever needed.

My deepest gratitude goes to my family for their love and support throughout my life. Without you, I would not be at this point of life now.

And, finally, I would like to thank you, Benny, for being there for me, listening, offering advice, supporting me in all my endeavors, not only, but also in writing this thesis—and for still making me laugh.

Index